

**UCSF**

**UC San Francisco Electronic Theses and Dissertations**

**Title**

Sharp-Wave Ripple Alterations Mark Memory Decline and Interneuron Drive

**Permalink**

<https://escholarship.org/uc/item/2bc340d2>

**Author**

Jones, Emily Aster

**Publication Date**

2019

Peer reviewed|Thesis/dissertation

# Sharp-Wave Ripple Alterations Mark Memory Decline and Interneuron Drive

by  
Emily Jones

## DISSERTATION

Submitted in partial satisfaction of the requirements for degree of  
DOCTOR OF PHILOSOPHY

in

Biomedical Sciences

in the

GRADUATE DIVISION

of the

UNIVERSITY OF CALIFORNIA, SAN FRANCISCO

Approved:

DocuSigned by:

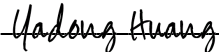


Li Gan

4B293EC353444D2...

Chair

DocuSigned by:



Yadong Huang

DocuSigned by:



Loren Frank

DocuSigned by:



Jeanne Paz

129DDCD87B64445...

Committee Members

Copyright 2019  
by  
Emily A. Jones

## ACKNOWLEDGEMENTS

This thesis was the result of effort and support from many co-workers, friends, and family. First, I thank Yadong Huang and Loren Frank, my two mentors. Yadong first convinced me to switch from molecular neuroscience back to electrophysiology in December of 2014, a decision which completely defined my future career. Yadong has provided many hours-long meetings full of lively discussion and taught me lessons about how to be a PI along the way. Loren taught me through his NS248 class that I had so much to learn, but that he could teach me. He took time out of his full schedule to take me on as an extra mentee and help me fill in the gaps until I finally felt like I knew what I was doing. Second, I thank the entire Huang and Frank labs. In the Huang lab, Victoria Yoon has been a collaborator, lifeline, mouse guru, queen of perfusions, and safety net. Ramsey Najm has been a review co-author, F31 grant writing partner, surgery tag team partner, and friend. Anna Gillespie has been a mentor through Huang and Frank labs, acting practically as my third advisor. None of this thesis would have happened had she not brought electrophysiology to the Huang lab. Third, I thank my thesis committee members, Li Gan – who has strengthened many an experimental design – and Jeanne Paz – who never fails to visit my desk to cheer me on. Fourth, I thank my mentors from before graduate school, in particular Matt Roesch. Spending 3 years in the Roesch lab was what made me realize I might want to be an electrophysiologist. Fifth, I thank my family, including my sister Irene Jones, my parents Margaret and Rick Jones, and my in-laws Catherine, Bruce, Charlotte, and Emily Fallick. They've worked hard to understand what my research is and cheer me on at every little achievement. Finally, I thank my partner and husband, Ozzie Fallick. Ozzie listened untiringly to me explaining how my science is good or bad on any given day, supported me through long work hours, and celebrated every small victory.

## CONTRIBUTIONS

Chapter I contains text adapted from Najm, Jones, & Huang, published on June 11, 2019 in *Molecular Neurodegeneration* (10.1186/s13024-019-0324-6). This review article was written by Ramsey Najm and myself, with editing and supervision from Yadong Huang.

Chapter II contains text and figures reprinted from Jones et al., currently in press at *Cell Reports*. Anna Gillespie, Yadong Huang, and I designed and coordinated the study. I carried out most studies and data analysis and wrote the manuscript. Anna Gillespie contributed to the studies and analysis of the screen cohort. Victoria Yoon managed mouse lines, performed perfusions, and conducted the MWM tests. Desiree Macchia and T. Michael Gill provided assistance with the place avoidance task. Hanci Lei and Alyssa Yang provided assistance with histology. Anna Gillespie, Loren Frank, and Yadong Huang provided advice on data analysis and interpretations and edited the manuscript. Loren Frank and Yadong Huang supervised the project.

Chapter III contains text and figures that are currently under preparation for submission. Yadong Huang, Loren Frank, and I designed and coordinated the study. I carried out most studies, performed all data analysis, and wrote the manuscript. Anna Gillespie and Antara Rao assisted with in vivo electrophysiological recordings. Misha Zilberter and Biljana Djukic performed ex vivo electrophysiology experiments. Antara Rao, Nicole Koutsodendris, Maxine Nelson, and Heidi Yuan assisted with immunohistochemistry. Victoria Yoon managed mouse lines and performed perfusions. Kylie Huang and Michael Gill performed the active place avoidance task and provided advice on data analysis. Yadong Huang and Loren Frank provided advice on data analysis and interpretations, edited the manuscript, and supervised the project.

# Sharp-Wave Ripple Alterations Mark Memory Decline and Interneuron Drive

Emily Aster Jones

## Abstract

Hippocampal sharp-wave ripples (SWRs) – electrophysiological signatures of memory reactivation in the hippocampus – play an important role in memory processes. We tested the relationship between SWRs and memory impairment in an Alzheimer’s disease (AD) mouse model and the role of GABAergic interneurons in modulating SWRs. First, there is a pressing need to identify early pathophysiological alterations that predict subsequent memory impairment in AD. Mouse models of AD show reductions in both SWR abundance and associated slow gamma (SG) power during aging, suggesting SWRs may be a compelling candidate biomarker. In aged AD model mice, we found that reduced SWR abundance and associated CA3 SG power predicted spatial memory impairments measured 1–2 months later. Importantly, SWR-associated CA3 SG power reduction in young apoE4-KI mice also predicted spatial memory deficits measured 10 months later. Second, SWRs in CA1 are driven by inputs from upstream area CA3 and also engage the dentate gyrus (DG), but little is known about whether and how GABAergic interneurons in either CA3 or the DG regulate activity in CA1. The majority of hippocampal interneurons are parvalbumin-expressing (PV+), soma-targeting or somatostatin-expressing (SST+), distal dendrite-targeting subtypes, which are differentially impaired in AD. We find that that PV+ and SST+ interneurons bidirectionally modulate sleep SWRs in CA1 and coincident SG observed throughout the hippocampus. Overall, our results suggest that PV+ interneurons reduce CA3 coupling to CA1, while SST+ interneurons reduce entorhinal cortex coupling to CA1. These results establish features of SWRs as potential functional biomarkers of memory impairment in AD and probe how GABAergic interneuron subtypes impaired in AD modulate these SWR features.

*This thesis is dedicated to my godmother, Joan Jurich*

## TABLE OF CONTENTS

<b>Introduction</b> .....	1
<b>Chapter I: Apolipoprotein E4, Inhibitory Dysfunction, and Alzheimer’s Disease</b>	
Abstract.....	29
Main Text.....	30
References.....	40
<b>Chapter II: Early Hippocampal Sharp-Wave Ripple Deficits Predict Later Learning and Memory Impairments in an Alzheimer’s Disease Mouse Model</b>	
Abstract.....	59
Introduction.....	60
Materials and Methods.....	63
Results.....	72
Discussion.....	109
References.....	115
<b>Chapter III: Hippocampal GABAergic Interneurons Bidirectionally Modulate Sharp-Wave Ripples</b>	
Abstract.....	124
Introduction.....	125
Materials and Methods.....	127
Results.....	134
Discussion.....	155
References.....	161
<b>Conclusion</b> .....	178



## LIST OF FIGURES

### Chapter II

<i>Figure 2.1:</i> Aged apoE4-KI mice show SWR deficits and spatial approach task impairments and variability .....	74
<i>Figure 2.2:</i> SWR deficits predicts spatial approach task impairments in aged apoE4-KI mice ...	82
<i>Figure 2.3:</i> Further predictive relationships identified in the screen cohort and examples of behavioral metrics used in correlations.....	84
<i>Figure 2.4:</i> ApoE4-KI mice are not impaired in non-spatial behaviors.....	86
<i>Figure 2.5:</i> SWR deficits predict spatial avoidance task impairments in aged apoE4-KI mice ...	95
<i>Figure 2.6:</i> Aged apoE4-KI mice show impaired acquisition of a spatial avoidance task .....	97
<i>Figure 2.7:</i> SWR deficits at younger ages predict spatial approach and spatial avoidance task impairments at older ages .....	104
<i>Figure 2.8:</i> Properties of SWRs and associated SG power in CA3 over aging in apoE3-KI and apoE4-KI mice .....	106
<i>Figure 2.9:</i> SWRs and associated SG power in SG as a proposed biomarker .....	110

### Chapter III

<b>Figure 3.1:</b> Recording <i>in vivo</i> hippocampal LFP during chemogenetic suppression of PV <sup>+</sup> and SST <sup>+</sup> interneurons in CA3 and DG .....	135
<b>Figure 3.2:</b> DREADDs function and expression in PV <sup>+</sup> and SST <sup>+</sup> interneurons in CA3 and DG .....	136
<b>Figure 3.3:</b> Suppressing PV <sup>+</sup> interneurons increases CA3 coupling onto CA1 during SWRs ...	139
<b>Figure 3.4:</b> Properties of SWRs during PV <sup>+</sup> interneuron suppression .....	141
<b>Figure 3.5:</b> Suppressing SST <sup>+</sup> interneurons decreases CA3 coupling onto CA1 during SWRs .	145
<b>Figure 3.6:</b> Properties of SWRs during SST <sup>+</sup> interneuron suppression .....	147
<b>Figure 3.7:</b> Figure S4. Suppressing both PV <sup>+</sup> and SST <sup>+</sup> interneurons increases CA3 coupling onto CA1 during SWRs .....	149

## LIST OF TABLES

### Chapter II

<i>Table 2.1:</i> Sample sizes for all experiments .....	75
<i>Table 2.2:</i> Relationships between SWR properties and MWM performance tested in screen cohort .....	87
<i>Table 2.3:</i> All APA metric correlations tested in replication cohort .....	99
<i>Table 2.4:</i> All behavioral correlations tested with 5–8 month apoE4-KI mouse electrophysiological data .....	108

### Chapter III

<i>Table 3.1:</i> Sex differences across all mice in vehicle-treated epochs.....	151
<i>Table 3.2:</i> Effects of PV+ and/or SST+ suppression stratified by sex .....	153

## INTRODUCTION

### **Alzheimer's Disease (AD) and Apolipoprotein (apo) E4**

AD is the most common form of dementia, affecting 5 million Americans, including 11% of all people over 65 and 32% of all people over 85<sup>1</sup>. AD patients exhibit impaired communication, disorientation, changes in mood and personality, and problems retrieving and forming memories. AD is characterized by damage to and death of neurons, particularly in the hippocampus and cerebral neocortex, as well as neuropathological hallmarks, including extracellular amyloid  $\beta$  plaques and intracellular tau neurofibrillary tangles<sup>2</sup>. How this molecular pathology, neuronal loss, and memory deficit are connected, however, still needs further investigation. One protein key to understanding these relationships is apoE, the most common genetic risk factor for AD.

In humans, there are three major apoE alleles – apoE2, apoE3, and apoE4 – which differ at two positions in their primary sequence<sup>3,4</sup>. ApoE4 has an allelic frequency of 14%, yet is found in 65-80% of AD patients<sup>5</sup>. In a dose-dependent manner, the presence of the apoE4 allele increases the likelihood of AD diagnosis at age 85 from 10% to 70% and decreases the average age of disease onset from 84 years to 68 years<sup>6</sup>. In the nervous system, apoE4 is more likely to be carboxyl-terminal truncated in neurons than apoE3, which increases tau phosphorylation<sup>7</sup>, induces neurofibrillary tangle-like inclusions<sup>8</sup>, and causes inefficient amyloid  $\beta$  clearance<sup>9</sup>, linking apoE4 to current AD neuropathology hypotheses.

Mice with human apoE4 knocked in at the mouse apoE locus (apoE4-KI) show age-dependent spatial learning and memory deficits which are correlated with age-dependent hilar GABAergic interneuron loss<sup>10,11</sup>. Transplanting GABAergic interneuron progenitors into the hilus rescues apoE4-induced learning and memory deficits<sup>12</sup>, while optogenetically inhibiting hilar GABAergic interneurons induces these deficits<sup>13</sup>, confirming that hilar interneuron loss causes

these learning and memory deficits. Interestingly, despite the fact that most nervous system apoE is produced by astrocytes<sup>8</sup>, knocking out apoE4 expression in interneurons prevents GABAergic interneuron death and apoE4-induced learning and memory deficits, while knocking out apoE4 expression in astroglia does not<sup>14</sup>. Thus, the pathological role of apoE depends on its cellular source within the hippocampus.

### **Rhythms of the Hippocampus**

The hippocampus is required for spatial learning, working memory, and reference memory, which are disrupted in AD<sup>15-17</sup>. The densely packed organization of this structure lends itself to generating large local field potentials, which are the extracellular currents that reflect the summation of action potentials from these neurons. This raw local field potential signal can be decomposed into frequency components, some of which are associated with specific functions<sup>18</sup>. These rhythms organize firing of cells that code related information<sup>19</sup>. Moreover, these rhythms provide a mechanism for task-specific neural networks to transiently connect through synchronized firing, allowing one area to coordinate processes across the entire brain<sup>20</sup>. Oscillations furthermore coordinate cell assemblies to bring together enough collective spiking to discharge the postsynaptic target<sup>19</sup>. Several reviews have proposed that hippocampal network oscillations would make ideal candidates for testing the physiological effect of AD drug candidates<sup>21,22</sup>. These oscillations are clear memory biomarkers, as they represent encoding, consolidation, and retrieval of task-related sequences and the integration of these sequences into cortical circuits to modify behavior and memory performance<sup>21</sup>. The hippocampus generates three major rhythms: theta, gamma, and SWRs.

Theta (4-12Hz) is the network signature of memory encoding during locomotion in humans<sup>23</sup> and rodents<sup>24,25</sup>. The main driver of hippocampal theta is tonic cholinergic excitation and phasic GABAergic inhibition of local interneurons by medial septum (MS) inputs<sup>26-28</sup>. The hippocampus has two theta dipoles. The first has a current sink in stratum radiatum and a current source in stratum pyramidale, reflecting Schaffer collateral inputs<sup>29</sup>. The second has a current sink in stratum lacunosum-moleculare and a source in stratum radiatum, reflecting direct entorhinal cortex (EC) glutamatergic inputs<sup>29</sup>, possibly onto CA1 pyramidal cell dendrites<sup>28</sup>. During locomotion, theta entrains place cell activity. As an animal explores a space, place cells in the CA1 and CA3 preferentially fire in certain locations, and each theta cycle contains one path in the space<sup>30</sup>. Place cells fire at successively later theta phases as they move through their place field, a phenomenon known as theta phase precession<sup>31,32</sup>. Thus, theta allows place cells to encode location via spike rate and timing. At decision points in learned working memory tasks, place cells for fields ahead of the animal preferentially fire and predict which choice an animal will make<sup>33</sup>. Moreover, the length of the prospective portion of a theta sequence predicts how far an animal will travel to its goal destination. Thus, theta is directly relevant to current spatial decisions<sup>34</sup>. Furthermore, disrupting theta sequences and theta phase precession impairs working memory<sup>35,36</sup>. Finally, theta power during tasks predicts memory performance in animals<sup>37-39</sup> and humans<sup>40</sup>, and disrupting theta oscillations impairs working memory<sup>41</sup> and reference memory<sup>42</sup>. While the SWR and associated slow gamma phenotype has been characterized in apoE4-KI mice, theta has not, which could elucidate the extent of network deficits and mechanisms of learning and memory impairments in apoE4 carriers.

During theta, gamma amplitude<sup>25</sup>, frequency<sup>43</sup>, and phase<sup>44</sup> are coupled to theta phase. The hippocampus has two gamma current generators: one in the DG and another in CA3. Gamma is

hypothesized to be driven by EPSPs from perforant path inputs and IPSPs from local oscillating interneurons. The DG gamma dipole, which drives the largest amplitude gamma activity, is itself driven by EC, as indicated by a current sink in stratum lacunosum-moleculare. Following EC lesion, DG theta and gamma amplitude is greatly reduced. The gamma that remains is lower frequency and driven by the CA3 dipole, as indicated by a current sink in stratum radiatum<sup>45</sup>. Both dipoles are driven by PV<sup>+</sup> basket cells<sup>46-48</sup>. Thus, hippocampal gamma comprises two frequency components: slow gamma (30-50Hz), driven by CA3 intrinsic inputs at the trough of theta in the stratum pyramidale, and fast gamma (50-100Hz), driven by EC extrinsic inputs at the descending phase of theta in the stratum pyramidale<sup>49</sup>. This switch between extrinsic and intrinsic inputs to CA3 in a single theta cycle during exploration of a novel environment is modulated by MS cholinergic inputs<sup>50</sup>. However, one study demonstrated that *in vitro* cholinergic drive of interneuron networks in CA1 alone can generate fast gamma<sup>51</sup>; this may be generated *in vivo* by direct EC inputs to CA1<sup>52</sup>. Gamma power is correlated with recall<sup>53</sup> and working memory load<sup>54</sup> in humans. Similarly, during working memory tasks, CA1 and CA3 gamma power and coherence increases<sup>55</sup>. Task-related theta-gamma coupling is also correlated with memory performance in humans<sup>56,57</sup>. This coupling and gamma power was recently found to be reduced in a mouse model of tauopathy<sup>58</sup>. Despite extensive research on the role of theta and nested gamma in memory and on the deficits in these oscillations in AD models, the relationship between theta deficits and working memory deficits in an AD model has not been determined.

One model of theta and nested gamma states that encoding and retrieval are segregated by theta phase, with encoding occurring on the trough of theta when EC input is highest and retrieval occurring on the peak of theta when output to EC is highest<sup>59</sup>. Several lines of evidence support this. First, CA1 pyramidal cells fire preferentially on different phases of theta during when

encountering new and familiar stimuli<sup>60</sup>. Second, LTP is easiest to induce along Schaffer collaterals at the trough of theta, consistent with the idea that this theta phase is involved in encoding new information from cortical inputs<sup>61</sup>. Third, inhibiting CA1 at the trough of theta during the encoding portion of a task enhanced performance, while inhibiting CA1 at the peak of theta during retrieval also enhanced performance<sup>62</sup>. Finally, gamma power and place cell firing during theta also support this model.

During theta, gamma modulates theta phase procession<sup>63</sup>. Approximately one place cell fires at the trough of each fast gamma wave, while compressed paths are within each slow gamma wave. The firing of place cells also shows phase procession with respect to slow gamma. In this study, path length ahead of the animal increased with slow gamma power and accuracy of current location encoding increased with fast gamma power, lending further credence to the hypothesis that slow gamma is involved in retrieval while fast gamma is responsible for encoding during theta<sup>64</sup>. Place cell firing also preferentially encodes locations ahead of an animal when slow gamma power is higher or the animal leaves a goal location and behind an animal when fast gamma power is higher or the animal approaches a goal location<sup>65,66</sup>. Moreover, fast gamma power and theta coupling increases when attending to novel stimuli<sup>67</sup> while slow gamma power and theta coupling increases during when attending to recalled stimuli<sup>68,69</sup>. However, one study found an increase in slow gamma coherence during encoding<sup>70</sup>, while another found an increase in fast gamma coherence during retrieval<sup>71</sup>, suggesting that this hypothesis may not be complete.

The third hippocampal rhythm, SWRs, are the network signature of memory replay<sup>21</sup>. When the animal is at rest or asleep, place cells fire in a compressed manner at the troughs of SWRs<sup>72</sup>, replaying forward or reverse trajectories traversed by the animal<sup>73,74</sup>. Sharp waves are generated by CA3 pyramidal population bursts exciting CA1 pyramidal dendrites and GABAergic



interneurons, which in turn inhibit CA1 pyramidal near the soma<sup>75</sup>; this sharp wave input is reflected in the current sink in stratum radiatum<sup>76</sup>. The interconnected CA1 pyramidal cell and interneuron network give rise to high frequency (150-250Hz) synchronized ripple activity in the stratum pyramidale<sup>76</sup>. Two studies have found that this CA1 network can generate SWRs independent of CA3, though their relevance to memory retrieval and consolidation is unknown<sup>77,78</sup>. SWRs occur in the absence of theta activity and are suppressed by MS activation<sup>79</sup>. Similarly, SWRs rarely occur during high gamma power in the DG<sup>80</sup>. Unlike theta and gamma oscillations, SWR LFPs are hypothesized to be mostly generated by summation of currents on pyramidal cells<sup>81</sup>. SWR power is correlated with the discharge probability of CA1 pyramidal cells, but not of interneurons<sup>77</sup>. Nevertheless, perisomatic inhibition is still critical for phase locking of pyramidal cell firing to SWRs<sup>21</sup>.

SWRs are critical for memory consolidation and retrieval<sup>82</sup>, as their disruption by stimulating the ventral hippocampal commissure impairs spatial learning and memory<sup>83-85</sup>. Awake SWRs are crucial for retrieval. These SWRs encode realistic paths within the current environment and are biased towards the current location<sup>74,86</sup>. Awake SWRs often occur at decision points during early learning of working memory tasks<sup>87</sup>, and trajectories of place cells active during these SWRs represent paths to goals, with bias towards the goal location and the angular displacement to a known goal<sup>88</sup>. Similar to theta sequences, SWRs preferentially replay forward when moving towards a goal and reverse when reaching the goal<sup>74</sup>. Reduced SWR abundance<sup>89-91</sup> and aberrant spatial encoding by place cells<sup>92,93</sup> have recently been found in mouse models of tau and amyloid  $\beta$  overexpression, suggesting that SWRs could be a relevant cognitive biomarker for AD. In addition, SWRs have been found to promote memory consolidation in humans<sup>94</sup>. Despite extensive research demonstrating that SWRs are critical in memory performance and that SWRs are less

abundant in AD models, the relationship between SWRs and memory in AD models has yet to be explored.

During SWRs, slow gamma power increases, and the fidelity of place cell replay is correlated with the extent of slow gamma synchrony<sup>95</sup>. In addition, path representations jump from one location at the troughs of discrete SWR-associated slow gamma cycles. Place cell firing is similarly locked to the opposite phase of slow gamma. Thus, slow gamma might coordinate compressed replay of a trajectory<sup>96</sup>. Cingulate cortex neurons also phase lock with hippocampal slow gamma during SWRs, suggesting that increased slow gamma power might be necessary to plan future trajectories<sup>97</sup>. Despite these studies, the mechanism of SWR-associated slow gamma has not been uncovered.

### **Hippocampal Inhibitory Interneurons**

Dysfunction of the GABAergic inhibitory system contributes to learning and memory impairment in mice and possibly in humans. AD patients have reduced GABAergic inhibitory function, as suggested by an increase in subclinical epileptiform activity<sup>98</sup>. Furthermore, AD patients have specific losses of SST<sup>+</sup> interneurons in the cortex<sup>99</sup> and hippocampus<sup>100</sup>, which are exacerbated by the presence of the apoE4 allele<sup>101</sup>. This inhibition regulates learning, as feed-forward inhibitory connectivity growth is required for memory precision<sup>102</sup> and reducing hippocampal GABA levels impairs learning and memory<sup>103</sup>. Finally, GABAergic interneuron loss reduces GABA signaling on newborn neurons from the subgranular zone, impairing hippocampal neurogenesis<sup>7</sup>, which is exacerbated by apoE4<sup>11</sup>, further contributing to learning and memory deficits. Interestingly, despite clear evidence linking AD to SST<sup>+</sup> interneuron loss, it is unclear whether interneuron loss or dysfunction is responsible for memory deficits.

Rhythmic firing emerges spontaneously from interconnected pyramidal and interneuron networks due to intrinsic membrane properties of interneurons<sup>104</sup>. Most oscillations of the hippocampus are driven by perisomatic feedback IPSPs onto principal cells by local interneurons<sup>105</sup>. Hippocampal interneurons show place preference in firing<sup>106,107</sup>, are responsible for theta phase procession<sup>108</sup>. Thus, hippocampal GABAergic interneurons contribute to local network activity.

GABAergic interneurons can be classified by the presence of molecular markers that differentiate unique morphologies and connections<sup>109</sup>. The neuropeptide SST labels oriens-lacunosum moleculare (O-LM) cells, which comprise 52% of all GABAergic interneurons in the stratum oriens, and hilar perforant path-associated (HIPP) cells, which comprise 57% of all interneurons in the hilus<sup>110</sup>. Both subtypes receive local excitatory input along the perforant path and provide slow feedback inhibition onto principal cell dendrites at the layer of extrahippocampal excitatory inputs from EC and MS<sup>109</sup>. These SST<sup>+</sup> interneurons also project onto PV<sup>+</sup> interneurons in the MS<sup>111,112</sup> and the EC<sup>113</sup>, which in turn project back onto interneurons throughout the hippocampus<sup>27,114</sup>. In addition, though most cholinergic projections from MS are onto principal cells, 5-10% are onto SST<sup>+</sup> cells<sup>115</sup>. These recurrent connections may act as a regulator of theta<sup>116</sup>. Furthermore, O-LM spiking is entrained to the trough of theta<sup>117,118</sup>. O-LM cells were also able to generate coherent gamma oscillations in one computational model<sup>119</sup> and had spiking entrained to the ascending phase of gamma in awake mice<sup>118</sup>. O-LM cells may also modulate the switch from fast gamma entorhinal inputs and slow gamma CA3 inputs<sup>120</sup>. Finally, spiking of O-LM cells, including those that project to MS, increases during the ascending phase of SWRs<sup>118,121,122</sup>.

HIPP interneurons are critical in age-related and AD-related cognitive decline. SST<sup>+</sup> HIPP interneurons are highly vulnerable to excitotoxicity<sup>123</sup>, which apoE3, but not apoE4, protects

against<sup>124</sup>. SST<sup>+</sup> HIPP interneurons are selectively lost through normal aging<sup>125</sup>, and the extent of loss of these neurons is correlated with reference memory in both aged WT<sup>125</sup> and apoE4-KI<sup>10</sup> mice. HIPP interneurons have very similar connections and membrane properties as O-LM cells, so they may participate in hippocampal rhythms like O-LM cells. However, the contribution of HIPP interneurons to this network activity has not been studied.

The calcium-binding protein PV labels basket and axoaxonic cells, comprising 32% of GABAergic interneurons in the strata oriens and pyramidale and 8% of all interneurons in the hilus<sup>126</sup>. Both subtypes receive both local and extrahippocampal excitatory inputs and thus provide fast feed-forward and feedback perisomatic inhibition at the principal cell layer<sup>109</sup>. Basket cells fire preferentially at the descending phase of theta, while axoaxonic cells increase firing at the peak of theta; this firing is simultaneously coupled to the rising phase of gamma<sup>117,118,127</sup>. Several lines of evidence support the critical role of basket cells in generating gamma. First, CA1 basket cells impose rhythmic IPSPs onto pyramidal cells at gamma frequency during theta activity, timing their firing<sup>128</sup>. Second, unlike O-LM cells, basket cells are mutually connected into an extensive network, which is hypothesized to be necessary to generate gamma<sup>129</sup>. Third, MS cholinergic inputs likely drive theta and nested gamma coupled firing in PV<sup>+</sup> basket cells, as applying muscarinic agonists *in vitro* causes gamma frequency firing in these cells<sup>130</sup>. However, ablating GABA<sub>A</sub>-mediated synaptic transmission in PV<sup>+</sup> interneurons was found to reduce theta power, frequency, and modulation of gamma phase, amplitude and spike timing, but not gamma power, calling into question the sufficiency of PV<sup>+</sup> interneurons in generating gamma<sup>131</sup>.

Basket cells also fire preferentially at the trough of SWRs, while axoaxonic cells fire immediately before SWR events<sup>117,118</sup>, which is hypothesized to contribute to sharp wave burst generation<sup>132</sup>. Suppressing GABA<sub>A</sub>-mediated perisomatic inhibition onto pyramidal cells reduces

SWR energy and SWR entrainment of pyramidal cell firing<sup>133,134</sup>, while activating CA3 basket cells *in vitro* increases SWR abundance<sup>135</sup>. Moreover, tonic drive of PV<sup>+</sup> CA1 interneurons alone can generate SWRs, while silencing these same cells can interrupt SWRs, suggesting PV<sup>+</sup> interneurons are necessary SWR generation<sup>136</sup>. However, most studies of PV<sup>+</sup> interneurons are in CA1, thus little is known about the role of hilar basket cells on hippocampal network activity.

SST<sup>+</sup> and PV<sup>+</sup> interneurons likely coordinate to generate these rhythms. First, it is hypothesized that PV<sup>+</sup> basket cells and SST<sup>+</sup> HIPPs are recruited in concert during theta-nested gamma so that HIPPs can provide delayed dendritic inhibition<sup>137</sup>. Second, basket cells drive intrinsic membrane theta outside of a cell's place field, while apical dendrite polarization drives membrane theta inside a cell's place field<sup>29</sup>. This cooperation between perisomatic and dendrite targeting cells drives theta-coordinated place cell firing<sup>138</sup>. Third, PV<sup>+</sup> interneurons preferentially fire at an earlier theta phase<sup>118</sup>, and silencing these neurons increased firing at the start of a cell's place field<sup>139</sup>, suggesting PV<sup>+</sup> interneurons might be responsible for determining which place cells become active. In contrast, SST<sup>+</sup> interneurons preferentially fire at a later phase<sup>118</sup>, and silencing these neurons increased firing at the end of a cell's place field<sup>139</sup>, suggesting SST<sup>+</sup> interneurons might be responsible updating the network representation of space.

## References

1. Hebert, L. E., Weuve, J., Scherr, P. A. & Evans, D. A. Alzheimer disease in the United States (2010-2050) estimated using the 2010 census. *Neurology* **80**, 1778–1783 (2013).
2. Mattson, M. P. Pathways towards and away from Alzheimer's disease. *Nature* **430**, 631–639 (2004).
3. Mahley, R. W. Apolipoprotein E: cholesterol transport protein with expanding role in cell biology. *Science* **240**, 622–630 (1988).
4. Weisgraber, K. H. Apolipoprotein E: structure-function relationships. *Adv Protein Chem* **45**, 249–302 (1994).
5. Farrer, L. A., Cupples, L. A., Haines, J. L., Hyman, B. T., Kukull, W. A., Mayeux, R., Myers, R. H., Pericak-Vance, M. A., Risch, N. & van Duijn, C. M. Effects of age, sex, and ethnicity on the association between apolipoprotein E genotype and Alzheimer disease. A meta-analysis. APOE and Alzheimer Disease Meta Analysis Consortium. *JAMA* **278**, 1349–1356 (1997).
6. Corder, E. H., Saunders, A. M., Strittmatter, W. J., Schmechel, D. E., Gaskell, P. C., Small, G. W., Roses, A. D., Haines, J. L. & Pericak-Vance, M. A. Gene dose of apolipoprotein E type 4 allele and the risk of Alzheimer's disease in late onset families. *Science* **261**, 921–923 (1993).
7. Li, G., Bien-Ly, N., Andrews-Zwilling, Y., Xu, Q., Bernardo, A., Ring, K., Halabisky, B., Deng, C., Mahley, R. W. & Huang, Y. GABAergic interneuron dysfunction impairs hippocampal neurogenesis in adult apolipoprotein E4 knockin mice. *Cell Stem Cell* **5**, 634–645 (2009).
8. Huang, Y., Liu, X. Q., Wyss-Coray, T., Brecht, W. J., Sanan, D. A. & Mahley, R. W.

- Apolipoprotein E fragments present in Alzheimer's disease brains induce neurofibrillary tangle-like intracellular inclusions in neurons. *Proc Natl Acad Sci U S A* **98**, 8838–8843 (2001).
9. Bien-Ly, N., Andrews-Zwilling, Y., Xu, Q., Bernardo, A., Wang, C. & Huang, Y. C-terminal-truncated apolipoprotein (apo) E4 inefficiently clears amyloid-beta (A $\beta$ ) and acts in concert with A $\beta$  to elicit neuronal and behavioral deficits in mice. *Proc Natl Acad Sci U S A* **108**, 4236–4241 (2011).
  10. Andrews-Zwilling, Y., Bien-Ly, N., Xu, Q., Li, G., Bernardo, A., Yoon, S. Y., Zwilling, D., Yan, T. X., Chen, L. & Huang, Y. Apolipoprotein E4 causes age- and Tau-dependent impairment of GABAergic interneurons, leading to learning and memory deficits in mice. *J Neurosci* **30**, 13707–13717 (2010).
  11. Leung, L., Andrews-Zwilling, Y., Yoon, S. Y., Jain, S., Ring, K., Dai, J., Wang, M. M., Tong, L., Walker, D. & Huang, Y. Apolipoprotein E4 causes age- and sex-dependent impairments of hilar GABAergic interneurons and learning and memory deficits in mice. *PLoS One* **7**, e53569 (2012).
  12. Tong, L. M., Djukic, B., Arnold, C., Gillespie, A. K., Yoon, S. Y., Wang, M. M., Zhang, O., Knoferle, J., Rubenstein, J. L. R., Alvarez-Buylla, A. & Huang, Y. Inhibitory interneuron progenitor transplantation restores normal learning and memory in ApoE4 knock-in mice without or with A $\beta$  accumulation. *J. Neurosci.* **34**, 9506–15 (2014).
  13. Andrews-Zwilling, Y., Gillespie, A. K., Kravitz, A. V., Nelson, A. B., Devidze, N., Lo, I., Yoon, S. Y., Bien-Ly, N., Ring, K., Zwilling, D., Potter, G. B., Rubenstein, J. L. R., Kreitzer, A. C. & Huang, Y. Hilar GABAergic interneuron activity controls spatial learning and memory retrieval. *PLoS One* **7**, e40555 (2012).

14. Knoferle, J., Yoon, S. Y., Walker, D., Leung, L., Gillespie, A. K., Tong, L. M., Bien-Ly, N. & Huang, Y. Apolipoprotein E4 produced in GABAergic interneurons causes learning and memory deficits in mice. *J. Neurosci.* **34**, 14069–14078 (2014).
15. Squire, L. R. & Zola-Morgan, J. T. The cognitive neuroscience of human memory since H.M. *Annu Rev Neurosci* **34**, 259–288 (2011).
16. Morris, R. G. & Baddeley, A. D. Primary and working memory functioning in Alzheimer-type dementia. *J. Clin. Exp. Neuropsychol.* **10**, 279–96 (1988).
17. deIpoliti, A. R., Rankin, K. P., Mucke, L., Miller, B. L. & Gorno-Tempini, M. L. Spatial cognition and the human navigation network in AD and MCI. *Neurology* **69**, 986–97 (2007).
18. Buzsáki, G., Anastassiou, C. A. & Koch, C. The origin of extracellular fields and currents — EEG, ECoG, LFP and spikes. *Nat. Rev. Neurosci.* **13**, 407–420 (2012).
19. Harris, K. D., Csicsvari, J., Hirase, H., Dragoi, G. & Buzsáki, G. Organization of cell assemblies in the hippocampus. *Nature* **424**, 552–6 (2003).
20. Nyhus, E. & Curran, T. Functional role of gamma and theta oscillations in episodic memory. *Neurosci. Biobehav. Rev.* **34**, 1023–35 (2010).
21. Buzsáki, G. Hippocampal sharp wave-ripple: A cognitive biomarker for episodic memory and planning. *Hippocampus* **1188**, 1073–1188 (2015).
22. Palop, J. J., Chin, J. & Mucke, L. A network dysfunction perspective on neurodegenerative diseases. *Nature* **443**, 768–773 (2006).
23. Ekstrom, A. D., Caplan, J. B., Ho, E., Shattuck, K., Fried, I. & Kahana, M. J. Human hippocampal theta activity during virtual navigation. *Hippocampus* **15**, 881–9 (2005).
24. Vanderwolf, C. H. Hippocampal electrical activity and voluntary movement in the rat.



- Electroencephalogr. Clin. Neurophysiol.* **26**, 407–18 (1969).
25. Buzsáki, G., Leung, L. & Vanderwolf, C. H. Cellular bases of hippocampal EEG in the behaving rat. *Brain Res.* **287**, 139–71 (1983).
  26. Green, J. D. & Arduini, A. A. Hippocampal Electrical Activity in Arousal. *J Neurophysiol* **17**, 533–557 (1954).
  27. Freund, T. F. & Antal, M. GABA-containing neurons in the septum control inhibitory interneurons in the hippocampus. *Nature* **336**, 170–173 (1988).
  28. Buzsáki, G. Theta Oscillations in the Hippocampus. *Neuron* **33**, 325–340 (2002).
  29. Kamondi, A., Acsády, L., Wang, X.-J. & Buzsáki, G. Theta oscillations in somata and dendrites of hippocampal pyramidal cells in vivo: Activity-dependent phase-precession of action potentials. *Hippocampus* **8**, 244–261 (1998).
  30. Foster, D. J. & Wilson, M. A. Hippocampal theta sequences. *Hippocampus* **17**, 1093–9 (2007).
  31. O’Keefe, J. & Recce, M. L. Phase relationship between hippocampal place units and the EEG theta rhythm. *Hippocampus* **3**, 317–30 (1993).
  32. Skaggs, W. E., McNaughton, B. L., Wilson, M. A. & Barnes, C. A. Theta phase precession in hippocampal neuronal populations and the compression of temporal sequences. *Hippocampus* **6**, 149–72 (1996).
  33. Johnson, A. & Redish, A. D. Neural ensembles in CA3 transiently encode paths forward of the animal at a decision point. *J. Neurosci.* **27**, 12176–89 (2007).
  34. Wikenheiser, A. M. & Redish, A. D. Hippocampal theta sequences reflect current goals. *Nat. Neurosci.* **18**, 289–94 (2015).
  35. Robbe, D., Montgomery, S. M., Thome, A., Rueda-Orozco, P. E., McNaughton, B. L. &

- Buzsáki, G. Cannabinoids reveal importance of spike timing coordination in hippocampal function. *Nat. Neurosci.* **9**, 1526–33 (2006).
36. Robbe, D. & Buzsáki, G. Alteration of theta timescale dynamics of hippocampal place cells by a cannabinoid is associated with memory impairment. *J. Neurosci.* **29**, 12597–605 (2009).
  37. Landfield, P. W., McGaugh, J. L. & Tusa, R. J. Theta Rhythm: A Temporal Correlate of Memory Storage Processes in the Rat. *Science* **175**, 87–89 (1972).
  38. Winson, J. Loss of hippocampal theta rhythm results in spatial memory deficit in the rat. *Science* **201**, 160–163 (1978).
  39. Berry, S. & Thompson, R. Prediction of learning rate from the hippocampal electroencephalogram. *Science* **200**, 1298–1300 (1978).
  40. Lega, B. C., Jacobs, J. & Kahana, M. J. Human hippocampal theta oscillations and the formation of episodic memories. *Hippocampus* **22**, 748–61 (2012).
  41. Wang, Y., Romani, S., Lustig, B., Leonardo, A. & Pastalkova, E. Theta sequences are essential for internally generated hippocampal firing fields. *Nat. Neurosci.* **18**, 282–8 (2015).
  42. Lee, H., Dvorak, D., Kao, H.-Y., Duffy, Á. M., Scharfman, H. E. & Fenton, A. A. Early cognitive experience prevents adult deficits in a neurodevelopmental schizophrenia model. *Neuron* **75**, 714–24 (2012).
  43. Schomburg, E. W., Fernández-Ruiz, A., Mizuseki, K., Berényi, A., Anastassiou, C. A., Koch, C. & Buzsáki, G. Theta Phase Segregation of Input-Specific Gamma Patterns in Entorhinal-Hippocampal Networks. *Neuron* **84**, 470–485 (2014).
  44. Belluscio, M. A., Mizuseki, K., Schmidt, R., Kempter, R. & Buzsáki, G. Cross-frequency

- phase-phase coupling between  $\theta$  and  $\gamma$  oscillations in the hippocampus. *J. Neurosci.* **32**, 423–35 (2012).
45. Bragin, A., Jandó, G., Nádasdy, Z., Hetke, J., Wise, K., Buzsáki, G., Szabó, G., Freund, T. F. & Hájos, N. Gamma (40-100 Hz) oscillation in the hippocampus of the behaving rat. *J. Neurosci.* **15**, 47–60 (1995).
  46. Hájos, N., Pálhalmi, J., Mann, E. O., Németh, B., Paulsen, O. & Freund, T. F. Spike timing of distinct types of GABAergic interneuron during hippocampal gamma oscillations in vitro. *J. Neurosci.* **24**, 9127–37 (2004).
  47. Mann, E. O., Suckling, J. M., Hajos, N., Greenfield, S. A. & Paulsen, O. Perisomatic feedback inhibition underlies cholinergically induced fast network oscillations in the rat hippocampus in vitro. *Neuron* **45**, 105–17 (2005).
  48. Gulyás, A. I., Szabó, G. G., Ulbert, I., Holderith, N., Monyer, H., Erdélyi, F., Szabó, G., Freund, T. F. & Hájos, N. Parvalbumin-containing fast-spiking basket cells generate the field potential oscillations induced by cholinergic receptor activation in the hippocampus. *J. Neurosci.* **30**, 15134–45 (2010).
  49. Colgin, L. L., Denninger, T., Fyhn, M., Hafting, T., Bonnevie, T., Jensen, O., Moser, M.-B. & Moser, E. I. Frequency of gamma oscillations routes flow of information in the hippocampus. *Nature* **462**, 353–357 (2009).
  50. Villarreal, D. M., Gross, A. L. & Derrick, B. E. Modulation of CA3 afferent inputs by novelty and theta rhythm. *J. Neurosci.* **27**, 13457–67 (2007).
  51. Pietersen, A. N. J., Ward, P. D., Hagger-Vaughan, N., Wiggins, J., Jefferys, J. G. R. & Vreugdenhil, M. Transition between fast and slow gamma modes in rat hippocampus area CA1 in vitro is modulated by slow CA3 gamma oscillations. *J. Physiol.* **592**, 605–20

- (2014).
52. Lasztóczy, B. & Klausberger, T. Layer-specific GABAergic control of distinct gamma oscillations in the CA1 hippocampus. *Neuron* **81**, 1126–39 (2014).
  53. Sederberg, P. B., Schulze-Bonhage, A., Madsen, J. R., Bromfield, E. B., McCarthy, D. C., Brandt, A., Tully, M. S. & Kahana, M. J. Hippocampal and neocortical gamma oscillations predict memory formation in humans. *Cereb. Cortex* **17**, 1190–6 (2007).
  54. van Vugt, M. K., Schulze-Bonhage, A., Litt, B., Brandt, A. & Kahana, M. J. Hippocampal gamma oscillations increase with memory load. *J. Neurosci.* **30**, 2694–9 (2010).
  55. Montgomery, S. M. & Buzsáki, G. Gamma oscillations dynamically couple hippocampal CA3 and CA1 regions during memory task performance. *Proc. Natl. Acad. Sci. U. S. A.* **104**, 14495–500 (2007).
  56. Chaieb, L., Leszczynski, M., Axmacher, N., Höhne, M., Elger, C. E. & Fell, J. Theta-gamma phase-phase coupling during working memory maintenance in the human hippocampus. *Cogn. Neurosci.* **6**, 149–157 (2015).
  57. Lega, B. C., Burke, J., Jacobs, J. & Kahana, M. J. Slow-Theta-to-Gamma Phase-Amplitude Coupling in Human Hippocampus Supports the Formation of New Episodic Memories. *Cereb. Cortex* **26**, 268–78 (2016).
  58. Booth, C. A., Ridler, T., Murray, T. K., Ward, M. A., de Groot, E., Goodfellow, M., Phillips, K. G., Randall, A. D. & Brown, J. T. Electrical and Network Neuronal Properties Are Preferentially Disrupted in Dorsal, But Not Ventral, Medial Entorhinal Cortex in a Mouse Model of Tauopathy. *J. Neurosci.* **36**, 312–24 (2016).
  59. Hasselmo, M. E. What is the function of hippocampal theta rhythm?--Linking behavioral

- data to phasic properties of field potential and unit recording data. *Hippocampus* **15**, 936–49 (2005).
60. Manns, J. R., Zilli, E. A., Ong, K. C., Hasselmo, M. E. & Eichenbaum, H. Hippocampal CA1 spiking during encoding and retrieval: Relation to theta phase. *Neurobiol. Learn. Mem.* **87**, 9–20 (2007).
  61. Hasselmo, M. E., Bodelón, C. & Wyble, B. P. A proposed function for hippocampal theta rhythm: separate phases of encoding and retrieval enhance reversal of prior learning. *Neural Comput.* **14**, 793–817 (2002).
  62. Siegle, J. H. & Wilson, M. A. Enhancement of encoding and retrieval functions through theta phase-specific manipulation of hippocampus. *Elife* **3**, e03061 (2014).
  63. Senior, T. J., Huxter, J. R., Allen, K., O’Neill, J. & Csicsvari, J. Gamma oscillatory firing reveals distinct populations of pyramidal cells in the CA1 region of the hippocampus. *J. Neurosci.* **28**, 2274–86 (2008).
  64. Zheng, C., Bieri, K. W., Hsiao, Y.-T. & Colgin, L. L. Spatial Sequence Coding Differs during Slow and Fast Gamma Rhythms in the Hippocampus. *Neuron* 1–11 (2016).  
doi:10.1016/j.neuron.2015.12.005
  65. Bieri, K. W., Bobbitt, K. N. & Colgin, L. L. Slow and fast  $\gamma$  rhythms coordinate different spatial coding modes in hippocampal place cells. *Neuron* **82**, 670–81 (2014).
  66. Gupta, A. S., van der Meer, M. A. A., Touretzky, D. S. & Redish, A. D. Segmentation of spatial experience by hippocampal  $\theta$  sequences. *Nat. Neurosci.* **15**, 1032–9 (2012).
  67. Takahashi, M., Nishida, H., Redish, A. D. & Lauwereyns, J. Theta phase shift in spike timing and modulation of gamma oscillation: a dynamic code for spatial alternation during fixation in rat hippocampal area CA1. *J. Neurophysiol.* **111**, 1601–14 (2014).

68. Shirvalkar, P. R., Rapp, P. R. & Shapiro, M. L. Bidirectional changes to hippocampal theta-gamma comodulation predict memory for recent spatial episodes. *Proc. Natl. Acad. Sci. U. S. A.* **107**, 7054–9 (2010).
69. Tort, A. B. L., Komorowski, R. W., Manns, J. R., Kopell, N. J. & Eichenbaum, H. Theta-gamma coupling increases during the learning of item-context associations. *Proc. Natl. Acad. Sci. U. S. A.* **106**, 20942–7 (2009).
70. Trimper, J. B., Stefanescu, R. A. & Manns, J. R. Recognition memory and theta-gamma interactions in the hippocampus. *Hippocampus* **24**, 341–53 (2014).
71. Yamamoto, J., Suh, J., Takeuchi, D. & Tonegawa, S. Successful execution of working memory linked to synchronized high-frequency gamma oscillations. *Cell* **157**, 845–57 (2014).
72. Wilson, M. A. & McNaughton, B. Reactivation of hippocampal ensemble memories during sleep. *Science* **265**, 676–679 (1994).
73. Lee, A. K. & Wilson, M. A. Memory of Sequential Experience in the Hippocampus during Slow Wave Sleep. *Neuron* **36**, 1183–1194 (2002).
74. Diba, K. & Buzsáki, G. Forward and reverse hippocampal place-cell sequences during ripples. *Nat. Neurosci.* **10**, 1241–2 (2007).
75. Buzsáki, G., Horváth, Z., Urioste, R., Hetke, J. & Wise, K. High-frequency network oscillation in the hippocampus. *Science* **256**, 1025–1027 (1992).
76. Ylinen, A., Bragin, A., Nádasdy, Z., Jandó, G., Szabó, I., Sik, A. & Buzsáki, G. Sharp wave-associated high-frequency oscillation (200 Hz) in the intact hippocampus: network and intracellular mechanisms. *J. Neurosci.* **15**, 30–46 (1995).
77. Csicsvari, J., Hirase, H., Czurkó, A., Mamiya, A. & Buzsáki, G. Fast network oscillations

- in the hippocampal CA1 region of the behaving rat. *J. Neurosci.* **19**, RC20 (1999).
78. Nakashiba, T., Buhl, D. L., McHugh, T. J. & Tonegawa, S. Hippocampal CA3 output is crucial for ripple-associated reactivation and consolidation of memory. *Neuron* **62**, 781–7 (2009).
79. Vandecasteele, M., Varga, V., Berényi, A., Papp, E., Barthó, P., Venance, L., Freund, T. F. & Buzsáki, G. Optogenetic activation of septal cholinergic neurons suppresses sharp wave ripples and enhances theta oscillations in the hippocampus. *Proc. Natl. Acad. Sci. U. S. A.* **111**, 13535–40 (2014).
80. Sullivan, D., Csicsvari, J., Mizuseki, K., Montgomery, S. M., Diba, K. & Buzsáki, G. Relationships between hippocampal sharp waves, ripples, and fast gamma oscillation: influence of dentate and entorhinal cortical activity. *J. Neurosci.* **31**, 8605–16 (2011).
81. Schomburg, E. W., Anastassiou, C. A., Buzsáki, G. & Koch, C. The spiking component of oscillatory extracellular potentials in the rat hippocampus. *J. Neurosci.* **32**, 11798–811 (2012).
82. Buzsáki, G. Hippocampal sharp waves: their origin and significance. *Brain Res.* **398**, 242–52 (1986).
83. Girardeau, G., Benchenane, K., Wiener, S. I., Buzsáki, G. & Zugaro, M. B. Selective suppression of hippocampal ripples impairs spatial memory. *Nat. Neurosci.* **12**, 1222–1223 (2009).
84. Ego-Stengel, V. & Wilson, M. A. Disruption of ripple-associated hippocampal activity during rest impairs spatial learning in the rat. *Hippocampus* **20**, 1–10 (2010).
85. Jadhav, S. P., Kemere, C., German, P. W. & Frank, L. M. Awake Hippocampal Sharp-Wave Ripples Support Spatial Memory. *Science* **336**, 1454–1458 (2012).

86. Davidson, T. J., Kloosterman, F. & Wilson, M. A. Hippocampal Replay of Extended Experience. *Neuron* **63**, 497–507 (2009).
87. Karlsson, M. P. & Frank, L. M. Awake replay of remote experiences in the hippocampus. *Nat. Neurosci.* **12**, 913–8 (2009).
88. Pfeiffer, B. E. & Foster, D. J. Hippocampal place-cell sequences depict future paths to remembered goals. *Nature* **497**, 74–9 (2013).
89. Witton, J., Staniaszek, L. E., Bartsch, U., Randall, A. D., Jones, M. W. & Brown, J. T. Disrupted hippocampal sharp-wave ripple-associated spike dynamics in a transgenic mouse model of dementia. *J Physiol* **594**, 4615–30 (2014).
90. Ciupek, S. M., Cheng, J., Ali, Y. O., Lu, H.-C. & Ji, D. Progressive Functional Impairments of Hippocampal Neurons in a Tauopathy Mouse Model. *J. Neurosci.* **35**, 8118–8131 (2015).
91. Nicole, O., Hadzibegovic, S., Gajda, J., Bontempi, B., Bem, T. & Meyrand, P. Soluble amyloid beta oligomers block the learning-induced increase in hippocampal sharp wave-ripple rate and impair spatial memory formation. *Sci. Rep.* **6**, 22728 (2016).
92. Cheng, J. & Ji, D. Rigid firing sequences undermine spatial memory codes in a neurodegenerative mouse model. *Elife* **2**, e00647 (2013).
93. Cacucci, F., Yi, M., Wills, T. J., Chapman, P. & O’Keefe, J. Place cell firing correlates with memory deficits and amyloid plaque burden in Tg2576 Alzheimer mouse model. *Proc. Natl. Acad. Sci. U. S. A.* **105**, 7863–8 (2008).
94. Axmacher, N., Elger, C. E. & Fell, J. Ripples in the medial temporal lobe are relevant for human memory consolidation. *Brain* **131**, 1806–17 (2008).
95. Carr, M. F., Karlsson, M. P. & Frank, L. M. Transient Slow Gamma Synchrony



- Underlies Hippocampal Memory Replay. *Neuron* **75**, 700–713 (2012).
96. Pfeiffer, B. E. & Foster, D. J. Autoassociative dynamics in the generation of sequences of hippocampal place cells. *Science* **349**, 180–183 (2015).
  97. Wilson, M. A., Varela, C. & Remondes, M. Phase organization of network computations. *Curr. Opin. Neurobiol.* **31C**, 250–253 (2015).
  98. Palop, J. J. & Mucke, L. Epilepsy and cognitive impairments in Alzheimer disease. *Arch Neurol* **66**, 435–440 (2009).
  99. Davies, P., Katzman, R. & Terry, R. D. Reduced somatostatin-like immunoreactivity in cerebral cortex from cases of Alzheimer disease and Alzheimer senile dementia. *Nature* **288**, 279–280 (1980).
  100. Chan-Palay, V. Somatostatin immunoreactive neurons in the human hippocampus and cortex shown by immunogold/silver intensification on vibratome sections: coexistence with neuropeptide Y neurons, and effects in Alzheimer-type dementia. *J. Comp. Neurol.* **260**, 201–23 (1987).
  101. Grouselle, D., Winsky-Sommerer, R., David, J. P., Delacourte, A., Dournaud, P. & Epelbaum, J. Loss of somatostatin-like immunoreactivity in the frontal cortex of Alzheimer patients carrying the apolipoprotein epsilon 4 allele. *Neurosci Lett* **255**, 21–24 (1998).
  102. Ruediger, S., Vittori, C., Bednarek, E., Genoud, C., Strata, P., Sacchetti, B. & Caroni, P. Learning-related feedforward inhibitory connectivity growth required for memory precision. *Nature* **473**, 514–518 (2011).
  103. Hu, J.-H., Ma, Y.-H., Jiang, J., Yang, N., Duan, S., Jiang, Z.-H., Mei, Z.-T., Fei, J. & Guo, L.-H. Cognitive impairment in mice over-expressing gamma-aminobutyric acid

- transporter 1 (GAT1). *Neuroreport* **15**, 9–12 (2004).
104. Whittington, M. A., Traub, R. D., Kopell, N., Ermentrout, B. & Buhl, E. H. Inhibition-based rhythms: experimental and mathematical observations on network dynamics. *Int. J. Psychophysiol.* **38**, 315–36 (2000).
  105. Colgin, L. L. Rhythms of the hippocampal network. *Nat. Rev. Neurosci.* **17**, 239–249 (2016).
  106. Marshall, L., Henze, D. A., Hirase, H., Leinekugel, X., Dragoi, G. & Buzsáki, G. Hippocampal pyramidal cell-interneuron spike transmission is frequency dependent and responsible for place modulation of interneuron discharge. *J. Neurosci.* **22**, RC197 (2002).
  107. Maurer, A. P., Cowen, S. L., Burke, S. N., Barnes, C. A. & McNaughton, B. L. Phase precession in hippocampal interneurons showing strong functional coupling to individual pyramidal cells. *J. Neurosci.* **26**, 13485–92 (2006).
  108. Ego-Stengel, V. & Wilson, M. A. Spatial selectivity and theta phase precession in CA1 interneurons. *Hippocampus* **17**, 161–74 (2007).
  109. Freund, T. F. & Buzsáki, G. Interneurons of the hippocampus. *Hippocampus* **6**, 347–470 (1998).
  110. Jinno, S. & Kosaka, T. Patterns of expression of neuropeptides in GABAergic nonprincipal neurons in the mouse hippocampus: Quantitative analysis with optical disector. *J. Comp. Neurol.* **461**, 333–49 (2003).
  111. Jinno, S. & Kosaka, T. Immunocytochemical characterization of hippocamposeptal projecting GABAergic nonprincipal neurons in the mouse brain: a retrograde labeling study. *Brain Res.* **945**, 219–31 (2002).

112. Gulyás, A. I., Hajos, N., Katona, I. & Freund, T. F. Interneurons are the local targets of hippocampal inhibitory cells which project to the medial septum. *Eur. J. Neurosci.* **17**, 1861–1872 (2003).
113. Melzer, S., Michael, M., Caputi, A., Eliava, M., Fuchs, E. C., Whittington, M. A. & Monyer, H. Long-range-projecting GABAergic neurons modulate inhibition in hippocampus and entorhinal cortex. *Science* **335**, 1506–10 (2012).
114. Tóth, K., Freund, T. F. & Miles, R. Disinhibition of rat hippocampal pyramidal cells by GABAergic afferents from the septum. *J. Physiol.* **500**, 463–474 (1997).
115. Léránth, C. & Frotscher, M. Cholinergic innervation of hippocampal GAD- and somatostatin-immunoreactive commissural neurons. *J. Comp. Neurol.* **261**, 33–47 (1987).
116. Dragoi, G., Carpi, D., Recce, M. L., Csicsvari, J. & Buzsáki, G. Interactions between hippocampus and medial septum during sharp waves and theta oscillation in the behaving rat. *J Neurosci* **19**, 6191–6199 (1999).
117. Klausberger, T., Magill, P. J., Márton, L. F., Roberts, J. D. B., Cobden, P. M., Buzsáki, G. & Somogyi, P. Brain-state- and cell-type-specific firing of hippocampal interneurons in vivo. *Nature* **421**, 844–8 (2003).
118. Varga, C., Golshani, P. & Soltesz, I. Frequency-invariant temporal ordering of interneuronal discharges during hippocampal oscillations in awake mice. *Proc. Natl. Acad. Sci. U. S. A.* **109**, E2726-34 (2012).
119. Tort, A. B. L., Rotstein, H. G., Dugladze, T., Gloveli, T. & Kopell, N. J. On the formation of gamma-coherent cell assemblies by oriens lacunosum-moleculare interneurons in the hippocampus. *Proc. Natl. Acad. Sci. U. S. A.* **104**, 13490–5 (2007).
120. Leão, R. N., Mikulovic, S., Leão, K. E., Munguba, H., Gezelius, H., Enjin, A., Patra, K.,

- Eriksson, A., Loew, L. M., Tort, A. B. L. & Kullander, K. OLM interneurons differentially modulate CA3 and entorhinal inputs to hippocampal CA1 neurons. *Nat. Neurosci.* **15**, 1524–30 (2012).
121. Jinno, S., Klausberger, T., Marton, L. F., Dalezios, Y., Roberts, J. D. B., Fuentealba, P., Bushong, E. A., Henze, D., Buzsáki, G. & Somogyi, P. Neuronal diversity in GABAergic long-range projections from the hippocampus. *J. Neurosci.* **27**, 8790–804 (2007).
122. Katona, L., Lapray, D., Viney, T. J., Oulhaj, A., Borhegyi, Z., Micklem, B. R., Klausberger, T. & Somogyi, P. Sleep and movement differentiates actions of two types of somatostatin-expressing GABAergic interneuron in rat hippocampus. *Neuron* **82**, 872–86 (2014).
123. Johansen, F. F., Zimmer, J. & Diemer, N. H. Early loss of somatostatin neurons in dentate hilus after cerebral ischemia in the rat precedes CA-1 pyramidal cell loss. *Acta Neuropathol* **73**, 110–114 (1987).
124. Buttini, M., Orth, M., Bellosta, S., Akeefe, H., Pitas, R. E., Wyss-Coray, T., Mucke, L. & Mahley, R. W. Expression of human apolipoprotein E3 or E4 in the brains of Apoe<sup>-/-</sup> mice: isoform-specific effects on neurodegeneration. *J. Neurosci.* **19**, 4867–4880 (1999).
125. Spiegel, A. M., Koh, M. T., Vogt, N. M., Rapp, P. R. & Gallagher, M. Hilar interneuron vulnerability distinguishes aged rats with memory impairment. *J. Comp. Neurol.* **521**, 3508–3523 (2013).
126. Jinno, S. & Kosaka, T. Patterns of expression of calcium binding proteins and neuronal nitric oxide synthase in different populations of hippocampal GABAergic neurons in mice. *J. Comp. Neurol.* **449**, 1–25 (2002).
127. Tukker, J. J., Fuentealba, P., Hartwich, K., Somogyi, P. & Klausberger, T. Cell type-

- specific tuning of hippocampal interneuron firing during gamma oscillations in vivo. *J. Neurosci.* **27**, 8184–9 (2007).
128. Penttonen, M., Kamondi, A., Acsády, L. & Buzsáki, G. Gamma frequency oscillation in the hippocampus of the rat: intracellular analysis in vivo. *Eur. J. Neurosci.* **10**, 718–728 (1998).
129. Sik, A., Penttonen, M., Ylinen, A., Buzsáki, G., Wise, K. & Buzsáki, G. Hippocampal CA1 interneurons: an in vivo intracellular labeling study. *J. Neurosci.* **15**, 6651–65 (1995).
130. Chiang, P. H., Yeh, W. C., Lee, C. T., Weng, J. Y., Huang, Y. Y. & Lien, C. C. M(1)-like muscarinic acetylcholine receptors regulate fast-spiking interneuron excitability in rat dentate gyrus. *Neuroscience* **169**, 39–51 (2010).
131. Murray, A. J., Sauer, J. F., Riedel, G., McClure, C., Ansel, L., Cheyne, L., Bartos, M., Wisden, W. & Wulff, P. Parvalbumin-positive CA1 interneurons are required for spatial working but not for reference memory. *Nat Neurosci* **14**, 297–299 (2011).
132. Somogyi, P., Katona, L., Klausberger, T., Lasztóczy, B. & Viney, T. J. Temporal redistribution of inhibition over neuronal subcellular domains underlies state-dependent rhythmic change of excitability in the hippocampus. *Philos. Trans. R. Soc. Lond. B. Biol. Sci.* **369**, 20120518 (2014).
133. Schönberger, J., Draguhn, A. & Both, M. Lamina-specific contribution of glutamatergic and GABAergic potentials to hippocampal sharp wave-ripple complexes. *Front. Neural Circuits* **8**, 103 (2014).
134. Stark, E., Roux, L., Eichler, R., Senzai, Y., Royer, S. S. & Buzsáki, G. Pyramidal Cell-Interneuron Interactions Underlie Hippocampal Ripple Oscillations. *Neuron* **83**, 467–480

- (2014).
135. Ellender, T. J., Nissen, W., Colgin, L. L., Mann, E. O. & Paulsen, O. Priming of hippocampal population bursts by individual perisomatic-targeting interneurons. *J. Neurosci.* **30**, 5979–91 (2010).
  136. Schlingloff, D., Káli, S., Freund, T. F., Hájos, N. & Gulyás, A. I. Mechanisms of sharp wave initiation and ripple generation. *J. Neurosci.* **34**, 11385–98 (2014).
  137. Savanthrapadian, S., Meyer, T., Elgueta, C., Booker, S. A., Vida, I. & Bartos, M. Synaptic properties of SOM- and CCK-expressing cells in dentate gyrus interneuron networks. *J. Neurosci.* **34**, 8197–209 (2014).
  138. Losonczy, A., Zemelman, B. V., Vaziri, A. & Magee, J. C. Network mechanisms of theta related neuronal activity in hippocampal CA1 pyramidal neurons. *Nat. Neurosci.* **13**, 967–72 (2010).
  139. Royer, S., Zemelman, B. V., Losonczy, A., Kim, J., Chance, F., Magee, J. C. & Buzsáki, G. Control of timing, rate and bursts of hippocampal place cells by dendritic and somatic inhibition. *Nat. Neurosci.* **15**, 769–75 (2012).

## **CHAPTER I**

### **Apolipoprotein E4, Inhibitory Network Dysfunction, and Alzheimer's Disease**

## **Abstract**

Apolipoprotein (apo) E4 is the major genetic risk factor for Alzheimer's disease (AD), increasing risk and decreasing age of disease onset. Many studies have demonstrated the detrimental effects of apoE4 in varying cellular contexts. However, the underlying mechanisms explaining how apoE4 leads to cognitive decline are not fully understood. In this review, we provide an overview of the literature describing apoE4's detrimental effects in the central nervous system (CNS), specifically focusing on its contribution to neuronal subtype dysfunction or loss. We focus on  $\gamma$ -aminobutyric acid (GABA)-expressing interneurons in the hippocampus, which are selectively vulnerable to apoE4-mediated neurotoxicity. Additionally, we discuss the importance of the GABAergic inhibitory network to proper cognitive function and how dysfunction of this network manifests in AD. Finally, we examine how apoE4-mediated GABAergic interneuron loss can lead to inhibitory network deficits and how this deficit results in cognitive decline. We propose the following working model: aging and/or stress induces neuronal expression of apoE. GABAergic interneurons are selectively vulnerable to intracellularly produced apoE4, through a tau dependent mechanism, which leads to their dysfunction and eventual death. In turn, GABAergic interneuron loss causes hyperexcitability and dysregulation of neural networks in the hippocampus and cortex. This dysfunction results in learning, memory, and other cognitive deficits that are the central features of AD.



## Main Text

### Inhibitory System Dysfunction in AD

In recent years, it has become clear that neurodegenerative diseases target specific neuronal populations<sup>1</sup>. GABAergic interneuron dysfunction, in particular, is found in a range of neurological and psychiatric disorders, including schizophrenia, autism, Fragile X syndrome, epilepsy, migraines, depression, bipolar disorder, and AD<sup>2</sup>. Loss of GABA, the primary inhibitory neurotransmitter in the brain, is a key component of AD. Post-mortem tissue from AD patients shows reduced GABA level throughout the brain, particularly in temporal, parietal, and frontal cortices<sup>3,4</sup>. Post-mortem cortices from AD patients contain reduced GABAergic terminals, particularly near amyloid plaques<sup>5,6</sup>. AD patients show reduced cortical GABA as measured by positron emission tomography, especially in the temporal cortex<sup>7,8</sup>, and reduced GABA in cerebrospinal fluid<sup>9-12</sup>. Additionally, AD patients have a specific loss of somatostatin-positive interneurons in the cortex<sup>13</sup> and hippocampus<sup>14</sup>. Several other neuronal subtypes are also affected by AD pathology, including cholinergic and glutamatergic neurons, whose loss and dysfunction in turn contribute to cognitive impairment<sup>15</sup>. This review will focus on the consequences of GABAergic interneuron loss and dysfunction, which have broad consequences at the network and behavioral level.

Loss of GABA and GABAergic interneurons in AD patients may be responsible for network hyperactivity manifesting as seizures. Substantial evidence shows that loss of GABAergic tone leads to seizures<sup>16</sup>. 10–22% of AD patients exhibit seizures<sup>17-19</sup>, as do hAPP<sub>FAD</sub> mice<sup>20</sup>, and the onset of these seizures precedes cognitive decline<sup>21</sup>. Levetiracetam, an anti-epileptic drug, successfully reverses hyperexcitability and learning and memory deficits in an hAPP<sub>FAD</sub> mouse model of AD<sup>22,23</sup> and in aged mice<sup>24-26</sup>. Cognitively normal elderly, amnesic mild cognitive

impairment (MCI), and AD patients all show cognitive improvement following chronic levetiracetam administration<sup>27-29</sup>. Thus, GABAergic dysfunction contributes to network-wide deficits in AD, which may in turn harm cognition.

GABAergic inhibitory interneurons make up a minority of neurons within the brain but play an outsized role in coordinating activity<sup>30</sup>. Inhibitory interneurons regulate network oscillations, which synchronize neuronal activity to rhythms that are crucial to learning and memory<sup>31-35</sup>. Inhibition also prevents hyperactivity of excitatory principal cells, which disrupts normally sparse neural coding and leads to decreased signal-to-noise ratio<sup>36-38</sup>. Furthermore, reducing hippocampal GABA levels impairs learning and memory<sup>39,40</sup>, and silencing inhibitory interneurons in the dentate gyrus prevents both encoding of new memories and recall of old memories<sup>41</sup>. Given their importance to proper learning and memory, it is crucial to better understand GABAergic inhibitory interneuron dysfunction and/or loss in the context of AD. As apoE4 is the major genetic risk factor for AD, understanding its effect on GABAergic interneurons, a population that is particularly vulnerable to apoE4 pathology, is essential. ApoE is expressed in neurons during periods of stress or normal aging. The neuronally expressed apoE4 is more susceptible to proteolytic cleavage and cytotoxic fragment generation. In the following sections, evidence for GABAergic interneuron susceptibility to apoE4 and the subsequent network deficits that result of inhibitory neuron loss, culminating in learning and memory deficits will be discussed.

### **GABAergic Interneuron Susceptibility to ApoE4**

Many lines of evidence from *in vivo* studies contribute to the hypothesis that GABAergic interneurons in the hippocampus are disproportionately susceptible to apoE4-mediated toxicity. For example, apoE4-KI mice display an age- and tau-dependent decrease in hilar GABAergic

somatostatin-positive interneurons in the hippocampus<sup>42</sup>. The extent of this inhibitory interneuron loss correlates with both decreased adult hippocampal neurogenesis and with learning and memory deficits<sup>43,44</sup>. The adverse effects of apoE4 are prevented by tau removal, indicating a direct link between tau pathology, apoE4, and GABAergic interneuron death<sup>42</sup>. Interestingly, the cellular source of apoE is critical to its pathological effect on GABAergic interneurons. ApoE4 undergoes proteolytic cleavage which generates neurotoxic fragments only when produced in neurons, but not when produced in astrocytes<sup>45</sup>. When expressed in neurons, apoE3 is excitoprotective whereas apoE4 is not; however, when expressed in astrocytes, apoE3 and apoE4 are equally excitoprotective<sup>46</sup>. Likewise, when expressed in neurons, apoE4 decreases dendrite arborization and spine density whereas apoE4 expressed in astrocytes does not show similar effects<sup>47</sup>. Importantly, deletion of apoE4 in GABAergic interneurons, but not deletion of apoE4 in astrocytes, is sufficient to protect aged mice from apoE4-induced GABAergic interneuron loss and learning and memory deficits<sup>48</sup>. These findings suggest that, although the majority of apoE is produced in astrocytes, it is apoE4 produced within GABAergic interneurons that is detrimental to their survival *in vivo* which leads to deficits in both learning and memory in AD models. Strikingly, bolstering inhibitory function, either through systemic GABA-agonist treatment<sup>49</sup> or through transplant of mouse derived inhibitory interneuron progenitors directly into the hippocampus<sup>50</sup>, restores learning and memory in aged apoE4-KI mice without or with mutant hAPP<sub>FAD</sub> expression.

### **ApoE4-Mediated GABAergic Interneuron Loss and Inhibitory Network Dysfunction in AD**

Given that hippocampal GABAergic interneurons are selectively vulnerable to apoE4, an intriguing question is: how does interneuron dysfunction manifest at the network and behavioral

or clinical levels? At the network level, loss of GABAergic function can lead to deficits in both tonic and phasic inhibition. Loss of tonic inhibition manifests itself most prominently in AD patients as hypersynchrony, leading to epilepsy and olfactory processing deficits, as well as hyperactivity, leading to aberrantly increased activation of cortical and hippocampal networks<sup>51</sup>. Loss of phasic inhibition manifests as reduced hippocampal rhythms<sup>51</sup>. These network consequences of inhibitory deficits each contribute to learning and memory impairments<sup>52</sup>. The following sections will address these manifestations of inhibitory network dysfunction that occur as a result of apoE4 expression.

#### ***ApoE4 and GABAergic Interneuron Dysfunction Leading to Seizure Activity in AD***

The loss of GABA and GABAergic interneurons in AD patients may lead to network hyperactivity, most commonly observed through seizures. ApoE4 carriers have a higher risk<sup>53-57</sup> and earlier onset<sup>58-60</sup> of developing idiopathic or secondary temporal lobe epilepsy. It is still unclear whether these patients demonstrate a higher risk for developing AD later in life, or if indeed the proportion of AD patients with concomitant epilepsy is enriched for apoE4 carriers. In addition to increased risk, apoE4 is also associated with increased epileptic pathology. The presence of apoE4 is correlated with smaller neuron size and increased DNA damage in temporal lobes of epilepsy patients<sup>61</sup>, and epilepsy patients with at least one *APOE4* allele are six times more likely to exhibit treatment resistance<sup>62</sup>. Investigating the connection between apoE4 and epilepsy may shed light on its role in large scale network dysfunction in AD.

### ***ApoE4-Mediated GABAergic Interneuron Dysfunction and Olfactory Deficits in AD***

Olfactory dysfunction is also an early and common symptom of AD as well as a result of carrying apoE4 and odor identification ability predicts future cognitive decline<sup>63–66</sup>, making olfactory acuity a potential early signal of underlying neurodegenerative processes. ApoE4 carriers show particularly marked deficits in odor identification and memory relative to non-carriers<sup>67</sup>, and evidence suggests disrupted GABA signaling in the olfactory bulb may mediate this olfactory loss<sup>68</sup>. *In vivo* electrophysiological recordings from aged apoE4-KI mice with odor memory deficits revealed increased local field potential response to odors in both the olfactory bulb and in primary olfactory cortex<sup>69</sup>, which was attributed to inhibitory dysfunction. These studies together suggest that apoE4-mediated odor memory impairment, a potential early biomarker of cognitive dysfunction, may be due to apoE4-induced hyperactivity.

### ***ApoE4 and Microglial Dysfunction in the GABAergic Inhibitory Network and AD***

The link between apoE, microglia, and GABAergic interneuron dysfunction is also an emerging area of interest in the context of network dysfunction and AD. ApoE expression in microglia and its roles in microglial physiology and pathology have recently been actively explored. ApoE is upregulated in primed/activated microglia<sup>70,71</sup>, and apoE signaling in microglia following phagocytosis of apoptotic neurons or in response to A $\beta$  accumulation leads to a transcriptional switch from promoting homeostasis to promoting inflammation and neurodegeneration<sup>71,72</sup>. Deletion of the *ApoE* gene suppresses microglial activation in response to A $\beta$  accumulation and prevents migration of microglia toward amyloid plaques<sup>71</sup>. However, the effect of specific apoE isoforms has yet to be explored<sup>73,74</sup>. It has been reported that activated microglia migrate to inhibitory synapses and displace them from excitatory neurons<sup>75</sup> and an increase in CX3CR1

expression in activated microglia suppresses GABA<sub>A</sub> receptor signaling in excitatory neurons<sup>76</sup>, both of which could contribute to GABAergic inhibitory network deficits in the context of apoE4. Another avenue by which microglial dysfunction may affect GABAergic interneurons is through perineuronal nets. Perineuronal nets are extracellular matrix structures which surround synapses of highly active neuronal subtypes and are associated with microglia<sup>77</sup>. These structures are involved in synapse development, stabilization and remodeling, buffering ions, and regulating the synapse microenvironment<sup>78</sup>. AD patients have reduced perineuronal net density<sup>79</sup>. Strikingly, the majority of neurons surrounded by perineuronal nets are parvalbumin-expressing GABAergic interneurons<sup>80</sup>, and these interneurons show deficits in perineuronal net density in AD model of mice<sup>81</sup>. Since perineuronal nets protect these interneurons from oxidative stress and other injuries<sup>82</sup>, it is possible that their breakdown in AD, which can be triggered or exacerbated by microglial dysfunction, may lead to interneuron dysfunction or death and thus inhibitory network deficits.

### ***ApoE4 and Network Hyperactivity Induced by GABAergic Interneuron Dysfunction***

Network hyperactivity is an overarching symptom of AD and is evident in human apoE4 carriers. More specifically, hyperactivity in two networks which are normally disengaged during task performance in healthy individuals has been demonstrated by multiple groups. First, cognitively normal apoE4 carriers show reduced task-induced deactivation of the default mode network (DMN)<sup>83-85</sup>. Higher resting state GABA levels in the DMN are associated with enhanced task-induced deactivation of this network<sup>86-88</sup>, suggesting that this DMN hyperactivity could be the result of inhibitory deficits. Reduced ability to deactivate the DMN during memory encoding is found in AD patients<sup>89-91</sup> and is correlated with worse task performance<sup>92</sup>, linking this apoE4-

induced deficit to memory impairments. Second, healthy elderly apoE4 carriers show increased hippocampal and entorhinal activation during encoding task performance<sup>93,94</sup>. A recent study found that aged apoE4-KI mice had increased field potential synchrony and pyramidal cell firing in the entorhinal cortex<sup>95</sup>. This activation is dysfunctional hyperactivity rather than task-related, as levetiracetam treatment of amnesic MCI patients both reduces hippocampal over-activation and improves cognitive performance during a recognition memory task<sup>28,96</sup>. Greater hippocampal activation during encoding tasks is associated with worse task performance<sup>97</sup> in MCI and AD patients<sup>93,98</sup>, and even predicts future cognitive decline in cognitively healthy elderly<sup>99</sup>. Finally, aberrant activity increases in these networks are seen even prior to aging. Healthy young and middle-aged adult apoE4 carriers show increased DMN activation at rest<sup>100</sup> and increased hippocampal activation during encoding task performance<sup>100-102</sup>, suggesting that apoE4-induced network hyperactivity occurs before significant A $\beta$  accumulation in human brains.

### ***ApoE4-Mediated GABAergic Interneuron Loss and Hippocampal Network Dysfunction and Memory Deficits***

Susceptibility of GABAergic interneurons to apoE4 and subsequent loss of inhibitory function can also lead to reduced coordination of hippocampal network activity involved in memory. ApoE4-KI mice show reduced abundance of sharp-wave ripples, the local field potential of hippocampal replay events which are critical for consolidating spatial memory<sup>103,104</sup>. ApoE4-KI mice also display reduced slow gamma power throughout the hippocampal circuit during ripple events, suggesting reduced accuracy of these replay events<sup>103,105</sup>. Thus, apoE4 leads to reduced instances as well as accuracy of spatial memory consolidation. Notably, removing apoE4 from inhibitory interneurons specifically rescues slow gamma power and learning and memory deficits, indicating

that these phenotypes are caused by intraneuronal apoE4 expressed in GABAergic interneurons. Younger mice recorded before the onset of significant interneuron loss do not show significant slow gamma power loss, further implicating inhibitory interneurons in apoE4-induced hippocampal gamma loss<sup>103</sup>.

## Conclusions and Perspectives

The combination of the data presented above paints a more complete picture of the mechanism underlying apoE4 mediated cognitive decline. We present a model wherein injury or aging-related stress induces neuronal apoE expression. Due to its pathological conformation (domain interaction), apoE4 is more susceptible to proteolytic cleavage than apoE3, leading to increased levels of neurotoxic fragment generation, and through a tau-dependent mechanism, results in GABAergic interneuron dysfunction and death. The loss of hippocampal GABAergic interneurons leads to network dysfunction and hyperexcitability. The network dysfunction and hyperexcitability themselves contribute to learning and memory deficits as well as induce further stress, and therefore more neuronal expression of apoE. This process culminates in further GABAergic interneuron loss and eventual cognitive decline.

Several approaches could be further developed for treating apoE4-mediated pathologies or GABAergic dysfunction. First, apoE4-mediated GABAergic deficits and cognitive decline could be treated with small molecules. For example, treating apoE4-KI mice with pentobarbital early in life prevents learning and memory deficits late in life<sup>49</sup>. Furthermore, the use of a structure corrector has been shown *in vitro* to ameliorate apoE4-mediated AD pathologies in hiPSC-derived neurons, including GABAergic neuron deficits<sup>106</sup>. However, developing new drugs for new targets can be prohibitively expensive. Using current screening methods it is possible to find combinations



of existing drugs that can correct pathological phenotypes of AD<sup>107,108</sup>. In the context of apoE4, it would be especially interesting to identify existing drugs that can enhance GABAergic interneuron function or can correct gene expression signatures in apoE4/4 neurons to a more ‘apoE3/3-like’ profile.

Several treatments which enhance inhibition have been tested in animal models and in clinical trials. GABA<sub>A</sub> receptor potentiators or agonists ameliorate apoE4- or amyloid-induced toxicity and improve cognition in rodent models of AD and normal aging<sup>109,110</sup>. However, across several clinical trials, these agents have produced behavioral, but not cognitive, improvements<sup>4</sup>. Unfortunately, these therapeutics produce undesirable side effects which limit long-term use<sup>111,112</sup>. Anti-epileptic agents similarly show promise in animal models<sup>22,23</sup>, but have not produced cognitive improvements in clinical trials<sup>4</sup>, with the exception of levetiracetam that improved MCI and reduced hippocampal hyperactivity in initial clinical studies<sup>96,113–115</sup>. However, trials for both of these therapeutics used only small cohorts over short treatment periods, so further study in larger clinical trials is required. Moreover, specifically targeted therapies might be more beneficial. For instance, theta burst stimulation via transcranial magnetic stimulation has been used successfully to increase GABA within the DMN<sup>116</sup>. This could be used to rescue specific network pathologies rather than globally increasing inhibition.

Driving specific interneuron populations could be used to rescue network synchrony. Two foundational optogenetic studies demonstrated that optogenetically driving inhibitory interneurons specifically enhances slow gamma frequency oscillations throughout cortex, reducing circuit noise while amplifying circuit signal<sup>117,118</sup>. Non-invasive stimulation can augment endogenous network oscillations to enhance learning and memory. In humans, transcranial magnetic stimulation enhances cortical slow waves and thus improve task performance<sup>119</sup>. In mice, slow gamma

frequency visual or audio input entrains neural firing to this frequency in the cortex and hippocampus and reduces A $\beta$  pathology and microglial abnormalities<sup>120,121</sup>. Finally, enhancing activity of existing interneurons could also attenuate the network effects. For example, exogenous neuregulin 1 increases excitability of parvalbumin-positive interneurons<sup>122</sup> and has been used to restore hippocampal theta synchrony and fear conditioning in a mouse model of schizophrenia, which showed inhibitory impairments<sup>123</sup>.

In addition to targeting susceptibility of GABAergic interneurons to apoE4 and the subsequent network hyperexcitability that results from inhibitory neuron loss, another potential therapy is to replace the lost population of GABAergic interneurons. Cell replacement therapy has been explored in the context of various neurodegenerative diseases<sup>124-127</sup>. Notably, it has been shown that GABAergic interneuron progenitor transplantation has potential to be an effective method to correct seizure activity in an epilepsy model<sup>128</sup>. Likewise, transplantation of mouse MGE-derived GABAergic progenitors into aged apoE4-KI mice without or with A $\beta$  accumulation rescues learning and memory deficits<sup>50</sup>. Furthermore, transplanting Nav1.1-overexpressing interneurons derived from the mouse MGE into an hAPP<sub>FAD</sub> mouse model enhances behavior-dependent gamma oscillatory activity, reduces network hypersynchrony, and improves cognitive function<sup>129</sup>. In the future, it would be interesting to employ a similar cell therapeutic strategy, using hiPSC-derived GABAergic progenitors with an apoE3/3 genotype as donor cells for transplantation, to treat hyperexcitability and network deficits in an apoE4 model of AD.

Clearly, new hope for effective therapeutics of AD relies upon the ability of scientists to explore multiple lines of inquiry. Moving forward, it is certainly conceivable that there will be combination therapies implemented, with drugs targeting A $\beta$ , tau, inflammation, apoE4, and apoE4-induced GABAergic interneuron impairment.

## References

1. Fu, H., Hardy, J. & Duff, K. E. Selective vulnerability in neurodegenerative diseases. *Nat. Neurosci.* **21**, (2018).
2. Ramamoorthi, K. & Lin, Y. The contribution of GABAergic dysfunction to neurodevelopmental disorders. *Trends Mol. Med.* **17**, 452–62 (2011).
3. Govindpani, K., Guzmán, B. C.-F., Vinnakota, C., Waldvogel, H., Faull, R., Kwakowsky, A., Govindpani, K., Calvo-Flores Guzmán, B., Vinnakota, C., Waldvogel, H. J., Faull, R. L. & Kwakowsky, A. Towards a Better Understanding of GABAergic Remodeling in Alzheimer's Disease. *Int. J. Mol. Sci.* **18**, 1813 (2017).
4. Lanctôt, K. L., Herrmann, N., Mazzotta, P., Khan, L. R. & Ingber, N. GABAergic Function in Alzheimer's Disease: Evidence for Dysfunction and Potential as a Therapeutic Target for the Treatment of Behavioural and Psychological Symptoms of Dementia: <http://dx.doi.org/10.1177/070674370404900705> (2016).  
doi:10.1177/070674370404900705
5. Garcia-Marin, V., Blazquez-Llorca, L., Rodriguez, J.-R., Boluda, S., Muntane, G., Ferrer, I. & Defelipe, J. Diminished perisomatic GABAergic terminals on cortical neurons adjacent to amyloid plaques. *Front. Neuroanat.* **3**, 28 (2009).
6. Ramos-Miguel, A., Hercher, C., Beasley, C. L., Barr, A. M., Bayer, T. A., Falkai, P., Leurgans, S. E., Schneider, J. A., Bennett, D. A. & Honer, W. G. Loss of Munc18-1 long splice variant in GABAergic terminals is associated with cognitive decline and increased risk of dementia in a community sample. *Mol. Neurodegener.* **10**, 65 (2015).
7. Soricelli, A., Postiglione, A., Grivet-Fojaja, M. R., Mainenti, P. P., Discepolo, A., Varrone, A., Salvatore, M. & Lassen, N. A. Reduced cortical distribution volume of

- iodine-123 iomazenil in Alzheimer's disease as a measure of loss of synapses. *Eur. J. Nucl. Med.* **23**, 1323–8 (1996).
8. Fukuchi, K., Hashikawa, K., Seike, Y., Moriwaki, H., Oku, N., Ishida, M., Fujita, M., Uehara, T., Tanabe, H., Kusuoka, H. & Nishimura, T. Comparison of iodine-123-iomazenil SPECT and technetium-99m-HMPAO-SPECT in Alzheimer's disease. *J. Nucl. Med.* **38**, 467–70 (1997).
  9. Bareggi, S. R., Franceschi, M., Bonini, L., Zecca, L. & Smirne, S. Decreased CSF Concentrations of Homovanillic Acid and  $\gamma$ -Aminobutyric Acid in Alzheimer's Disease. Age- or Disease-Related Modifications? *Arch. Neurol.* **39**, 709 (1982).
  10. Zimmer, R., Teelken, A. W., Trieling, W. B., Weber, W., Weihmayr, T. & Lauter, H. - Aminobutyric Acid and Homovanillic Acid Concentration in the CSF of Patients With Senile Dementia of Alzheimer's Type. *Arch. Neurol.* **41**, 602–604 (1984).
  11. Manyam, N. V, Katz, L., Hare, T. A., Gerber, J. C. & Grossman, M. H. Levels of  $\gamma$ -Aminobutyric Acid in Cerebrospinal Fluid in Various Neurologic Disorders. *Arch. Neurol.* **37**, 352–5 (1980).
  12. Enna, S. J., Stern, L. Z., Wastek, G. J. & Yamamura, H. I. Cerebrospinal Fluid  $\gamma$ -Aminobutyric Acid Variations in Neurological Disorders. *Arch. Neurol.* **34**, 683–5 (1977).
  13. Davies, P., Katzman, R. & Terry, R. D. Reduced somatostatin-like immunoreactivity in cerebral cortex from cases of Alzheimer disease and Alzheimer senile dementia. *Nature* **288**, 279–280 (1980).
  14. Chan-Palay, V. Somatostatin immunoreactive neurons in the human hippocampus and cortex shown by immunogold/silver intensification on vibratome sections: coexistence with neuropeptide Y neurons, and effects in Alzheimer-type dementia. *J. Comp. Neurol.*

- 260**, 201–223 (1987).
15. Palmer, A. M. & Gershon, S. Is the neuronal basis of Alzheimer's disease cholinergic or glutamatergic ? *Faseb* **4**, 2745–2752 (1990).
  16. Treiman, D. M. GABAergic mechanisms in epilepsy. *Epilepsia* **42**, 8–12 (2001).
  17. Palop, J. J. & Mucke, L. Epilepsy and cognitive impairments in Alzheimer disease. *Arch Neurol* **66**, 435–440 (2009).
  18. Palop, J. J. & Mucke, L. Amyloid-B-induced neuronal dysfunction in Alzheimer's disease: From synapses toward neural networks. *Nat. Neurosci.* **13**, 812–818 (2010).
  19. Vossel, K. A., Beagle, A. J., Rabinovici, G. D., Shu, H., Lee, S. E., Naasan, G., Hegde, M., Cornes, S. B., Henry, M. L., Nelson, A. B., Seeley, W. W., Geschwind, M. D., Gorno-Tempini, M. L., Shih, T., Kirsch, H. E., Garcia, P. A., Miller, B. L. & Mucke, L. Seizures and epileptiform activity in the early stages of Alzheimer disease. *JAMA Neurol.* **70**, 1158–1166 (2013).
  20. Palop, J. J., Chin, J., Roberson, E. D., Wang, J., Thwin, M. T., Bien-Ly, N., Yoo, J., Ho, K. O., Yu, G. Q., Kreitzer, A., Finkbeiner, S., Noebels, J. L. & Mucke, L. Aberrant Excitatory Neuronal Activity and Compensatory Remodeling of Inhibitory Hippocampal Circuits in Mouse Models of Alzheimer's Disease. *Neuron* **55**, 697–711 (2007).
  21. DiFrancesco, J. C., Tremolizzo, L., Polonia, V., Giussani, G., Bianchi, E., Franchi, C., Nobili, A., Appollonio, I., Beghi, E. & Ferrarese, C. Adult-Onset Epilepsy in Presymptomatic Alzheimer's Disease: A Retrospective Study. *J. Alzheimers. Dis.* **60**, 1267–1274 (2017).
  22. Sanchez, P. E., Zhu, L., Verret, L., Vossel, K. A., Orr, A. G., Cirrito, J. R., Devidze, N., Ho, K., Yu, G.-Q., Palop, J. J. & Mucke, L. Levetiracetam suppresses neuronal network

- dysfunction and reverses synaptic and cognitive deficits in an Alzheimer's disease model. *Proc. Natl. Acad. Sci.* **109**, E2895–E2903 (2012).
23. Shi, J.-Q., Wang, B.-R., Tian, Y.-Y., Xu, J., Gao, L., Zhao, S.-L., Jiang, T., Xie, H.-G. & Zhang, Y.-D. Antiepileptics Topiramate and Levetiracetam Alleviate Behavioral Deficits and Reduce Neuropathology in APP<sup>swe</sup>/PS1<sup>dE9</sup> Transgenic Mice. *CNS Neurosci. Ther.* **19**, 871–881 (2013).
  24. Koh, M. T., Haberman, R. P., Foti, S., McCown, T. J. & Gallagher, M. Treatment strategies targeting excess hippocampal activity benefit aged rats with cognitive impairment. *Neuropsychopharmacology* **35**, 1016–1025 (2010).
  25. Devi, L. & Ohno, M. Effects of levetiracetam, an antiepileptic drug, on memory impairments associated with aging and Alzheimer's disease in mice. *Neurobiol. Learn. Mem.* **102**, 7–11 (2013).
  26. Haberman, R. P., Branch, A. & Gallagher, M. Targeting Neural Hyperactivity as a Treatment to Stem Progression of Late-Onset Alzheimer's Disease. *Neurotherapeutics* **14**, 662–676 (2017).
  27. Schoenberg, M. R., Rum, R. S., Osborn, K. E. & Werz, M. A. A randomized, double-blind, placebo-controlled crossover study of the effects of levetiracetam on cognition, mood, and balance in healthy older adults. *Epilepsia* **58**, 1566–1574 (2017).
  28. Bakker, A., Krauss, G. L., Albert, M. S., Speck, C. L., Jones, L. R., Stark, C. E., Yassa, M. A., Bassett, S. S., Shelton, A. L. & Gallagher, M. Reduction of Hippocampal Hyperactivity Improves Cognition in Amnesic Mild Cognitive Impairment. *Neuron* **74**, 467–474 (2012).
  29. Cumbo, E. & Lorigi, L. D. Levetiracetam, lamotrigine, and phenobarbital in patients with

- epileptic seizures and Alzheimer's disease. *Epilepsy Behav.* **17**, 461–466 (2010).
30. Moore, R. Principles of Synaptic Transmission. *Ann. N. Y. Acad. Sci.* **695**, 1–9 (1993).
  31. Mongillo, G., Rumpel, S. & Loewenstein, Y. Inhibitory connectivity defines the realm of excitatory plasticity. *Nat. Neurosci.* **21**, 1463–1470 (2018).
  32. Cobb, S. R., Buhl, E. H., Halasy, K., Paulsen, O. & Somogyi, P. Synchronization of neuronal activity in hippocampus by individual GABAergic interneurons. *Nature* **378**, 75–8 (1995).
  33. Somogyi, P. & Klausberger, T. Defined types of cortical interneurone structure space and spike timing in the hippocampus. *J. Physiol.* **562**, 9–26 (2005).
  34. Xu, X., An, L., Mi, X. & Zhang, T. Impairment of Cognitive Function and Synaptic Plasticity Associated with Alteration of Information Flow in Theta and Gamma Oscillations in Melamine-Treated Rats. *PLoS One* **8**, e77796 (2013).
  35. Cardin, J. A. Inhibitory Interneurons Regulate Temporal Precision and Correlations in Cortical Circuits. *Trends Neurosci.* **41**, 689–700 (2018).
  36. Jones, M. W. & Wilson, M. A. Theta rhythms coordinate hippocampal-prefrontal interactions in a spatial memory task. *PLoS Biol.* **3**, e402 (2005).
  37. Mann, E. O., Kohl, M. M. & Paulsen, O. Distinct roles of GABA(A) and GABA(B) receptors in balancing and terminating persistent cortical activity. *J. Neurosci.* **29**, 7513–7518 (2009).
  38. Lehmann, K., Steinecke, A. & Bolz, J. GABA through the Ages: Regulation of Cortical Function and Plasticity by Inhibitory Interneurons. *Neural Plast.* **2012**, 1–11 (2012).
  39. Hu, J.-H., Ma, Y.-H., Jiang, J., Yang, N., Duan, S., Jiang, Z.-H., Mei, Z.-T., Fei, J. & Guo, L.-H. Cognitive impairment in mice over-expressing gamma-aminobutyric acid

- transporter 1 (GAT1). *Neuroreport* **15**, 9–12 (2004).
40. Prut, L., Prenosil, G., Willadt, S., Vogt, K., Fritschy, J.-M. & Crestani, F. A reduction in hippocampal GABAA receptor  $\alpha 5$  subunits disrupts the memory for location of objects in mice. *Genes, Brain Behav.* **9**, 478–488 (2010).
  41. Andrews-Zwilling, Y., Gillespie, A. K., Kravitz, A. V., Nelson, A. B., Devidze, N., Lo, I., Yoon, S. Y., Bien-Ly, N., Ring, K., Zwilling, D., Potter, G. B., Rubenstein, J. L. R., Kreitzer, A. C. & Huang, Y. Hilar GABAergic interneuron activity controls spatial learning and memory retrieval. *PLoS One* **7**, e40555 (2012).
  42. Andrews-Zwilling, Y., Bien-Ly, N., Xu, Q., Li, G., Bernardo, A., Yoon, S. Y., Zwilling, D., Yan, T. X., Chen, L. & Huang, Y. Apolipoprotein E4 causes age- and Tau-dependent impairment of GABAergic interneurons, leading to learning and memory deficits in mice. *J Neurosci* **30**, 13707–13717 (2010).
  43. Leung, L., Andrews-Zwilling, Y., Yoon, S. Y., Jain, S., Ring, K., Dai, J., Wang, M. M., Tong, L., Walker, D. & Huang, Y. Apolipoprotein E4 causes age- and sex-dependent impairments of hilar GABAergic interneurons and learning and memory deficits in mice. *PLoS One* **7**, e53569 (2012).
  44. Li, G., Bien-Ly, N., Andrews-Zwilling, Y., Xu, Q., Bernardo, A., Ring, K., Halabisky, B., Deng, C., Mahley, R. W. & Huang, Y. GABAergic interneuron dysfunction impairs hippocampal neurogenesis in adult apolipoprotein E4 knockin mice. *Cell Stem Cell* **5**, 634–645 (2009).
  45. Brecht, W. J., Harris, F. M., Chang, S., Tesseur, I., Yu, G.-Q., Xu, Q., Dee Fish, J., Wyss-Coray, T., Buttini, M., Mucke, L., Mahley, R. W. & Huang, Y. Neuron-Specific Apolipoprotein E4 Proteolysis Is Associated with Increased Tau Phosphorylation in



- Brains of Transgenic Mice. *J. Neurosci.* **24**, 2527–2534 (2004).
46. Buttini, M., Masliah, E., Yu, G.-Q., Palop, J. J., Chang, S., Bernardo, A., Lin, C., Wyss-Coray, T., Huang, Y. & Mucke, L. Cellular source of apolipoprotein E4 determines neuronal susceptibility to excitotoxic injury in transgenic mice. *Am. J. Pathol.* **177**, 563–9 (2010).
  47. Jain, S., Yoon, S. Y., Leung, L., Knoferle, J. & Huang, Y. Cellular source-specific effects of apolipoprotein (apo) E4 on dendrite arborization and dendritic spine development. *PLoS One* **8**, e59478 (2013).
  48. Knoferle, J., Yoon, S. Y., Walker, D., Leung, L., Gillespie, a. K., Tong, L. M., Bien-Ly, N. & Huang, Y. Apolipoprotein E4 Produced in GABAergic Interneurons Causes Learning and Memory Deficits in Mice. *J. Neurosci.* **34**, 14069–14078 (2014).
  49. Tong, L. M., Yoon, S. Y., Andrews-Zwilling, Y., Yang, A., Lin, V., Lei, H. & Huang, Y. Enhancing GABA Signaling during Middle Adulthood Prevents Age-Dependent GABAergic Interneuron Decline and Learning and Memory Deficits in ApoE4 Mice. *J. Neurosci.* **36**, 2316–2322 (2016).
  50. Tong, L. M., Djukic, B., Arnold, C., Gillespie, A. K., Yoon, S. Y., Wang, M. M., Zhang, O., Knoferle, J., Rubenstein, J. L. R., Alvarez-Buylla, A. & Huang, Y. Inhibitory interneuron progenitor transplantation restores normal learning and memory in ApoE4 knock-in mice without or with A $\beta$  accumulation. *J. Neurosci.* **34**, 9506–15 (2014).
  51. Lee, V. & Maguire, J. The impact of tonic GABA<sub>A</sub> receptor-mediated inhibition on neuronal excitability varies across brain region and cell type. *Front. Neural Circuits* **8**, 3 (2014).
  52. Lucas, E. K. & Clem, R. L. GABAergic interneurons: The orchestra or the conductor in

- fear learning and memory? *Brain Res. Bull.* **141**, 13–19 (2018).
53. Fu, Y., Lv, R., Jin, L., Lu, Q., Shao, X., He, J., Wu, L., Zhang, L. & Hu, H. Association of apolipoprotein E polymorphisms with temporal lobe epilepsy in a Chinese Han population. *Epilepsy Res.* **91**, 253–259 (2010).
  54. Li, Z., Ding, C., Gong, X., Wang, X. & Cui, T. Apolipoprotein E  $\epsilon 4$  Allele was Associated With Nonlesional Mesial Temporal Lobe Epilepsy in Han Chinese Population. *Medicine (Baltimore)*. **95**, e2894 (2016).
  55. Diaz-Arrastia, R., Gong, Y., Fair, S., Scott, K. D., Garcia, M. C., Carlile, M. C., Agostini, M. A. & Van Ness, P. C. Increased Risk of Late Posttraumatic Seizures Associated With Inheritance of APOE  $\epsilon 4$  Allele. *Arch. Neurol.* **60**, 818 (2003).
  56. Salzman, A., Perroud, N., Crespel, A., Lambercy, C. & Malafosse, A. Candidate genes for temporal lobe epilepsy: a replication study. *Neurol. Sci.* **29**, 397–403 (2008).
  57. Johnson, E. L., Krauss, G. L., Lee, A. K., Schneider, A. L. C., Dearborn, J. L., Kucharska-Newton, A. M., Huang, J., Alonso, A. & Gottesman, R. F. Association Between Midlife Risk Factors and Late-Onset Epilepsy: Results From the Atherosclerosis Risk in Communities Study. *JAMA Neurol.* **75**, 1375–1382 (2018).
  58. Briellmann, R. S., Torn-Broers, Y., Busuttill, B. E., Major, B. J., Kalnins, R. M., Olsen, M., Jackson, G. D., Frauman, A. G. & Berkovic, S. F. APOE epsilon4 genotype is associated with an earlier onset of chronic temporal lobe epilepsy. *Neurology* **55**, 435–7 (2000).
  59. Kauffman, M. A., Consalvo, D., Moron, D. G., Lereis, V. P. & Kochen, S. ApoE  $\epsilon 4$  genotype and the age at onset of temporal lobe epilepsy: A case–control study and meta-analysis. *Epilepsy Res.* **90**, 234–239 (2010).

60. Leal, B., Chaves, J., Carvalho, C., Bettencourt, A., Freitas, J., Lopes, J., Ramalheira, J., Costa, P. P., Mendonça, D., Silva, A. M. & Silva, B. M. Age of onset of mesial temporal lobe epilepsy with hippocampal sclerosis: the effect of apolipoprotein E and febrile seizures. *Int. J. Neurosci.* **127**, 800–804 (2017).
61. Aboud, O., Mrak, R. E., Boop, F. & Griffin, S. T. Apolipoprotein epsilon 3 alleles are associated with indicators of neuronal resilience. *BMC Med.* **10**, 35 (2012).
62. Sporis, D., Sertic, J., Henigsberg, N., Mahovic, D., Bogdanovic, N. & Babic, T. Association of refractory complex partial seizures with a polymorphism of ApoE genotype. *J. Cell. Mol. Med.* **9**, 698–703
63. Schubert, C. R., Carmichael, L. L., Murphy, C., Klein, B. E. K., Klein, R. & Cruickshanks, K. J. Olfaction and the 5-year incidence of cognitive impairment in an epidemiological study of older adults. *J. Am. Geriatr. Soc.* **56**, 1517–21 (2008).
64. Devanand, D. P., Liu, X., Tabert, M. H., Pradhaban, G., Cuasay, K., Bell, K., de Leon, M. J., Doty, R. L., Stern, Y. & Pelton, G. H. Combining early markers strongly predicts conversion from mild cognitive impairment to Alzheimer’s disease. *Biol. Psychiatry* **64**, 871–9 (2008).
65. Olofsson, J. K., Rönnlund, M., Nordin, S., Nyberg, L., Nilsson, L.-G. & Larsson, M. Odor Identification Deficit as a Predictor of Five-Year Global Cognitive Change: Interactive Effects with Age and ApoE-ε4. *Behav. Genet.* **39**, 496–503 (2009).
66. Olofsson, J. K., Josefsson, M., Ekström, I., Wilson, D., Nyberg, L., Nordin, S., Nordin Adolfsson, A., Adolfsson, R., Nilsson, L.-G. & Larsson, M. Long-term episodic memory decline is associated with olfactory deficits only in carriers of ApoE-ε4. *Neuropsychologia* **85**, 1–9 (2016).

67. Misiak, M. M., Hipolito, M. S., Ressom, H. W., Obisesan, T. O., Manaye, K. F. & Nwulia, E. A. Apo E4 Alleles and Impaired Olfaction as Predictors of Alzheimer's Disease. *Clin. Exp. Psychol.* **3**, (2017).
68. Hu, B., Geng, C. & Hou, X.-Y. Oligomeric amyloid- $\beta$  peptide disrupts olfactory information output by impairment of local inhibitory circuits in rat olfactory bulb. *Neurobiol. Aging* **51**, 113–121 (2017).
69. Peng, K. Y., Mathews, P. M., Levy, E. & Wilson, D. A. Apolipoprotein E4 causes early olfactory network abnormalities and short-term olfactory memory impairments. *Neuroscience* **343**, 364–371 (2017).
70. Holtman, I. R., Raj, D. D., Miller, J. A., Schaafsma, W., Yin, Z., Brouwer, N., Wes, P. D., Möller, T., Orre, M., Kamphuis, W., Hol, E. M., Boddeke, E. W. G. M. & Eggen, B. J. L. Induction of a common microglia gene expression signature by aging and neurodegenerative conditions : a co-expression meta-analysis. *Acta Neuropathol.* **May**, 1–18 (2015).
71. Frigerio, C. S., Wolfs, L., Fattorelli, N., Perry, V. H., Fiers, M., Strooper, B. De, Frigerio, C. S., Wolfs, L., Fattorelli, N., Thrupp, N., Voytyuk, I., Schmidt, I. & De Strooper, B. The Major Risk Factors for Alzheimer's Disease: Age, Sex, and Genes Modulate the Microglia Response to A $\beta$  Plaques. *Cell Rep.* **27**, 1293–1306 (2019).
72. Krasemann, S., Madore, C., Cialic, R., Baufeld, C., Calcagno, N., El Fatimy, R., Beckers, L., O'Loughlin, E., Xu, Y., Fanek, Z., Greco, D. J., Smith, S. T., Tweet, G., Humulock, Z., Zrzavy, T., Conde-Sanroman, P., Gacias, M., Weng, Z., Chen, H., Tjon, E., Mazaheri, F., Hartmann, K., Madi, A., Ulrich, J. D., Glatzel, M., Worthmann, A., Heeren, J., Budnik, B., Lemere, C., Ikezu, T., Heppner, F. L., Litvak, V., Holtzman, D. M., Lassmann, H.,

- Weiner, H. L., Ochando, J., Haass, C. & Butovsky, O. The TREM2-APOE Pathway Drives the Transcriptional Phenotype of Dysfunctional Microglia in Neurodegenerative Diseases. *Immunity* **47**, 566-581.e9 (2017).
73. Sarlus, H. & Heneka, M. T. Microglia in Alzheimer's disease. *J. Clin. Invest.* **127**, 3240–3249 (2017).
74. Hansen, D. V, Hanson, J. E. & Sheng, M. Microglia in Alzheimer's disease. *J. Cell Biol.* **217**, 459–472 (2017).
75. Chen, Z., Jalabi, W., Hu, W., Park, H., Gale, J. T., Kidd, G. J., Bernatowicz, R., Gossman, Z. C., Chen, J. T., Dutta, R. & Trapp, B. D. Microglial displacement of inhibitory synapses provides neuroprotection in the adult brain. *Nat. Commun.* **5**, 4486 (2014).
76. Roseti, C., Fucile, S., Lauro, C., Martinello, K., Bertollini, C., Esposito, V., Mascia, A., Catalano, M., Aronica, E. & Palma, E. Fractalkine/CX3CL1 modulates GABA(A) currents in human temporal lobe epilepsy. *Epilepsia* **5**, 1834–1844 (2013).
77. Brockner, G., Brauer, K., Hartg, W., Wolff, J. R., Rickma, M. J., Derouiche, A., Delpech, B., Girard, N., Oertel, W. H. & Reichenbach, A. Perineuronal Nets Provide a Polyanionic , Glia-Associated Form of Microenvironment Around Certain Neurons in Many Parts of the Rat Brain. *Glia* **8**, 183–200 (1993).
78. Kwok, J. C. F., Dick, G., Wang, D. & Fawcett, J. W. Extracellular Matrix and Perineuronal Nets in CNS Repair. *Dev. Neurobiol.* **7**, 1073–89 (2011).
79. Baig, S., Wilcock, G. K. & Love, S. Loss of perineuronal net N -acetylgalactosamine in Alzheimer's disease. *Acta Neuropathol.* **110**, 393–401 (2005).
80. Härtig, W., Brauer, K. & G, B. Wisteria floribunda agglutinin-labelled nets surround parvalbumin- containing neurons. *Neuroreport* **3**, 869–72 (1992).

81. Cattaud, V., Bezzina, C., Rey, C. C., Lejards, C., Dahan, L. & Verret, L. Early disruption of parvalbumin expression and perineuronal nets in the hippocampus of the Tg2576 mouse model of Alzheimer's disease can be rescued by enriched environment. *Neurobiol. Aging* **72**, 147–158 (2018).
82. Cabungcal, J., Steullet, P., Morishita, H., Kraftsik, R., Cuenod, M. & Hensch, T. K. Perineuronal nets protect fast-spiking interneurons against oxidative stress. *Proc. Natl. Acad. Sci.* **110**, 9130–9135 (2013).
83. Persson, J., Lind, J., Larsson, A., Ingvar, M., Slegers, K., Van Broeckhoven, C., Adolfsson, R., Nilsson, L.-G. & Nyberg, L. Altered deactivation in individuals with genetic risk for Alzheimer's disease. *Neuropsychologia* **46**, 1679–1687 (2008).
84. Fleisher, A. S., Sherzai, A., Taylor, C., Langbaum, J. B. S., Chen, K. & Buxton, R. B. Resting-state BOLD networks versus task-associated functional MRI for distinguishing Alzheimer's disease risk groups. *Neuroimage* **47**, 1678–1690 (2009).
85. Pihlajamäki, M. & Sperling, R. A. Functional MRI assessment of task-induced deactivation of the default mode network in Alzheimer's disease and at-risk older individuals. *Behav. Neurol.* **21**, 77–91 (2009).
86. Hu, Y., Chen, X., Gu, H. & Yang, Y. Resting-state glutamate and GABA concentrations predict task-induced deactivation in the default mode network. *J. Neurosci.* **33**, 18566–73 (2013).
87. Kapogiannis, D., Reiter, D. A., Willette, A. A. & Mattson, M. P. Posteromedial cortex glutamate and GABA predict intrinsic functional connectivity of the default mode network. *Neuroimage* **64**, 112–119 (2013).
88. Chen, X., Fan, X., Hu, Y., Zuo, C., Whitfield-Gabrieli, S., Holt, D., Gong, Q., Yang, Y.,

- Pizzagalli, D. A., Du, F. & Ongur, D. Regional GABA Concentrations Modulate Inter-network Resting-state Functional Connectivity. *Cereb. Cortex* (2018).  
doi:10.1093/cercor/bhy059
89. Buckner, R. L., Andrews-Hanna, J. R. & Schacter, D. L. The brain's default network: anatomy, function, and relevance to disease. *Ann. N. Y. Acad. Sci.* **1124**, 1–38 (2008).
  90. Mevel, K., Chételat, G., Eustache, F. & Desgranges, B. The default mode network in healthy aging and Alzheimer's disease. *Int. J. Alzheimers. Dis.* **2011**, 535816 (2011).
  91. Lustig, C., Snyder, A. Z., Bhakta, M., O'Brien, K. C., McAvoy, M., Raichle, M. E., Morris, J. C. & Buckner, R. L. Functional deactivations: change with age and dementia of the Alzheimer type. *Proc. Natl. Acad. Sci. U. S. A.* **100**, 14504–9 (2003).
  92. Broyd, S. J., Demanuele, C., Debener, S., Helps, S. K., James, C. J. & Sonuga-Barke, E. J. S. Default-mode brain dysfunction in mental disorders: A systematic review. *Neurosci. Biobehav. Rev.* **33**, 279–296 (2009).
  93. Dickerson, B. C., Salat, D. H., Greve, D. N., Chua, E. F., Rand-Giovannetti, E., Rentz, D. M., Bertram, L., Mullin, K., Tanzi, R. E., Blacker, D., Albert, M. S., Sperling, R. A., Tangalos, E. G. & Jack, C. R. Increased hippocampal activation in mild cognitive impairment compared to normal aging and AD. *Neurology* **65**, 404–11 (2005).
  94. Bondi, M. W., Houston, W. S., Eyler, L. T. & Brown, G. G. fMRI evidence of compensatory mechanisms in older adults at genetic risk for Alzheimer disease. *Neurology* **64**, 501–508 (2005).
  95. Nuriel, T., Angulo, S. L., Khan, U., Ashok, A., Chen, Q., Figueroa, H. Y., Emrani, S., Liu, L., Herman, M., Barrett, G., Savage, V., Buitrago, L., Cepeda-Prado, E., Fung, C., Goldberg, E., Gross, S. S., Hussaini, S. A., Moreno, H., Small, S. A. & Duff, K. E.

- Neuronal hyperactivity due to loss of inhibitory tone in APOE4 mice lacking Alzheimer's disease-like pathology. *Nat. Commun.* **8**, 1464 (2017).
96. Bakker, A., Albert, M. S., Krauss, G., Speck, C. L. & Gallagher, M. Response of the medial temporal lobe network in amnesic mild cognitive impairment to therapeutic intervention assessed by fMRI and memory task performance. *NeuroImage Clin.* **7**, 688–698 (2015).
97. Yassa, M. A., Lacy, J. W., Stark, S. M., Albert, M. S., Gallagher, M. & Stark, C. E. L. Pattern separation deficits associated with increased hippocampal CA3 and dentate gyrus activity in nondemented older adults. *Hippocampus* **21**, n/a-n/a (2010).
98. Miller, S. L., Fenstermacher, E., Bates, J., Blacker, D., Sperling, R. A. & Dickerson, B. C. Hippocampal activation in adults with mild cognitive impairment predicts subsequent cognitive decline. *J. Neurol. Neurosurg. Psychiatry* **79**, 630–5 (2008).
99. Leal, S. L., Landau, S. M., Bell, R. K. & Jagust, W. J. Hippocampal activation is associated with longitudinal amyloid accumulation and cognitive decline. *Elife* **6**, e22978 (2017).
100. Filippini, N., MacIntosh, B. J., Hough, M. G., Goodwin, G. M., Frisoni, G. B., Smith, S. M., Matthews, P. M., Beckmann, C. F. & Mackay, C. E. Distinct patterns of brain activity in young carriers of the APOE- $\epsilon$ 4 allele. *Proc. Natl. Acad. Sci. U. S. A.* **106**, 7209–7214 (2009).
101. Bookheimer, S. Y., Strojwas, M. H., Cohen, M. S., Saunders, A. M., Pericak-Vance, M. A., Mazziotta, J. C. & Small, G. W. Patterns of Brain Activation in People at Risk for Alzheimer's Disease. *N. Engl. J. Med.* **343**, 450–456 (2000).
102. Dennis, N. A., Browndyke, J. N., Stokes, J., Need, A., Burke, J. R., Welsh-Bohmer, K. A.



- & Cabeza, R. Temporal lobe functional activity and connectivity in young adult APOE  $\epsilon$ 4 carriers. *Alzheimer's Dement.* **6**, 303–311 (2010).
103. Gillespie, A. K., Jones, E. A., Lin, Y.-H., Karlsson, M. P., Kay, K., Yoon, S. Y., Tong, L. M., Nova, P., Carr, J. S., Frank, L. M. & Huang, Y. Apolipoprotein E4 causes age-dependent disruption of slow gamma oscillations during hippocampal sharp-wave ripples. *Neuron* **90**, 740–751 (2016).
104. Buzsáki, G. Hippocampal sharp wave-ripple: A cognitive biomarker for episodic memory and planning. *Hippocampus* **1188**, 1073–1188 (2015).
105. Carr, M. F., Karlsson, M. P. & Frank, L. M. Transient Slow Gamma Synchrony Underlies Hippocampal Memory Replay. *Neuron* **75**, 700–713 (2012).
106. Wang, C., Najm, R., Xu, Q., Jeong, D., Walker, D., Balestra, M. E., Yoon, S. Y., Yuan, H., Li, G., Miller, Z. A., Miller, B. L. & Malloy, M. J. Gain of Toxic Apolipoprotein E4 Effects in Human iPSC-derived Neurons is Ameliorated by a Small-Molecule Structure Corrector. *Nat. Med.* 1–11 (2018). doi:10.1038/s41591-018-0004-z
107. Kondo, T., Asai, M., Tsukita, K., Kutoku, Y., Ohsawa, Y., Sunada, Y., Imamura, K., Egawa, N., Yahata, N., Okita, K., Takahashi, K., Asaka, I., Aoi, T., Watanabe, A., Watanabe, K., Kadoya, C., Nakano, R., Watanabe, D., Maruyama, K., Hori, O., Hibino, S., Choshi, T., Nakahata, T., Hioki, H., Kaneko, T., Naitoh, M., Yoshikawa, K., Yamawaki, S., Suzuki, S., Hata, R., Ueno, S.-I., Seki, T., Kobayashi, K., Toda, T., Murakami, K., Irie, K., Klein, W. L., Mori, H., Asada, T., Takahashi, R., Iwata, N., Yamanaka, S. & Inoue, H. Modeling Alzheimer's disease with iPSCs reveals stress phenotypes associated with intracellular A $\beta$  and differential drug responsiveness. *Cell Stem Cell* **12**, 487–96 (2013).

108. Kondo, T., Imamura, K., Funayama, M., Tsukita, K., Miyake, M., Ohta, A., Woltjen, K., Nakagawa, M., Asada, T., Arai, T., Kawakatsu, S., Izumi, Y., Kaji, R., Iwata, N. & Inoue, H. iPSC-Based Compound Screening and In Vitro Trials Identify a Synergistic Anti-amyloid  $\beta$  Combination for Alzheimer's Disease. *Cell Rep.* **21**, 2304–2312 (2017).
109. Tong, L. M., Yoon, S. Y., Andrews-Zwilling, Y., Yang, A., Lin, V., Lei, H. & Huang, Y. Enhancing GABA Signaling during Middle Adulthood Prevents Age-Dependent GABAergic Interneuron Decline and Learning and Memory Deficits in ApoE4 Mice. *J. Neurosci.* **36**, 2316–22 (2016).
110. Li, Y., Sun, H., Chen, Z., Xu, H., Bu, G. & Zheng, H. Implications of GABAergic Neurotransmission in Alzheimer's Disease. *Front. Aging Neurosci.* **8**, 31 (2016).
111. Nava-Mesa, M. O., Jimenez-Díaz, L., Yajeya, J. & Navarro-Lopez, J. D. GABAergic neurotransmission and new strategies of neuromodulation to compensate synaptic dysfunction in early stages of Alzheimer's disease. *Front. Cell. Neurosci.* **8**, 167 (2014).
112. Calvo-Flores Guzmán, B., Vinnakota, C., Govindpani, K., Waldvogel, H. J., Faull, R. L. M. & Kwakowsky, A. The GABAergic system as a therapeutic target for Alzheimer's disease. *J. Neurochem.* **146**, 649–669 (2018).
113. Helmstaedter, C. & Witt, J.-A. Cognitive outcome of antiepileptic treatment with levetiracetam versus carbamazepine monotherapy: A non-interventional surveillance trial. *Epilepsy Behav.* **18**, 74–80 (2010).
114. Lippa, C. F., Rosso, A., Hepler, M., Jenssen, S., Pillai, J. & Irwin, D. Levetiracetam: A Practical Option for Seizure Management in Elderly Patients With Cognitive Impairment. *Am. J. Alzheimer's Dis. Other Dementias* **25**, 149–154 (2010).

115. Cumbo, E. & Ligori, L. D. Levetiracetam, lamotrigine, and phenobarbital in patients with epileptic seizures and Alzheimer's disease. *Epilepsy Behav.* **17**, 461–466 (2010).
116. Vidal-Piñeiro, D., Martín-Trias, P., Falcón, C., Bargalló, N., Clemente, I. C., Valls-Solé, J., Junqué, C., Pascual-Leone, A. & Bartrés-Faz, D. Neurochemical Modulation in Posteromedial Default-mode Network Cortex Induced by Transcranial Magnetic Stimulation. *Brain Stimul.* **8**, 937–944 (2015).
117. Cardin, J. A., Carlén, M., Meletis, K., Knoblich, U., Zhang, F., Deisseroth, K., Tsai, L.-H. & Moore, C. I. Driving fast-spiking cells induces gamma rhythm and controls sensory responses. *Nature* **459**, 663–667 (2009).
118. Sohal, V. S., Zhang, F., Yizhar, O. & Deisseroth, K. Parvalbumin neurons and gamma rhythms enhance cortical circuit performance. *Nature* **459**, 698–702 (2009).
119. Ketz, N., Jones, A. P., Bryant, N. B., Clark, V. P. & Pilly, P. K. Closed-Loop Slow-Wave tACS Improves Sleep-Dependent Long-Term Memory Generalization by Modulating Endogenous Oscillations. *J. Neurosci.* **38**, 7314–7326 (2018).
120. Iaccarino, H. F., Singer, A. C., Martorell, A. J., Rudenko, A., Gao, F., Gillingham, T. Z., Mathys, H., Seo, J., Kritskiy, O., Abdurrob, F., Adaikkan, C., Canter, R. G., Rueda, R., Brown, E. N., Boyden, E. S. & Tsai, L.-H. Gamma frequency entrainment attenuates amyloid load and modifies microglia. *Nature* **540**, 230–235 (2016).
121. Martorell, A. J., Paulson, A. L., Suk, H., Boyden, E. S., Singer, A. C. & Tsai, L. Multi-sensory Gamma Stimulation Ameliorates Alzheimer's-Associated Pathology and Improves Cognition. *Cell* **177**, 256-271.e22 (2019).
122. Li, K.-X., Lu, Y.-M., Xu, Z.-H., Zhang, J., Zhu, J.-M., Zhang, J.-M., Cao, S.-X., Chen, X.-J., Chen, Z., Luo, J.-H., Duan, S. & Li, X.-M. Neuregulin 1 regulates excitability of fast-

- spiking neurons through Kv1.1 and acts in epilepsy. *Nat. Neurosci.* **15**, 267–273 (2012).
123. Marissal, T., Salazar, R. F., Bertollini, C., Mutel, S., De Roo, M., Rodriguez, I., Müller, D. & Carleton, A. Restoring wild-type-like CA1 network dynamics and behavior during adulthood in a mouse model of schizophrenia. *Nat. Neurosci.* **21**, 1412–1420 (2018).
124. Srivastava, D. & DeWitt, N. In Vivo Cellular Reprogramming: The Next Generation. *Cell* **166**, 1386–1396 (2016).
125. Tyson, J. A. & Anderson, S. A. GABAergic interneuron transplants to study development and treat disease. *Trends Neurosci.* **37**, 169–177 (2014).
126. Steinbeck, J. A. & Studer, L. Moving stem cells to the clinic: Potential and limitations for brain repair. *Neuron* **86**, 187–206 (2015).
127. Li, X., Zhu, H., Sun, X., Zuo, F., Lei, J., Wang, Z., Bao, X. & Wang, R. Human Neural Stem Cell Transplantation Rescues Cognitive Defects in APP/PS1 Model of Alzheimer's Disease by Enhancing Neuronal Connectivity and Metabolic Activity. *Front. Aging Neurosci.* **8**, 282 (2016).
128. Cunningham, M., Cho, J.-H., Leung, A., Savvidis, G., Ahn, S., Moon, M., Lee, P. K. J., Han, J. J., Azimi, N., Kim, K.-S., Bolshakov, V. Y. & Chung, S. hPSC-Derived Maturing GABAergic Interneurons Ameliorate Seizures and Abnormal Behavior in Epileptic Mice. *Cell Stem Cell* **15**, 559–573 (2014).
129. Martinez-Losa, M., Tracy, T. E., Ma, K., Verret, L., Clemente-Perez, A., Khan, A. S., Cobos, I., Ho, K., Gan, L., Mucke, L., Alvarez-Dolado, M. & Palop, J. J. Nav1.1-Overexpressing Interneuron Transplants Restore Brain Rhythms and Cognition in a Mouse Model of Alzheimer's Disease. *Neuron* **98**, 75-89.e5 (2018).

## **CHAPTER II**

### **Early Hippocampal Sharp-Wave Ripple Deficits Predict Later Learning and Memory Impairments in an Alzheimer's Disease Mouse Model**

## **Abstract**

Alzheimer's disease (AD) is characterized by progressive memory loss, and there is a pressing need to identify early pathophysiological alterations that predict subsequent memory impairment. Hippocampal sharp-wave ripples (SWRs) – electrophysiological signatures of memory reactivation in the hippocampus – are a compelling candidate for doing so. Mouse models of AD show reductions in both SWR abundance and associated slow gamma (SG) power during aging, but these alterations have yet to be directly linked to memory impairments. In aged apolipoprotein E4 knock in (apoE4-KI) mice – a model of the major genetic risk factor for AD – we found that reduced SWR abundance and associated CA3 SG power predicted spatial memory impairments measured 1–2 months later. Importantly, SWR-associated CA3 SG power reduction in young apoE4-KI mice also predicted spatial memory deficits measured 10 months later. These results establish features of SWRs as potential functional biomarkers of memory impairment in AD.

## Introduction

Alzheimer's disease (AD) is a form of dementia characterized by progressive cognitive decline that affects 11% of the US population over the age of 65<sup>1</sup>. The continued failure of AD clinical trials has redirected the field towards halting disease progression before symptoms manifest; once memory impairment is detected, it may be too late for treatment to reverse it<sup>2</sup>. While there are known genetic and environmental risk factors for AD<sup>3</sup>, our ability to predict which individuals will develop the disease, when symptoms will arise, and how rapidly they will progress remains poor. There is therefore a pressing need to identify early pathophysiological alterations which can distinguish later cognitive decline from healthy aging.

To identify early, predictive alterations, we studied a mouse model of  $\epsilon 4$  variant of the *APOE* gene, the most common genetic risk factor for AD<sup>4,5</sup>. It has an allelic frequency of 20–25%, yet is found in 65–80% of AD patients<sup>6</sup>. The presence of  $\epsilon 4$  alleles increases the likelihood of developing AD by age 85 from 10% to 70% in a gene dose-dependent manner<sup>7</sup>, but does not guarantee AD. Thus, the population of  $\epsilon 4$  carriers shows significant individual variation, and predicting that variation could allow preventative treatment to be targeted to the highest risk individuals. Mice with human *APOE*  $\epsilon 4$  knocked in at the mouse *APOE* locus (apoE4-KI) have physiologically appropriate patterns and levels of apoE expression<sup>8,9</sup> and recapitulate gender and age effects of apoE4 seen in humans<sup>6,10–12</sup>. By 16 months of age, female apoE4-KI mice show spatial learning and memory deficits as measured in the Morris water maze (MWM), recapitulating age-dependent memory loss as seen in human  $\epsilon 4$  carriers<sup>13</sup> and providing a useful animal model for longitudinal study of memory decline.

A memory-predicting alteration should reflect underlying pathology of AD and be related directly to memory processes. The hippocampus is one of the first sites of AD pathology and is required for the spatial learning and memory processes that falter early in AD<sup>14-17</sup>; thus, physiological signatures of hippocampal information processing could provide useful biomarkers. The hippocampal local field potential (LFP) is a particularly appealing candidate. The LFP is an extracellular voltage measurement that reflects the summation of activity patterns from local neurons. The LFP provides real-time measures related to memory processing including consolidation and retrieval<sup>18</sup> and can be repeatedly measured in the same subject; for these reasons, features of the LFP have been previously proposed as potential biomarkers in AD<sup>19,20</sup>. We focused on sharp-wave ripples (SWRs), an LFP signature of memory replay. During SWRs, a large population of hippocampal neurons is activated, often in sequences that recapitulate past or potential future experiences<sup>18</sup>. SWRs are critical for memory consolidation and retrieval<sup>21,22</sup>, as their disruption impairs spatial learning and memory<sup>23-26</sup>. SWRs are also signatures of a brain-wide activity patterns<sup>27</sup>, and could in principle be detected via EEG or other non-invasive approaches.

We further narrowed our focus to two SWR features that are altered in AD models – SWR abundance and associated slow gamma (SG) power. SWR abundance (events/s) is reduced in apoE4-KI mice<sup>28</sup> and in models of tau and amyloid  $\beta$  overexpression<sup>29,30</sup>. SWR abundance increases during and after both novel and rewarded experiences<sup>31-33</sup>, suggesting a relationship between SWR abundance and the need to store memories. SWR-associated SG power is reduced in both apoE4-KI mice<sup>28</sup> and in models of amyloid  $\beta$  overexpression<sup>34</sup>. During SWRs, power in the SG band (30–50 Hz) increases throughout the hippocampus<sup>28,35-37</sup>. SWR-associated SG properties have been linked to the quality of memory replay and may help coordinate its



structure<sup>36,38</sup>. These observations raise the possibility that SWR abundance and associated SG power could serve as functional biomarkers, but the potential relationship between SWR properties and memory impairments in AD models has yet to be explored. We also know little about the stability of these properties over an animal's lifetime and about whether SWR properties in early life could predict cognitive abilities in later life.

We set out to determine whether early deficits in SWR features could be used to predict age-dependent cognitive decline in an AD mouse model. We recorded hippocampal network activity from apoE3-KI and apoE4-KI mice at rest, then later examined performance on the Morris water maze (MWM)<sup>39</sup>, a spatial goal approach task, and active place avoidance (APA)<sup>40</sup>, a spatial goal avoidance task. We found that deficits in SWR abundance and associated SG power in CA3 predicted spatial memory impairment on both tasks in aged apoE4-KI mice. Strikingly, SWR-associated CA3 SG power remained relatively stable over time, and SG power reduction in young apoE4-KI mice predicted spatial memory deficits 10 months later. These findings support the use of SWR properties as functional biomarkers in AD.

## Materials and Methods

### EXPERIMENTAL MODEL AND SUBJECT DETAILS

Mice with human apoE3 or apoE4 knocked-in at the mouse *APOE* locus on a C57BL/6 background<sup>41</sup> were originally obtained from Taconic. All animals were bred in-house using trio breeding producing 10 pups per litter on average, which were weaned at 28 days. Female mice aged 5–20 months were used. Animals were housed in a pathogen-free barrier facility on a 12h light cycle (lights on at 7am and off at 7pm) at 19–23°C and 30–70% humidity. Animals were identified by ear punch under brief isofluorane anesthesia and genotyped by PCR of a tail clipping at both weaning and perfusion. All animals otherwise received no procedures except those reported in this study. Throughout the study, mice were singly housed. All animal experiments were conducted in accordance with the guidelines and regulations of the National Institutes of Health, the University of California, and the Gladstone Institutes under IACUC protocol AN117112.

### METHOD DETAILS

The study consisted of two cohorts of female apoE3-KI and apoE4-KI mice: one screen cohort which had electrophysiological recordings at 12–18 months and MWM at 13–19 months and one replication cohort which had electrophysiological recordings at 5–8 months, 9–11 months, and 13–17 months, MWM at 5-8 months, open field, elevated plus maze, and MWM at 14–18 months, and APA and hot plate at 15–20 months (see **Fig. 1A**). Electrode lifetime did not diminish our ability to detect SWRs and measure associated SG power, as neither metric declined over aging (**Fig. 2.8A** and **2.8B**). Some mice in the replication cohort did not survive the duration of the longitudinal study, so their electrophysiological data was included in younger group analyses, but their behavioral data was not available for group analyses or correlations (**Table S1**). For this reason,

additional mice which had not had any LFP recordings were included in the aged behavioral studies of the replication cohort to achieve sufficient power for group analyses (**Table S1**). All procedures were conducted during the light cycle. Mice were recorded at a randomly allocated time each day to counteract differences caused by circadian effects. The experimenters were blinded to genotype during surgery, recordings, behavior, and histology.

## **Surgery**

Mice were anesthetized by intraperitoneal injection of ketamine (60 mg/kg) and xylazine (30 mg/kg); anesthesia was maintained with 0.6–1.5% isoflurane given through a vaporizer and nose cone. The head was secured with earbars and a tooth bar in a stereotaxic alignment system (Kopf Instruments). Fur was removed from the scalp, which was then sterilized with alternating swabs of chlorhexidine and 70% ethanol. The scalp was opened, sterilized with 3% hydrogen peroxide, and thoroughly cleaned to reduce risk of tissue regrowth. 0.5 mm craniotomies were made over the right frontal cortex and left parietal cortex. Skull screws (FST) were inserted to anchor and support the implant, and were secured with dental adhesive (C&B Metabond, Parkell). An additional 0.5 mm craniotomy was made over the right cerebellum for insertion of the indifferent ground and reference wires. A fourth craniotomy was centered at -1.95 mm AP and 1.5 mm ML from bregma and extended bidirectionally along the ML axis to 2 mm width to receive the recording probe. The probes had four 5 mm shanks spaced 400  $\mu$ m apart with 8 electrode sites per shank and 200  $\mu$ m spacing between sites (Neuronexus; configuration A4x8-400-200-704-CM32). The probe was quickly lowered until the tip reached 2.2 mm below the surface of the brain, and the reference and ground wire was inserted into the subdural space above the cerebellum. The probe was cemented in place with dental acrylic and the scalp was closed with nylon sutures. Mice

were treated with 0.0375 mg/kg buprenorphine intraperitoneally and 5 mg/kg ketofen subcutaneously 30–45 min after surgery, monitored until ambulatory, then monitored daily for 3 days. A minimum of 1 week was allowed for recovery before recording.

### **Electrophysiology**

Data from all mice was collected, amplified, multiplexed, processed, and digitized with 32-channel Upright Headstage, commutator, and Main Control Unit (SpikeGadgets). Simultaneous data acquisition at 30 kHz and video tracking at 30 frames/s was performed using Trodes software (SpikeGadgets). Each data collection time point consisted of 5 days of 60 min home cage sessions. Each mouse was recorded at a randomly assigned time each day across the light cycle to control for the effects of circadian rhythm. During recordings, home cages were changed to Alpha-dri bedding (Shepherd Specialty Papers) to enable video tracking.

### **Behavior**

During the MWM task, mice were housed in the testing room with the arena obscured by a partition and given 2 days to acclimate to the room in a fresh cage before training began. In all trials, mice were placed in a 122 cm diameter pool filled with opaque water and had to locate a 14 x 14 cm platform submerged 1.5 cm below the water's surface. Mice could only use spatial cues on the walls around the pool to guide their search. On once daily pretraining trial for the first 2 days, mice swam down a rectangular channel until they locate the platform, or were guided there by the experimenter after 90 s. Then, the rectangular guides were removed and the platform was placed in a new location. On 4 daily trials for the next 5 hidden days, mice were dropped at random locations each trial and given 60 s to locate the platform. Daily trials were divided into two pairs

10 min apart, with 4 hours between the pairs. Then, on probe trials conducted 24 hours, 72 hours, and 128 hours after the last hidden day, the platform was removed, and mice explored the arena for 60 s. Finally, on twice daily visible trials over 3 days, a flag was placed on the platform, and mice swam directly to the platform to measure visual acuity. Video tracking at 30 frames/s was performed during all trials with Ethovision (Noldus).

During the APA task, mice were housed adjacent to the testing room and given 3 days to acclimate to the room in a fresh cage before training began. In all trials, mice were placed in a 40 cm diameter arena that rotates at 1 rpm (BioSignal Group). On the first day, mice habituated to the environment by exploring it for 10 minutes. On the following 4 days, when mice entered a 60° region which is fixed relative to the room, as measured by video tracking, they received a 0.2 mA foot shock for 500 ms at 60 Hz every 1.5 s until they left the shock zone. Mice could only use spatial cues on the walls around the arena to actively avoid this shock zone given the constant rotation of the arena. On the fifth day, the shock was inactivated for the first 5 min (probe), then turned on for the second 5 min (reinstatement) of a 10 min continuous trial. 1 apoE4-KI mouse was excluded from APA and hot plate testing due to a motor impairment it developed immediately prior to testing (see **Table 2.1**). Shock times and video tracking at 30 frames/s relative to the rotating arena were recorded during all trials with Tracker software (BioSignal Group).

We selected five metrics to assess different aspects of spatial learning and memory on the APA task, four of which were proposed by the original task creators<sup>40</sup>. Over a trial, mice attempt to enter the shock zone as few times as possible (entrances). Mice are successful if they move around in the arena to avoid the shock zone (path length) rather than staying still and then fleeing when shocked, optimally spending most of the trial as far from the shock zone as possible (percent time in quadrant opposite target). Mice with more accurate representations of the shock zone

boundary may not move far from the shock zone during each bout of movement (distance from shock zone per bout). At trial start, mice avoid the shock zone before being given any feedback as to its location (latency to first entrance).

Three tasks were used to assess general anxiety, exploratory drive, and nociception in order to determine if these factors affected spatial memory task acquisition. For these tests, mice were habituated to the testing room for 1 hour prior to testing. First, during the open field test, mice explore a 41 cm x 41 cm enclosed arena (San Diego Instruments). Location and movements are captured by beam breaks and analyzed in Photobeam Activity System software (San Diego Instruments). Reduced time spent or distance travelled in center of the field indicates anxiety, and reduced total distance travelled indicates reduced exploratory drive. Second, during the elevated plus maze, mice explore a plus-shaped maze 80 cm above the ground, 5 cm in width and 75 cm in length, consisting of 2 open arms without walls and 2 closed arms with 17 cm walls (Kinder Scientific). Location is captured by beam breaks and analyzed in MotorMonitor software (Kinder Scientific). Reduced time spent or distance travelled in open arm indicates anxiety, and reduced total distance travelled indicates reduced exploratory drive. Third, during the hot plate test, mice are placed on a 52°C plate in an open cylinder (Campden Instruments). Latency to hindpaw withdrawal is recorded via live observation by the experimenter, with high latency suggesting impaired nociception.

## **Histology**

Mice were deeply anesthetized with avertin, and a 30  $\mu$ A current was passed through each recording site for 2 s to generate small electrolytic lesions (Ugo Basile). Mice were then perfused with 0.9% NaCl. The brains were removed and stored at 4°C, then fixed in 4% PFA for 2 days,

rinsed in PBS for 1 day, and cryoprotected in 30% sucrose for at least 2 days. Hemibrains were cut into 30  $\mu\text{m}$  coronal sections with a microtome (Leica) and stored in cryoprotectant at  $-20^{\circ}\text{C}$ . Every third right hemibrain section was stained with cresyl violet, then electrolytic lesion locations were observed under a light microscope (Leica). Mice were excluded from electrophysiological analysis if they did not contain at least 2 electrode sites in CA1 pyramidal layer and from CA3 SG power analyses if they had no electrode sites in CA3 (**Table 2.1**).

### **Analysis of neural data**

Neural data was analyzed with custom software written in MATLAB (Mathworks) with the Chronux toolbox ([chronux.org](http://chronux.org)), NeuroQuery (Mattias Karlsson), and Trodes to MATLAB software (SpikeGadgets). The anatomical location of each electrode site was determined by examining Nissl-stained histological sections, raw LFP traces, the SWR-triggered spectrogram signature, and dentate spikes. Data were band-pass Butterworth filtered at 0.1–300 Hz, then downsampled to 1000 Hz and analyzed as LFP. Raw LFP data were band-pass equiripple filtered at 150–250 Hz for SWRs and at 30–50 Hz for SG. SWRs were detected on the CA1 site closest to the center of the pyramidal layer and defined by the envelope of the ripple-filtered trace exceeding 5 SD above baseline for at least 15 ms<sup>31</sup>. This method enables SWR detection that is robust to small differences in electrode location within the pyramidal layer between animals. Analysis of SWRs was restricted to periods of extended immobility, after the mouse Gaussian smoothed velocity had been  $< 1$  cm/s for 30 seconds or more. A recording session was excluded if the mouse was immobile for less than 10 min out of the 60 min session (1/65 and 3/85 sessions for apoE3-KI and apoE4-KI in the screen cohort; 9/65 and 2/80 sessions for apoE3-KI and apoE4-KI 5–8 month recording of the replication cohort). SWR-triggered spectrograms for each electrode site were

calculated across all SWRs with the multitaper method, as previously described<sup>36</sup>, with a 100 ms sliding window. For illustration in **Fig.s**, a 10 ms sliding window was used (see **Fig. 1C**). SWR-associated SG power was calculated as the averaged z-scored power over the 30–50 Hz frequency band 0–100 ms after ripple detection. This was then averaged over all SWR events and over all electrode sites within that cell layer or subregion. SG power was analyzed for three regions: CA1 stratum radiatum, CA3 including stratum pyramidale and stratum radiatum, and dentate gyrus including hilus and granule cell layers. Only dentate gyrus sites with visually confirmed dentate spikes were included in analysis. For multi-unit analysis, data were referenced to a corpus callosum electrode, band-pass Butterworth filtered at 600–6000 Hz, and then events greater than 75  $\mu$ V were analyzed as spikes. Sites used for SWR detection were further verified to be in the CA1 pyramidal layer by measuring large increases in multi-unit activity during SWRs. All measurements were analyzed per session, then averaged across all sessions to control for any effects of estrous cycling. Thus, each mouse contributed a single number to all comparisons.

### **Analysis of behavioral data**

For the screen cohort, we tested, for all hidden days, escape latency, slope of escape latency from day 1 to each day, and difference between escape latency on the last session of a day and the first session of the next day, and for probe days, percent time in target quadrant, number of target crossings, and area under the distance to platform curve. For the MWM task, escape latency during hidden trials and target crossings, percent time in target quadrant, and distance to platform location curve during probe trials were extracted from Noldus (Ethovision). Escape latency was averaged across the 4 daily trials to create 1 value per day. The following two analyses were not provided by Noldus and so were calculated in Excel (Microsoft). Escape latency slope was calculated as the



slope of the first-degree polynomial which best fit the average daily escape latencies across a range of hidden days. Area under the distance to platform curve was calculated with the trapezoid method. For the APA task, number of entrances into the shock zone, latency to first entrance to the shock zone, path length relative to the arena, and percent time spent in target opposite the shock zone for each day, plus the number of shocks that would have been received per entrance if the shock were active during the probe trial (pseudoshocks/entrance), were extracted from Tracker software (BioSignal Group). Distance travelled relative to the shock zone per movement bout was extracted using custom Python scripts that analyzed video tracking data extracted from Tracker software (BioSignal Group). When data was non-parametric, they were aligned rank transformed using ARTool (University of Washington).

## **QUANTIFICATION AND STATISTICAL ANALYSIS**

Performance scores were calculated by taking the z-score of each behavioral measure, inverting the sign of all behavioral measures where higher values indicate worse performance, and averaging across all behavioral measures. For the learning performance score for MWM, all behavioral measures that were significantly correlated with SWR abundance in the screen cohort were used: slope of the escape latency curve across days 1–2 and 1–3, escape latency on day 3, and overnight change in escape latency over days 1–2. For the learning performance score for APA, all behavioral measures that were significantly correlated with SWR abundance in the replication cohort were used: latency to first entrance, path length, and percent time in quadrant opposite the shock zone on day 2. For the memory precision performance score for MWM, all behavioral measures that were significantly correlated with CA3 SG power during SWRs in the screen cohort were used: percent time in target quadrant on probes 1 and 2, number of target crossings on probe

1, and area under the distance to platform curve on probes 1 and 2. For the memory precision performance score for APA, all behavioral measures that were significantly correlated with CA3 SG power during SWRs in the replication cohort were used: number of entrances into the shock zone on day 2 and distance travelled relative to shock zone per movement bout on days 2 and 3.

Statistics were computed using Prism software (Graphpad). Statistical test used, exact n, test statistic values, degrees of freedom, and exact p value are in **Fig.** legends. When a central value is plotted, it is always mean  $\pm$  SEM, as indicated in **Fig.** legends. In all cases, n represents number of animals. Significance was established as  $p < 0.05$ . No data were excluded based on statistical tests. Subjects were not randomized or stratified. Sample sizes were based on previous studies<sup>11,28</sup>. Most data were normally distributed as shown by Shapiro-Wilk test, and variances between groups were similar as shown by F test. In these instances, we used two-tailed paired and unpaired t tests, two-way ANOVA, two-way mixed-effects analysis (for data sets with missing values), and Pearson correlations. Post-hoc testing was done with Sidak correction for multiple comparisons. When these assumptions were violated, we used two-tailed Mann-Whitney U tests, two-way ANOVA or mixed-effects analysis on aligned rank transformed data<sup>42</sup>, and Spearman correlations. For the replication cohort, p values were adjusted using Holm-Sidak correction. All significant correlations reported in this paper were confirmed to be not driven by a single data point by measuring the significance of each relationship after removing each data point in a custom MATLAB script (Mathworks) and confirming  $p < 0.05$ .

## Results

Our study employed a two-stage design. We began with a cohort of animals where we searched for potential predictive relationships between SWR features and behavioral performance in older animals (screen cohort; **Fig. 2.1A** and **Table 2.1**). We then carried out a longitudinal study in a second cohort of animals to determine whether these relationships replicated and whether they were predictive over a substantial fraction of the lifespan (replication cohort; **Fig. 2.1A** and **Table 2.1**).

### **Aged apoE4-KI mice show SWR deficits and spatial approach task impairments and variability**

We first set out to confirm that aged apoE4-KI mice had deficits in SWR features – allowing the use of SWRs as a predictor – and had sufficient individual variation in memory impairment – enabling prediction of this phenotype. We recorded hippocampal network activity in female apoE3-KI mice and apoE4-KI mice at 12–18 months of age, and then assessed spatial learning and memory on the MWM task one month later (screen cohort; **Fig. 2.1A**). Recordings were taken from chronically implanted 32-channel silicon arrays targeting right dorsal hippocampus with sites distributed across CA1, CA3, and DG subregions (**Fig. 2.1B**). Data were collected over five daily 60 min recording sessions in the home cage. SWRs were detected in CA1 stratum pyramidale, and we verified that coincident with these SWRs was an increase in SG power throughout all three subregions of the hippocampus (**Fig. 2.1C** and **2.1D**)<sup>28</sup>. We also observed an increase in multi-unit activity in CA1 stratum pyramidale (**Fig. 2.3A**) during SWRs, and this firing rate was not different between genotypes during or immediately before SWR events. One month later, we measured the ability of each mouse to learn the location of a hidden platform in the MWM across

4 daily 1 min trials for 5 days and to remember the previous platform location during 3 probe trials with the platform removed, assessed 24 hours, 72 hours, and 128 hours (probes 1, 2, and 3) after the last hidden platform trial. Replicating previous findings<sup>11,28</sup>, apoE4-KI mice had reduced SWR abundance and associated SG power in CA1, CA3, and DG (**Fig. 2.1E** and **2.1F**) as well as impaired MWM learning (**Fig. 2.1G**). Critically, we observed substantial variability in task performance within the apoE4-KI population (**Fig. 2.1H**) indicating that, just as in human  $\epsilon 4$  carriers, genotype is insufficient to explain the extent of cognitive impairment. We capitalized on this variability to explore whether memory impairments could be predicted by deficits in SWR properties.

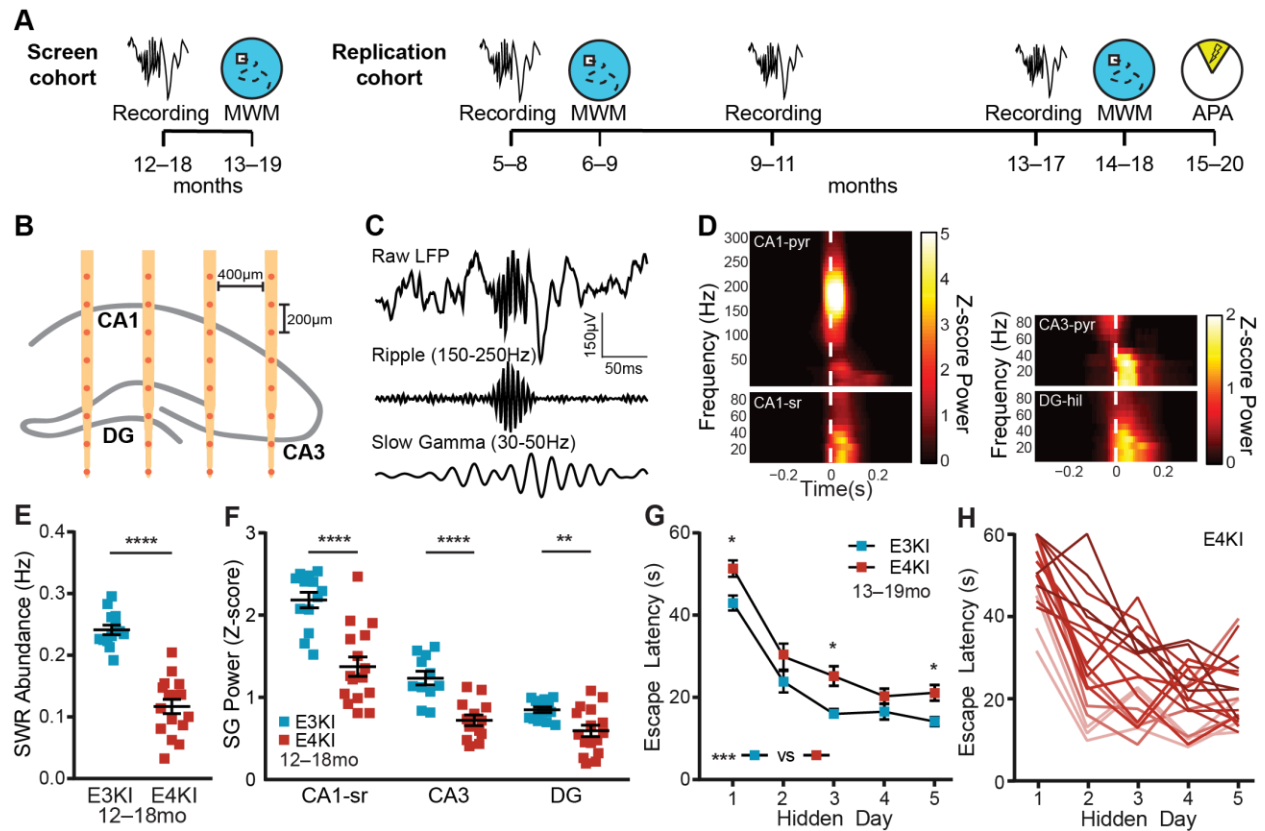


**Figure 2.1. Aged apoE4-KI mice show SWR deficits and spatial approach task impairments and variability.**

**(A)** Timeline of experiments. In the screen cohort, aged mice underwent recordings, then MWM 1 month later. In the replication cohort, young mice underwent recordings, then MWM 1 month later, another recording at middle age and old age, then MWM 1 month later and APA 2 months later.

**(B)** Schematic representation of probe placement in dorsal hippocampus, adapted with permission<sup>28</sup>.

**(C)** Representative raw, ripple filtered (150–250 Hz), and SG filtered (30–50 Hz) traces of a SWR event.

**(D)** Representative SWR-triggered spectrograms from CA1 pyramidal cell layer (CA1-pyr), CA1 stratum radiatum (CA1-sr), CA3 pyramidal cell layer (CA3-pyr), and dentate gyrus hilus (DG-hil) in an apoE3-KI mouse. White dashed lines represent threshold crossing for SWR detection.

**(E)** SWR abundance,  $n = 13$  apoE3-KI and  $n = 16$  apoE4-KI mice, aged 12–18 months (unpaired  $t$  test;  $t(27) = 8.42$ ,  $p < 0.0001$ ).

**(F)** Z-scored SG power during SWRs,  $n = 13$  apoE3-KI and  $n = 16$  apoE4-KI mice ( $n = 11$  and  $13$  for CA3), aged 12–18 months (unpaired  $t$  test,  $t(27) = 5.17$ ,  $p < 0.0001$  for CA1-sr; unpaired  $t$  test;  $t(22) = 4.91$ ,  $p < 0.0001$  for CA3; Mann-Whitney  $U = 45$ ,  $p = 0.0087$  for DG).

**(G)** Average daily escape latency on MWM,  $n = 20$  apoE3-KI and  $n = 19$  apoE4-KI mice, aged 13–19 months. Two-way repeated measures ANOVA of aligned rank transformed data shows significant effect of genotype ( $F(1,37) = 13.08$ ,  $p = 0.0009$ ) and post-hoc Mann-Whitney  $U$  test with Sidak adjustment shows significant difference on hidden days 1 ( $U = 95$ ,  $p = 0.033$ ), 3 ( $U = 95$ ,  $p = 0.034$ ), and 5 ( $U = 92$ ,  $p = 0.026$ ).

**(H)** ApoE4-KI mice show wide variation in extent of memory impairment. Escape latency curves colored from best (light) to worst (dark) average performance over all days.  
\* $p < 0.05$ ; \*\* $p < 0.01$ ; \*\*\*\* $p < 0.0001$ . Error bars indicate mean  $\pm$  SEM.

**Table 2.1. Sample sizes for all experiments.**

Age	Metric	Cohort 1		Cohort 2	
		apoE3-KI	apoE4-KI	apoE3-KI	apoE4-KI
5–8 months	SWR Abundance	--	--	13	17 <sup>a</sup>
	CA3 SG Power	--	--	12	16
	MWM	--	--	13	13
9–11 months	SWR Abundance	--	--	12 <sup>b</sup>	17
	CA3 SG Power	--	--	11 <sup>b</sup>	16
12–20 months	SWR Abundance	13	16	9 <sup>c</sup>	15 <sup>d</sup>
	CA3 SG Power	11	13	9 <sup>c</sup>	14 <sup>d</sup>
	MWM, Open Field, Elevated Plus	20	19	12 <sup>e</sup>	15 <sup>f</sup>
	APA, Hot Plate	--	--	12 <sup>e</sup>	13 <sup>g</sup>

<sup>a</sup>4 apoE4-KI mice aged 7 months were added to the study after the first MWM had been completed.

<sup>b</sup>Implant no longer functional in 1 apoE3-KI mouse

<sup>c</sup>Implant no longer functional in 2 apoE3-KI mice, 1 apoE3-KI mouse died

<sup>d</sup>Implant no longer functional in 1 apoE4-KI mouse, 1 apoE4-KI mouse died

<sup>e</sup>3 apoE3-KI mice died, 3 apoE3-KI mice added

<sup>f</sup>4 apoE4-KI mice died, 3 apoE4-KI mice added

<sup>g</sup>1 apoE4-KI mouse (added just for behavior) excluded due to motor deficits, 1 apoE4-KI mouse died

## SWR deficits predict spatial approach task impairments in aged apoE4-KI mice

Prediction of future outcomes is possible when the value of one variable measured at one time is related to the value of another variable measured at a later time. Prediction can be quantified by measuring the correlation between the two variables. We therefore began our search for a predictive feature by examining the relationship between electrophysiological measurements that showed significant differences between apoE3-KI and apoE4-KI mice and subsequent behavioral performance, focusing on MWM metrics previously shown to be impaired in apoE4-KI mice<sup>11,28</sup> (**Fig. 2.2A**). We began with a screen assessing the predictability of 22 behavioral metrics by 4 SWR properties for a total of 88 comparisons, 9 of which were significant with  $\alpha = 0.05$ ; far more than would be predicted by chance ( $p < 0.00032$ , binomial test assuming all initial tests are independent; see **Table 2.2**). Furthermore, to ensure that performance metrics were not redundant and captured distinct aspects of behavior, we only included behavior metrics that had an  $R^2 < 0.5$  with each other throughout this study.

In aged apoE4-KI mice, SWR abundance (events/s) predicted the slope of the escape latency curve – a measure of the speed of learning – over the first 2 or first 3 hidden days (**Fig. 2.2B** and **2.3B**). In order to follow individual mice over all measurements, points are colored by SWR abundance from lowest (blue) to highest (red). SWR abundance also predicted escape latency on hidden day 3 (**Fig. 2.2C**), a measure of approach efficacy. Because SWRs contribute to memory consolidation processes after an experience<sup>22</sup>, we also examined differences between the last trial of a day and the first trial of the next day, between which mice rested for 19 hours (**Fig. 2.3C**). SWR abundance predicted the extent of behavioral improvement over the first night (**Fig. 2.2D**), where high SWR abundance predicted improved performance overnight while lower SWR abundance predicted worse performance.



All of these measures relate to rapidity of learning across days, suggesting that lower SWR abundance in aged apoE4-KI mice contributes to slower learning, perhaps through impaired consolidation leading to reduced memory maintenance over days. We therefore combined these four metrics by calculating a z-score for each mouse and metric, reversing the sign of any metrics where lower values indicated better performance, and averaging all z-scores for each mouse. The resulting measure, the learning performance score, is positive to indicate above average performance and negative to indicate below average performance. SWR abundance (also z-scored) accounted for 51% of the variance of the subsequently measured learning performance score (**Fig. 2.2E**).

Interestingly, SWR-associated SG power in CA3 predicted several metrics of probe memory in aged apoE4-KI mice, but these metrics differ from those predicted by SWR abundance. In fact, we observed that SWR abundance and associated SG power in CA3 were not correlated, and, similarly, measures of early learning speed and of probe memory were not correlated, suggesting that these reflect two distinct reflections of spatial memory impairment. Some mice did not have electrode sites in CA3 and thus were excluded from this analysis (see **Table 2.1**). SWR-associated SG power in CA3 predicted the percent time spent exploring the quadrant that previously contained the platform on probes 1 and 2 (**Fig. 2.2F** and **2.3D**), a measure of retrieval of previously learned spatial information without feedback from the target. To more narrowly define the precision of target location memory, we examined target crossings, which require direct overlap with the previous platform location. CA3 SG power during SWRs predicted the number of target crossings on probe 1 (**Fig. 2.2G**). Additionally, to examine efficiency of memory retrieval, we measured the cumulative distance traveled toward the previous platform location during the initial approach (first 5 seconds; **Fig. 2.3E**). CA3 SG power during SWRs predicted

this metric for probes 1 and 2 (**Fig. 2.2H** and **2.3F**). All of these measures relate to precision of memory retrieval, suggesting that lower SWR-associated CA3 SG power in aged apoE4-KI mice reflects an impaired retrieval mechanism. As described above for the learning performance score, we combined these 5 metrics, z-scored, into a memory precision performance score. CA3 SG power during SWRs accounted for 77% of the variance in the subsequently measured memory precision score (**Fig. 2.2I**).

The quantity and strength of these preliminary predictive relationships were compelling enough to motivate a replication and extension of the initial study in a second cohort of animals. Importantly, the analyses of the screen cohort were completed before experiments on the replication cohort, allowing us to establish planned comparisons to determine whether findings from the screen cohort were robust and replicable. For the replication cohort, we implanted young animals (5–8 months) and periodically measured SWR properties in each individual mouse for up to 8 months. We assessed memory performance through MWM tasks at 6–9 months and again at 14–18 months and through an APA task at 15–20 months (**Fig. 2.1A** and **Table S1**).

In this replication cohort, studied two years – thus several generations of mice – later, we found that all relationships identified in the screen cohort remained significant (**Fig. 2.2J–R** and **2.3G–I**), far more than would be predicted by chance ( $p = 0$ , binomial test assuming all initial tests are independent). To test if this result could be affected by the number of tests, we applied a Holm-Sidak correction to all  $p$  values and found that 6 of the 9 comparisons still remained significant, again far more than would be predicted by chance ( $p = 0$ , binomial test assuming all initial tests are independent). As before, in order to follow individual mice over all measurements, points are colored by SWR abundance from lowest (blue) to highest (red). We also noted that these predictive relationships were consistent across the two cohorts despite differences in the mean values of SWR

abundance ( $\mu = 0.12$  Hz vs  $0.20$  Hz; unpaired t test,  $t(29) = 4.75$ ,  $p < 0.0001$ ) and in mean values of SWR baseline ( $\mu = 16.2$   $\mu$ V vs  $11.5$   $\mu$ V; unpaired t test,  $t(25) = 5.41$ ,  $p < 0.0001$ ), which may explain the difference in SWR abundance. These differences may have resulted from genetic drift across the multiple generations, colony conditions, or other factors, but could not have resulted from experimental factors such as probe type, probe placement, or experimenter, which were kept constant across cohorts.

Calculating z-scores allowed us to normalize for this difference between the two cohorts, and thus ask whether the predictive measures derived from the screen cohort predicted behavioral performance in the replication cohort. This can be seen as a form of validation, where relationships derived from a training set (screen cohort) are validated through application to a test set (replication cohort). These predictions were remarkably accurate, capturing 56% of the variance in the actual learning performance score and 79% of the variance in the actual memory precision performance score (**Fig. 2.2N** and **2.2R**). Thus, deficits in SWR abundance and associated CA3 SG power, z-scored across the population, predict early learning and memory precision impairment, respectively, even when applied to a separate cohort of animals.

These predictive relationships were also robust: we determined that none of the correlations in this study were driven by a single data point (see STAR Methods). The width of the age range did not affect the results, as age within this cohort did not significantly correlated with SWR properties or MWM performance. We also confirmed that the predictive relationships remained significant regardless of the frequency band (150–250 Hz vs 125–250 Hz) or threshold (3 SD vs 5 SD) used for SWR detection (**Table 2.2**). These predictive relationships are unlikely to be driven by differences in SWR detection, as mean and standard deviation of the ripple-filtered trace and multi-unit firing rate during SWRs were not correlated with SWR abundance or any behavioral

measure. We further established in the replication cohort that there were no genotype differences in anxiety or exploratory drive as measured by open field and elevated plus maze tests, in pain response as measured by a hot plate test, or in visual acuity as measured by MWM trials with the platform marked (**Fig. 2.4**). Moreover, none of these non-spatial behaviors significantly correlated with spatial task performance or with SWR properties at  $\alpha = 0.05$ . Therefore, spatial performance differences were most likely driven by spatial memory ability, and SWR-related network alterations were specifically related to this spatial memory impairment. Additionally, SWR-associated SG power in CA1 and in DG did not consistently and significantly predict memory performance (**Table 2.2**), thus, we focused only on SWR abundance and associated CA3 SG power for the remainder of the study.

These consistent predictive relationships were also specific to apoE4-KI mice. While we identified some predictive relationships between SWR properties and memory in the screen cohort of aged apoE3-KI mice (**Table 2.2**), the majority did not replicate in the replication cohort. This may be the result of a ceiling effect given the higher levels of both SWR abundance and associated CA3 SG power in apoE3-KI mice (**Fig. 2.1E** and **2.1F**; for example see **Fig. 2.3J**). The one relationship that did replicate across both apoE3-KI cohorts was that SWR abundance predicted escape latency on the second day (**Fig. 2.3K** and **2.3L**). Thus, SWR abundance may be related to early learning speed in both control and AD model mice.

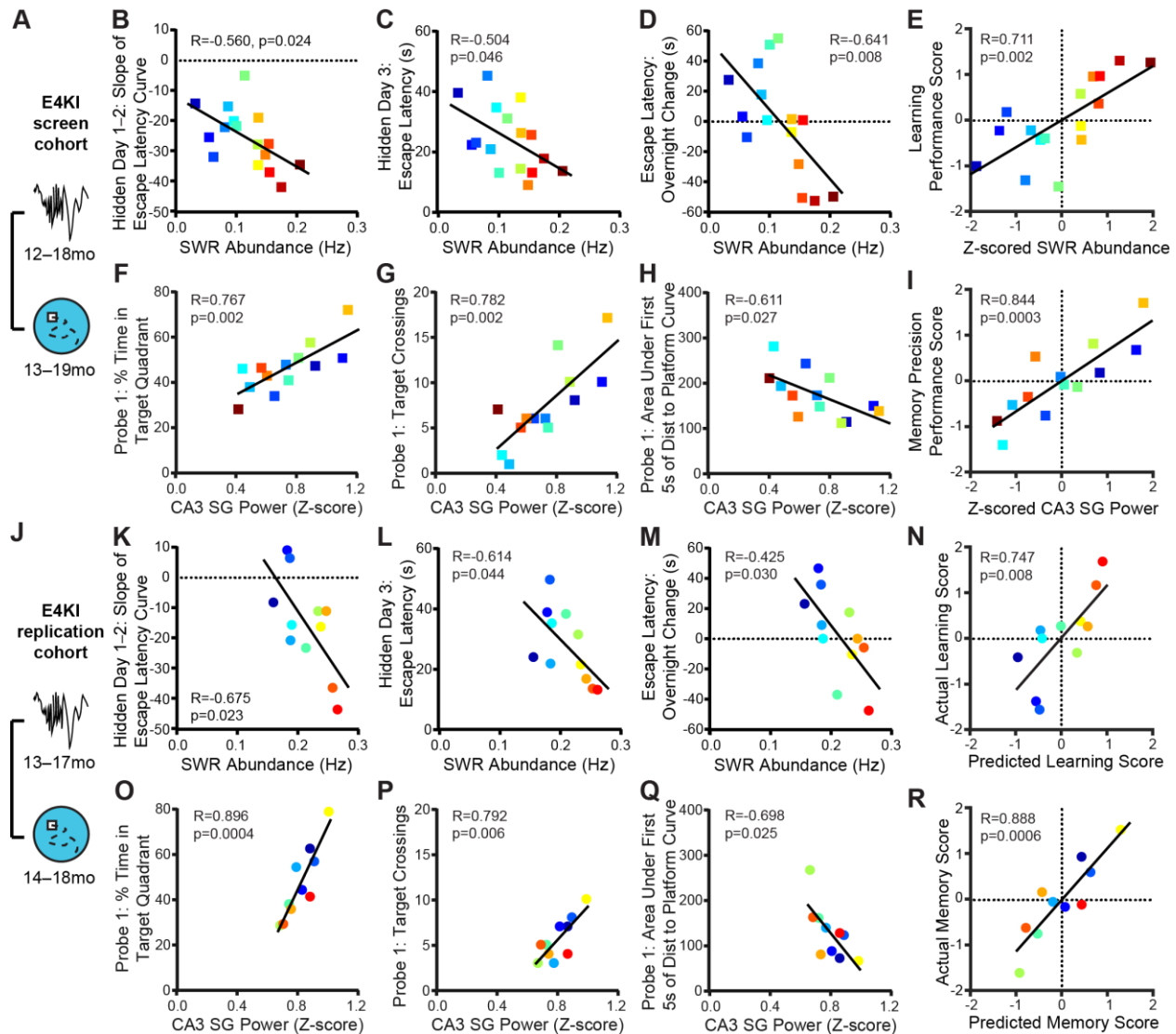


**Figure 2.2. SWR deficits predicts spatial approach task impairments in aged apoE4-KI mice**

(A) Timeline of experiments shown in B–I.

(B–D) SWR abundance predicts (B) slope of escape latency over hidden days 1–2 ( $F(1,14) = 6.41$ ), (C) average escape latency on hidden day 3 ( $F(1,14) = 4.77$ ), and (D) change in escape latency between the last trial of hidden day 1 and the first trial of hidden day 2 ( $F(1,14) = 9.76$ ),  $n = 16$  mice.

(E) Z-scored SWR abundance predicts learning performance score ( $F(1,14) = 14.3$ ),  $n = 16$  mice.

(F–H) CA3 SG power during SWRs predicts (F) percent time spent in quadrant that previously contained the platform ( $F(1,11) = 15.75$ ), (G) number of times crossing the previous platform location ( $F(1,11) = 17.3$ ), and (H) area under the curve of the distance to the prior platform location during the first 5 seconds of probe 1 ( $F(1,11) = 6.55$ ),  $n = 13$  mice.

(I) Z-scored CA3 slow gamma power during SWRs predicts memory precision performance score ( $F(1,11) = 27.3$ ),  $n = 13$  mice.

In B–I, apoE4-KI mice aged 12–18 months at electrophysiological recording and 13–19 months at MWM.

**(J)** Timeline of experiments shown in K–R.

**(K–M)** In a replication experiment in a separate cohort of animals, SWR abundance predicts **(K)** slope of escape latency over hidden days 1–2 ( $F(1,9) = 7.51$ , adjusted  $p = 0.067$ ), **(L)** average escape latency on hidden day 3 ( $F(1,9) = 5.45$ , adjusted  $p = 0.044$ ), and **(M)** change in escape latency between the last trial of hidden day 1 and the first trial of hidden day 2 ( $F(1,9) = 6.66$ , adjusted  $p = 0.059$ ),  $n = 11$  mice.

**(N)** Learning performance score as predicted by the linear model in E predicts actual learning performance score ( $F(1,9) = 11.4$ ),  $n = 11$  mice.

**(O–Q)** In a replication experiment in a separate cohort of animals, CA3 SG power during SWRs predicts **(O)** percent time spent in quadrant that previously contained the platform ( $F(1,8) = 32.64$ , adjusted  $p = 0.002$ ), **(P)** number of times crossing the previous platform location ( $F(1,8) = 13.48$ , adjusted  $p = 0.025$ ), and **(Q)** area under the curve of the distance to the prior platform location during the first 5 seconds of probe ( $F(1,8) = 7.61$ , adjusted  $p = 0.049$ ),  $n = 10$  mice.

**(R)** Memory precision performance score as predicted by the linear model in I predicts actual memory precision performance score ( $F(1,8) = 30.1$ ),  $n = 10$  mice.

In K–R, apoE4-KI mice aged 13–17 months at electrophysiological recording and 14–18 months at MWM. Multiplicity adjusted  $p$  values with the Holm-Sidak method.

Pearson correlations of apoE4-KI mice. Points colored in order of SWR abundance from blue (lowest) to red (highest).

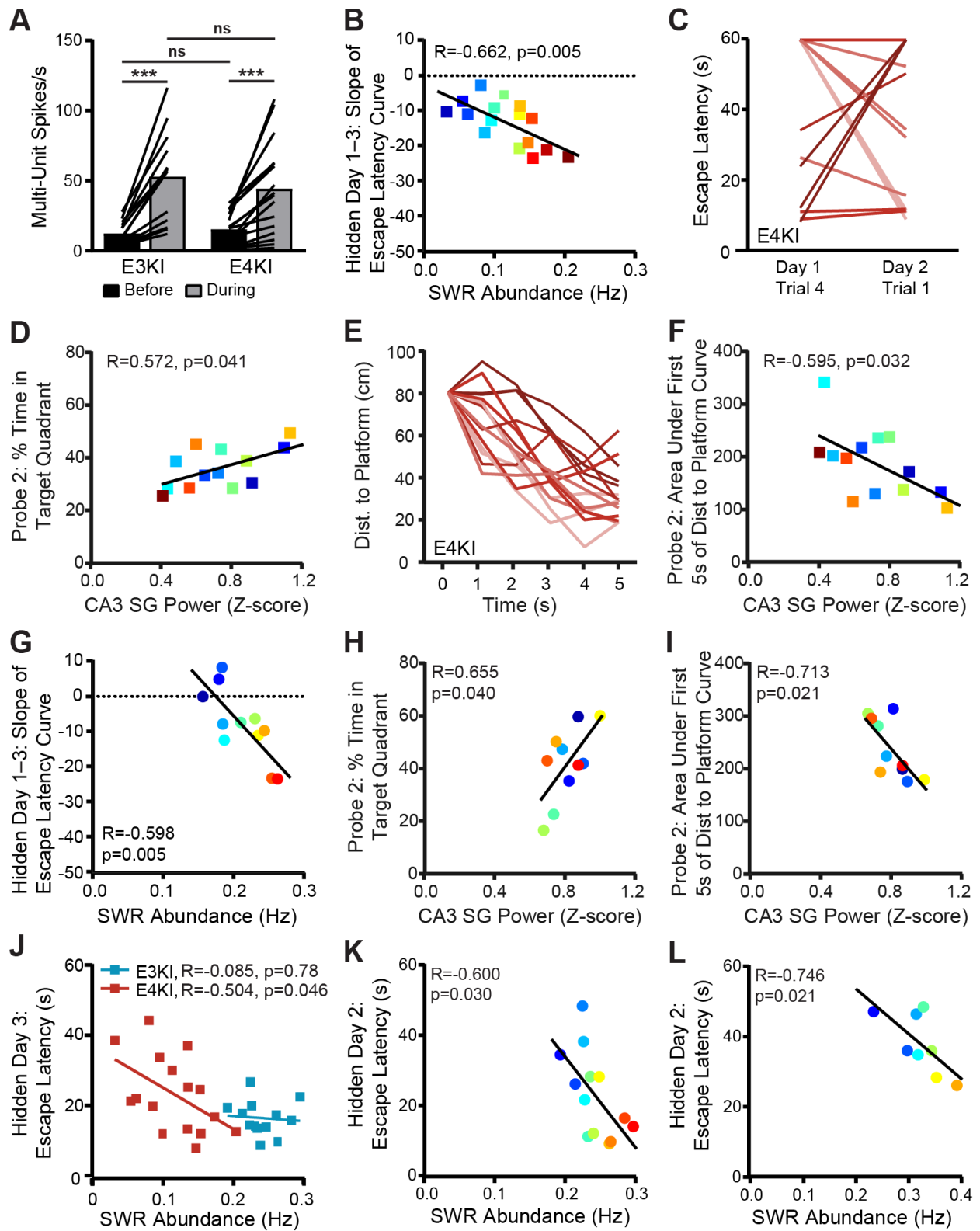


**Figure 2.3. Further predictive relationships identified in the screen cohort and examples of behavioral metrics used in correlations.**

(A) Multi-unit activity increases from baseline (400 ms before SWR detection) to during SWRs (0–100 ms after detection) in apoE3-KI ( $t(12) = 5.54$ ,  $p = 0.0001$ ) and apoE4-KI ( $t(15) = 4.56$ ,  $p = 0.0004$ ) mice. No difference between genotypes before ( $t(27) = 0.78$ ,  $p = 0.21$ ) or during ( $t(27) = 0.67$ ,  $p = 0.94$ ) SWRs.  $N = 13$  apoE3-KI and  $n = 16$  apoE4-KI mice aged 12–18 months, paired  $t$  test.

(B) SWR abundance predicts slope of escape latency over hidden days 1–3 ( $F(1,14) = 10.91$ ),  $n = 16$  mice.

(C) Individual apoE4-KI mouse escape latency curves over hidden sessions, showing difference between day 1, trial 4 and day 2, trial 1 (overnight), colored from most negative (light) to most positive (dark),  $n = 16$  mice.

(D) CA3 SG power during SWRs predicts percent time spent in quadrant that previously contained the platform on probe 2 ( $F(1,11) = 5.34$ ),  $n = 13$  mice.

(E) Individual apoE4-KI mouse distance to platform curves during the first 5 seconds of probe 1, colored from best (light) to worst (dark) cumulative distance to platform over the curve,  $n = 16$  mice.

(F) CA3 SG power during SWRs predicts area under the curve of the distance to the prior platform location during the first 5 seconds of probe 2 ( $F(1,11) = 6.01$ ),  $n = 13$  mice.

In B–F, apoE4-KI mice aged 12–18 months at electrophysiological recording and 13–19 months at MWM.

(G) In a replication experiment in a separate cohort of animals, SWR abundance predicts slope of escape latency over hidden days 1–3 ( $F(1,9) = 13.39$ , adjusted  $p = 0.021$ ),  $n = 11$  mice.

(H,I) In a replication experiment in a separate cohort of animals, CA3 SG power during SWRs predicts (H) percent time spent in quadrant that previously contained the platform ( $F(1,8) = 6.02$ , adjusted  $p = 0.04$ ) and (I) area under the curve of the distance to the prior platform location during the first 5 seconds of probe 2 ( $F(1,8) = 8.27$ , adjusted  $p = 0.06$ ),  $n = 10$  mice.

In G–I, apoE4-KI mice aged 13–17 months at electrophysiological recording and 14–18 months at MWM. Multiplicity adjusted  $p$  values with the Holm-Sidak method.

(J) Example of how SWR abundance for apoE3-KI mice does not overlap with that of apoE4-KI mice and does not predict escape latency for apoE3-KI mice, demonstrating a ceiling effect ( $F(1,11) = 0.80$  for apoE3-KI,  $n = 13$ ;  $F(1,14) = 4.77$  for apoE4-KI,  $n = 16$ ). Mice aged 12–18 months at electrophysiological recording and 13–19 months at MWM.

(K) SWR abundance predicts average escape latency on hidden day 2 ( $F(1,11) = 6.19$ ).  $N = 13$  apoE3-KI mice aged 12–18 months at electrophysiological recording and 13–19 months at MWM.

(L) In a replication cohort, SWR abundance predicts average escape latency on hidden day 2 ( $F(1,7) = 8.79$ ).  $N = 9$  apoE3-KI mice aged 13–17 months at electrophysiological recording and 14–18 months at MWM.

Points colored in order of SWR abundance from blue (lowest) to red (highest). Pearson correlations.



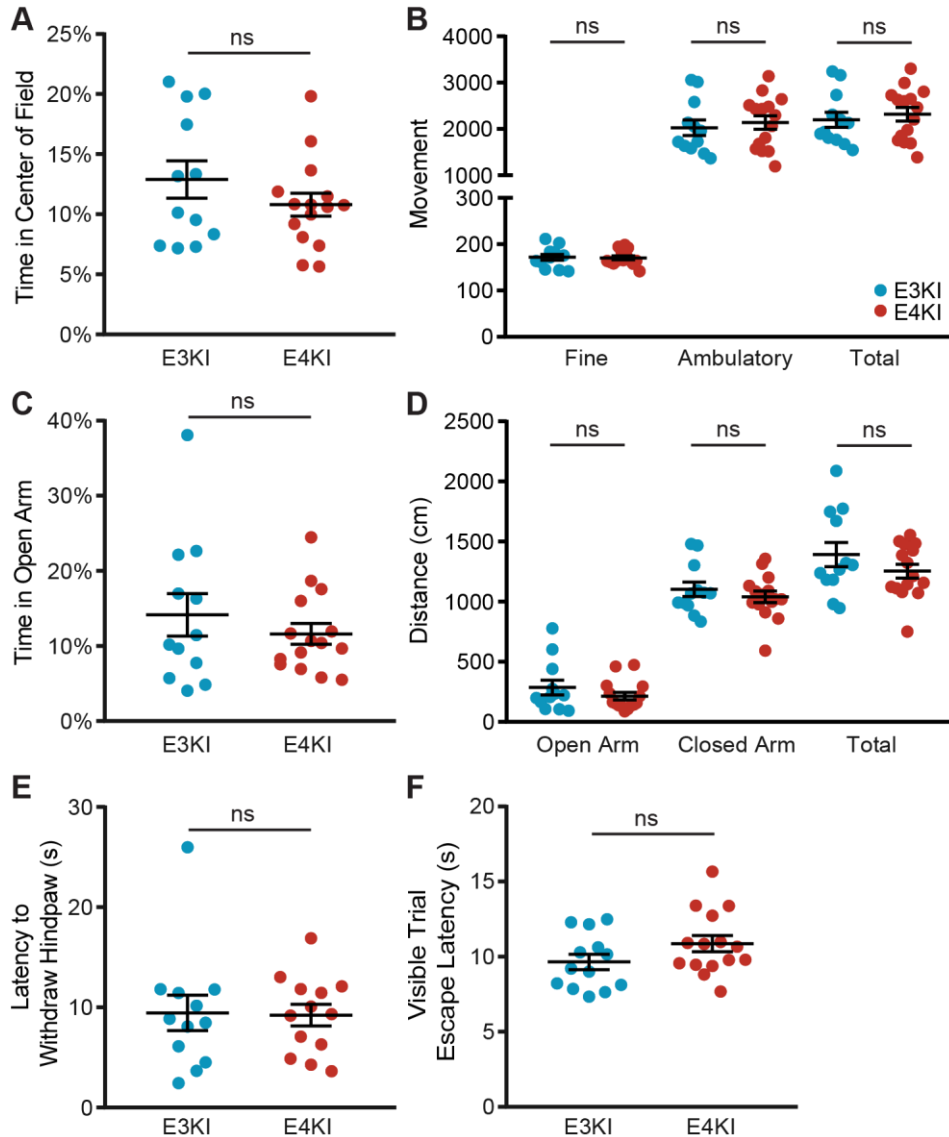


**Figure 2.4. ApoE4-KI mice are not impaired in non-spatial behaviors.**

(A) Percent time in center of open field ( $t(25) = 1.19, p = 0.24$ ).

(B) Number of instances of detected movement in the open field ( $t(25) = 0.19, p = 0.80$  for fine;  $t(25) = 0.52, p = 0.61$  for ambulatory; and  $t(25) = 0.54, p = 0.60$  for total).

(C) Percent time in open arm of elevated plus maze ( $t(25) = 0.84, p = 0.41$ ).

(D) Distance travelled in elevated plus arms (Mann-Whitney  $U = 72.5, p = 0.41$  for open arms;  $t(25) = 0.81, p = 0.43$  for closed arms;  $t(25) = 1.25, p = 0.22$  for total movement).

(E) Latency to withdraw hind paw on hot plate (Mann-Whitney  $U = 66, p = 0.54$ ).  $N = 12$  apoE3-KI and  $n = 13$  apoE4-KI mice, aged 15–20 months.

(F) Escape latency on MWM trials with platform labeled with flag ( $t(25) = 1.26, p = 0.22$ ).

$N = 12$  apoE3-KI and  $n = 15$  apoE4-KI mice, aged 14–18 months, unless otherwise specified. All tests are unpaired  $t$  tests unless otherwise specified. Error bars indicate mean  $\pm$  SEM.

**Table 2.2. Relationships between SWR properties and MWM performance tested in screen cohort.**

ApoE4-KI Metric	SWR Abundance				CA3 SG Power			
	R	F	DFn, DFd	P value	R	F	DFn, DFd	P value
Slope of Escape Latency Days 1–2	<b>-0.56</b>	<b>6.41</b>	<b>1, 14</b>	<b>0.024</b>	0.28	0.94	1, 11	0.35
Slope of Escape Latency Days 1–3	<b>-0.66</b>	<b>10.91</b>	<b>1, 14</b>	<b>0.0052</b>	0.48	3.29	1, 11	0.10
Slope of Escape Latency Days 1–4	-0.18	0.45	1, 14	0.51	0.43	2.43	1, 11	0.15
Slope of Escape Latency Days 1–5	0.14	0.29	1, 14	0.60	0.15	0.26	1, 11	0.62
Escape Latency Day 1	0.33	1.74	1, 14	0.21	-0.46	2.89	1, 11	0.12
Escape Latency Day 2	-0.19	0.51	1, 14	0.49	-0.03	0.01	1, 11	0.92
Escape Latency Day 3	<b>-0.5</b>	<b>4.77</b>	<b>1, 14</b>	<b>0.046</b>	0.15	0.27	1, 11	0.61
Escape Latency Day 4	0.35	1.97	1, 14	0.18	-0.12	0.15	1, 11	0.71
Escape Latency Day 5	0.35	1.92	1, 14	0.19	-0.14	0.24	1, 11	0.64
Night 1 Learning	<b>-0.64</b>	<b>9.76</b>	<b>1, 14</b>	<b>0.0075</b>	0.38	1.84	1, 11	0.20
Night 2 Learning	-0.36	2.06	1, 14	0.17	-0.17	0.33	1, 11	0.58
Night 3 Learning	-0.03	0.01	1, 14	0.92	-0.18	0.38	1, 11	0.55
Night 4 Learning	-0.05	0.04	1, 14	0.85	-0.36	1.65	1, 11	0.23
Probe 1 % in Target Quadrant	-0.11	0.16	1, 14	0.69	<b>0.77</b>	<b>15.75</b>	<b>1, 11</b>	<b>0.0022</b>
Probe 2 % in Target Quadrant	-0.03	0.02	1, 14	0.90	<b>0.57</b>	<b>5.34</b>	<b>1, 11</b>	<b>0.041</b>
Probe 3 % in Target Quadrant	-0.13	0.23	1, 14	0.64	-0.37	1.77	1, 11	0.21
Probe 1 Target Crossings	0.12	0.21	1, 14	0.65	<b>0.78</b>	<b>17.3</b>	<b>1, 11</b>	<b>0.0016</b>
Probe 2 Target Crossings	0.03	0.02	1, 14	0.90	0.43	2.52	1, 11	0.14
Probe 3 Target Crossings	0.21	0.63	1, 14	0.44	-0.36	1.61	1, 11	0.23
Probe 1 Dist to Platform Curve	0.1	0.15	1, 14	0.71	<b>-0.61</b>	<b>6.55</b>	<b>1, 11</b>	<b>0.027</b>
Probe 2 Dist to Platform Curve	0.03	0.02	1, 14	0.90	<b>-0.59</b>	<b>6.01</b>	<b>1, 11</b>	<b>0.032</b>
Probe 3 Dist to Platform Curve	0.19	0.5	1, 14	0.49	-0.33	1.38	1, 11	0.27

Metric	CA1-sr SG Power				DG SG Power			
	R	F	DFn, DFd	P value	R	F	DFn, DFd	P value
Slope of Escape Latency Days 1–2	0.1	0.14	1, 14	0.72	0.1	0.15	1, 14	0.71
Slope of Escape Latency Days 1–3	-0.05	0.03	1, 14	0.87	0	0	1, 14	0.99
Slope of Escape Latency Days 1–4	0	0	1, 14	1	0.02	0.01	1, 14	0.94
Slope of Escape Latency Days 1–5	-0.02	0	1, 14	0.95	0.05	0.04	1, 14	0.85
Escape Latency Day 1	0.11	0.17	1, 14	0.69	-0.27	1.13	1, 14	0.31
Escape Latency Day 2	0.14	0.28	1, 14	0.61	-0.12	0.20	1, 14	0.66
Escape Latency Day 3	0.04	0.02	1, 14	0.89	-0.23	0.79	1, 14	0.39
Escape Latency Day 4	0.19	0.54	1, 14	0.48	-0.27	1.12	1, 14	0.31
Escape Latency Day 5	0.09	0.12	1, 14	0.73	-0.3	1.39	1, 14	0.26
Night 1 Learning	0.25	0.92	1, 14	0.35	0.13	0.24	1, 14	0.63
Night 2 Learning	0.15	0.32	1, 14	0.58	-0.1	0.14	1, 14	0.71
Night 3 Learning	0.41	2.85	1, 14	0.11	-0.04	0.03	1, 14	0.87
Night 4 Learning	0.18	0.46	1, 14	0.51	-0.17	0.44	1, 14	0.52
Probe 1 % in Target Quadrant	0.1	0.13	1, 14	0.72	0.02	0.01	1, 14	0.94
Probe 2 % in Target Quadrant	-0.21	0.66	1, 14	0.43	0.02	0	1, 14	0.95
Probe 3 % in Target Quadrant	0.13	0.24	1, 14	0.63	0.15	0.30	1, 14	0.59
Probe 1 Target Crossings	0.48	4.15	1, 14	0.06	0.44	3.32	1, 14	0.09
Probe 2 Target Crossings	0.15	0.32	1, 14	0.58	-0.01	0	1, 14	0.98
Probe 3 Target Crossings	-0.12	0.21	1, 14	0.66	-0.28	1.19	1, 14	0.29
Probe 1 Dist to Platform Curve	0.15	0.33	1, 14	0.57	-0.35	1.98	1, 14	0.18
Probe 2 Dist to Platform Curve	0.05	0.04	1, 14	0.84	-0.31	1.49	1, 14	0.24
Probe 3 Dist to Platform Curve	-0.43	3.21	1, 14	0.10	-0.18	0.46	1, 14	0.51

ApoE3-KI	SWR Abundance				CA3 SG Power			
Metric	R	F	DFn, DFd	P value	R	F	DFn, DFd	P value
Slope of Escape Latency Days 1–2	-0.35	1.55	1, 11	0.24	-0.14	0.18	1, 9	0.68
Slope of Escape Latency Days 1–3	0.43	2.45	1, 11	0.15	0.18	0.32	1, 9	0.59
Slope of Escape Latency Days 1–4	0.33	1.33	1, 11	0.27	0.05	0.02	1, 9	0.89
Slope of Escape Latency Days 1–5	0.10	0.11	1, 11	0.74	0.2	0.39	1, 9	0.55
Escape Latency Day 1	-0.43	2.46	1, 11	0.15	-0.24	0.55	1, 9	0.48
Escape Latency Day 2	<b>-0.60</b>	<b>6.19</b>	<b>1, 11</b>	<b>0.03</b>	-0.28	0.79	1, 9	0.40
Escape Latency Day 3	-0.08	0.08	1, 11	0.78	-0.16	0.24	1, 9	0.63
Escape Latency Day 4	0.22	0.58	1, 11	0.46	0.02	0	1, 9	0.96
Escape Latency Day 5	0.25	0.72	1, 11	0.42	-0.04	0.02	1, 9	0.90
Night 1 Learning	0.05	0.02	1, 11	0.88	-0.09	0.07	1, 9	0.80
Night 2 Learning	0.44	2.68	1, 11	0.13	-0.25	0.58	1, 9	0.46
Night 3 Learning	-0.09	0.08	1, 11	0.78	0.35	1.22	1, 9	0.30
Night 4 Learning	-0.46	2.98	1, 11	0.11	-0.28	0.79	1, 9	0.40
Probe 1 % in Target Quadrant	-0.22	0.56	1, 11	0.47	-0.07	0.04	1, 9	0.84
Probe 2 % in Target Quadrant	-0.06	0.03	1, 11	0.86	0.45	2.31	1, 9	0.16
Probe 3 % in Target Quadrant	-0.08	0.08	1, 11	0.78	-0.22	0.45	1, 9	0.52
Probe 1 Target Crossings	-0.21	0.52	1, 11	0.49	-0.06	0.03	1, 9	0.87
Probe 2 Target Crossings	0.05	0.02	1, 11	0.88	0.24	0.54	1, 9	0.48
Probe 3 Target Crossings	-0.24	0.66	1, 11	0.43	0.25	0.58	1, 9	0.46
Probe 1 Dist to Platform Curve	0.47	3.2	1, 11	0.10	0.16	0.24	1, 9	0.64
Probe 2 Dist to Platform Curve	0.45	2.8	1, 11	0.12	0.10	0.09	1, 9	0.77
Probe 3 Dist to Platform Curve	0.35	1.49	1, 11	0.25	0.18	0.32	1, 9	0.59

Metric	CA1-sr SG Power				DG SG Power			
	R	F	DFn, DFd	P value	R	F	DFn, DFd	P value
Slope of Escape Latency Days 1–2	0.33	1.31	1, 11	0.28	-0.01	0	1, 11	0.98
Slope of Escape Latency Days 1–3	-0.12	0.17	1, 11	0.69	<b>0.77</b>	<b>15.53</b>	<b>1, 11</b>	<b>0.002</b>
Slope of Escape Latency Days 1–4	-0.05	0.03	1, 11	0.87	0.49	3.5	1, 11	0.09
Slope of Escape Latency Days 1–5	-0.34	1.41	1, 11	0.26	0.51	3.79	1, 11	0.08
Escape Latency Day 1	0.29	1.02	1, 11	0.33	<b>-0.74</b>	<b>13.17</b>	<b>1, 11</b>	<b>0.004</b>
Escape Latency Day 2	0.48	3.26	1, 11	0.10	<b>-0.55</b>	<b>4.85</b>	<b>1, 11</b>	<b>0.0499</b>
Escape Latency Day 3	0.34	1.40	1, 11	0.26	-0.1	0.11	1, 11	0.75
Escape Latency Day 4	0.47	3.11	1, 11	0.11	-0.27	0.84	1, 11	0.38
Escape Latency Day 5	0.33	1.35	1, 11	0.27	-0.38	1.81	1, 11	0.21
Night 1 Learning	-0.04	0.01	1, 11	0.91	0.39	1.98	1, 11	0.19
Night 2 Learning	0.1	0.12	1, 11	0.74	0.04	0.02	1, 11	0.90
Night 3 Learning	0.14	0.22	1, 11	0.65	-0.33	1.33	1, 11	0.27
Night 4 Learning	-0.23	0.62	1, 11	0.45	0.16	0.29	1, 11	0.60
Probe 1 % in Target Quadrant	-0.02	0.01	1, 11	0.94	0.35	1.56	1, 11	0.24
Probe 2 % in Target Quadrant	-0.13	0.19	1, 11	0.67	-0.16	0.28	1, 11	0.60
Probe 3 % in Target Quadrant	0.15	0.27	1, 11	0.62	-0.24	0.7	1, 11	0.42
Probe 1 Target Crossings	-0.41	2.26	1, 11	0.16	<b>0.66</b>	<b>8.41</b>	<b>1, 11</b>	<b>0.015</b>
Probe 2 Target Crossings	-0.05	0.02	1, 11	0.88	0.41	2.19	1, 11	0.17
Probe 3 Target Crossings	-0.08	0.06	1, 11	0.81	-0.12	0.17	1, 11	0.69
Probe 1 Dist to Platform Curve	0.14	0.21	1, 11	0.65	-0.01	0	1, 11	0.97
Probe 2 Dist to Platform Curve	<b>0.68</b>	<b>9.5</b>	<b>1, 11</b>	<b>0.01</b>	-0.39	1.98	1, 11	0.19
Probe 3 Dist to Platform Curve	<b>0.69</b>	<b>10.04</b>	<b>1, 11</b>	<b>0.089</b>	-0.35	1.5	1, 11	0.25

ApoE4-KI	150–250 Hz 3 SD SWR Abundance				150–250 Hz 5 SD SWR Abundance			
Metric	R	F	DFn, DFd	P value	R	F	DFn, DFd	P value
Slope of Escape Latency Days 1-2	<b>-0.62</b>	<b>8.76</b>	<b>1, 14</b>	<b>0.01</b>	<b>-0.56</b>	<b>6.41</b>	<b>1, 14</b>	<b>0.024</b>
Slope of Escape Latency Days 1-3	<b>-0.73</b>	<b>16.07</b>	<b>1, 14</b>	<b>0.0013</b>	<b>-0.66</b>	<b>10.91</b>	<b>1, 14</b>	<b>0.0052</b>
Escape Latency Day 3	<b>-0.62</b>	<b>8.96</b>	<b>1, 14</b>	<b>0.0097</b>	<b>-0.5</b>	<b>4.77</b>	<b>1, 14</b>	<b>0.046</b>
Night 1 Learning	<b>-0.6</b>	<b>7.96</b>	<b>1, 14</b>	<b>0.014</b>	<b>-0.64</b>	<b>9.76</b>	<b>1, 14</b>	<b>0.0075</b>
ApoE4-KI	125–250 Hz 3 SD SWR Abundance				125–250 Hz 5 SD SWR Abundance			
Metric	R	F	DFn, DFd	P value	R	F	DFn, DFd	P value
Slope of Escape Latency Days 1-2	<b>-0.55</b>	<b>5.99</b>	<b>1, 14</b>	<b>0.028</b>	<b>-0.57</b>	<b>6.69</b>	<b>1, 14</b>	<b>0.022</b>
Slope of Escape Latency Days 1-3	<b>-0.62</b>	<b>8.71</b>	<b>1, 14</b>	<b>0.011</b>	<b>-0.6</b>	<b>7.76</b>	<b>1, 14</b>	<b>0.015</b>
Escape Latency Day 3	<b>-0.6</b>	<b>7.73</b>	<b>1, 14</b>	<b>0.015</b>	<b>-0.54</b>	<b>5.68</b>	<b>1, 14</b>	<b>0.032</b>
Night 1 Learning	<b>-0.51</b>	<b>4.92</b>	<b>1, 14</b>	<b>0.044</b>	<b>-0.64</b>	<b>9.47</b>	<b>1, 14</b>	<b>0.0082</b>
ApoE4-KI	150–250 Hz 3 SD CA3 SG Power				150–250 Hz 5 SD CA3 SG Power			
Metric	R	F	DFn, DFd	P value	R	F	DFn, DFd	P value
Probe 1 % in Target Quadrant	<b>0.77</b>	<b>15.66</b>	<b>1, 11</b>	<b>0.0022</b>	<b>15.75</b>	<b>1, 11</b>	<b>0.0022</b>	<b>15.75</b>
Probe 2 % in Target Quadrant	<b>0.61</b>	<b>6.44</b>	<b>1, 11</b>	<b>0.028</b>	<b>5.34</b>	<b>1, 11</b>	<b>0.041</b>	<b>5.34</b>
Probe 1 Target Crossings	<b>0.74</b>	<b>13.13</b>	<b>1, 11</b>	<b>0.004</b>	<b>0.78</b>	<b>17.3</b>	<b>1, 11</b>	<b>0.0016</b>
Probe 1 Dist to Platform Curve	<b>-0.65</b>	<b>8.03</b>	<b>1, 11</b>	<b>0.016</b>	<b>-0.61</b>	<b>6.55</b>	<b>1, 11</b>	<b>0.027</b>
Probe 2 Dist to Platform Curve	<b>-0.57</b>	<b>5.42</b>	<b>1, 11</b>	<b>0.04</b>	<b>-0.59</b>	<b>6.01</b>	<b>1, 11</b>	<b>0.032</b>
ApoE4-KI	125–250 Hz 3 SD CA3 SG Power				125–250 Hz 5 SD CA3 SG Power			
Metric	R	F	DFn, DFd	P value	R	F	DFn, DFd	P value
Probe 1 % in Target Quadrant	<b>0.65</b>	<b>8.01</b>	<b>1, 11</b>	<b>0.016</b>	<b>0.72</b>	<b>11.91</b>	<b>1, 11</b>	<b>0.0054</b>
Probe 2 % in Target Quadrant	<b>0.58</b>	<b>5.49</b>	<b>1, 11</b>	<b>0.039</b>	<b>0.6</b>	<b>6.22</b>	<b>1, 11</b>	<b>0.03</b>
Probe 1 Target Crossings	<b>0.61</b>	<b>6.49</b>	<b>1, 11</b>	<b>0.027</b>	<b>0.68</b>	<b>9.34</b>	<b>1, 11</b>	<b>0.011</b>
Probe 1 Dist to Platform Curve	<b>-0.64</b>	<b>7.68</b>	<b>1, 11</b>	<b>0.018</b>	<b>-0.65</b>	<b>8.16</b>	<b>1, 11</b>	<b>0.016</b>
Probe 2 Dist to Platform Curve	<b>-0.59</b>	<b>5.81</b>	<b>1, 11</b>	<b>0.035</b>	<b>-0.58</b>	<b>5.61</b>	<b>1, 11</b>	<b>0.037</b>

Bold values indicate significant correlations.

## SWR deficits predict spatial avoidance task impairments in aged apoE4-KI mice

A robust predictor of memory decline should generalize across tasks, so we next assessed the predictive capacity of SWR properties for subsequent performance on the APA task (**Fig. 2.5A**), a spatial avoidance task<sup>40</sup>. In this task, mice explore a rotating arena and must use distal cues to avoid a shock zone that is fixed relative to the room across daily 10 min trials for 4 days. As this task has not been previously used in AD models, we first asked whether there was an overall effect of apoE genotype. ApoE4-KI mice task acquisition was significantly impaired on day 1: mice had greater number of entrances into the shock zone (**Fig. 2.5B**), travelled less distance (**Fig. 2.6A**), spent less time in the quadrant opposite the shock zone (**Fig. 2.6B**), and moved further from the shock zone in bouts of movement (**Fig. 2.6C**). Performance on the probe trial, in which the shock was inactivated, was also impaired (**Fig. 2.6D**). Thus, APA is able to identify significant behavioral differences between aged apoE4-KI and apoE3-KI mice.

We then determined which behavioral metrics correlated with SWR properties, noting that, as in MWM, there was substantial variability in apoE4-KI mice (**Fig. 2.6E**). In total, we compared 5 behavioral metrics over 4 days against 2 SWR properties for a total of 40 comparisons, 8 of which were significant with  $\alpha = 0.05$ ; far more than would be predicted by chance ( $p < 0.00071$ , binomial test assuming all initial tests are independent; see **Table 2.3**). The majority of significant comparisons were found on day 2. Focusing on day 2, we again corrected for multiple comparisons and found that 2 of the 5 comparisons remained significant, which had a 7.5% probability of occurring by chance (binomial test assuming all initial tests are independent). To gain further insight into potential drivers of these significant relationships, we computed the variance in the number of shock zone entrances across animals for days 1 and 2 and found that day 2 variances were higher (mean entrances day 1  $\sigma^2 = 15.76$  vs day 2  $\sigma^2 = 33.82$  mean entrances), suggesting day

2 performance would be more effective for assessing predictive validity. In addition, day 2 performance predicted day 3 and 4 performance, and apoE4-KI mice separated out into two distinct performance populations on day 2 such that the top 50% of performers on day 2 continued to learn on days 3 and 4 and that the bottom 50% did not (**Fig. 2.6F** and **2.6G**). These findings led us to focus on day 2 performance, as it captured much of the overall learning curve.

SWR abundance measured 2 months before task training predicted the latency to first entrance on day 2, a measure of memory of the shock location assessed 24 hours after the previous training trial and before receiving any feedback in that trial (**Fig. 2.5C**). This result closely parallels the measure for overnight consolidation in the MWM task, which also correlated with SWR abundance (**Fig. 2.2D** and **2.2M**). SWR abundance also predicted path length and percent time in the quadrant opposite the target on day 2 (**Fig. 2.5D** and **2.5E**). Together, these findings suggest that SWR abundance deficits in apoE4-KI mice are related to avoidance efficacy, just as it correlated with approach efficacy on hidden day 3 of the MWM (**Fig. 2.2C** and **2.2L**). We therefore calculated a learning performance score for the APA task in the same manner as for the MWM task (mean for each animal across the z-scored metrics shown in **Fig. 2.5D** and **2.5E**) and used the predictive relationship derived from the screen cohort to assess our ability to predict relative behavioral impairments from SWR abundance. Strikingly, the relationship between the predicted and actual learning performance scores was very strong, with the predicted score accounting for 75% of the variance in the actual score (**Fig. 2.5F**).

A similar pattern of predictability was seen for CA3 SG power during SWRs. This SWR property predicted the number of shock zone entrances – a metric which requires precise memory of shock zone boundaries – on day 2 (**Fig. 2.5G**) as well as on days 3 and 4. CA3 SG power during SWRs further predicted the distance mice travelled away from the shock zone during bouts of



movement on days 2 and 3 (**Fig. 2.5H** and **2.6H**). Mice with lower CA3 SG power during SWRs moved further from the shock zone, suggesting less precise memory of shock zone boundaries. This is consistent with the MWM results, in which SWR-associated CA3 SG power deficits in aged apoE4-KI mice are related to impairments in memory retrieval precision, particularly later in the task (**Fig. 2.2F–H** and **2.2O–Q**).

As above, we calculated a memory precision performance score for the APA task in the same manner as for the MWM task (mean for each animal across the sign reversed z-scored metrics shown in **Fig. 2.5G**, **2.5H**, and **2.6H**) and predicted memory precision performance scores using the model developed in the screen cohort. In sum, we validated relationships derived from a training set (screen cohort MWM) through application to a test set (replication cohort APA). Here again, we found that predicted score accounting for 73% of the variance in the actual score (**Fig. 2.5I**). Thus, the models developed in the screen cohort accurately predict behavioral performance, despite being derived from a different behavior and a different group of animals. We further noted that the performance scores of the MWM task predicted the performance scores of the APA task (**Fig. 2.6I** and **2.6J**). Therefore, performance on the first 3 days of MWM training predicted avoidance efficacy on day 2 of APA, while performance on probe trials during MWM predicted memory precision on day 2 of APA.

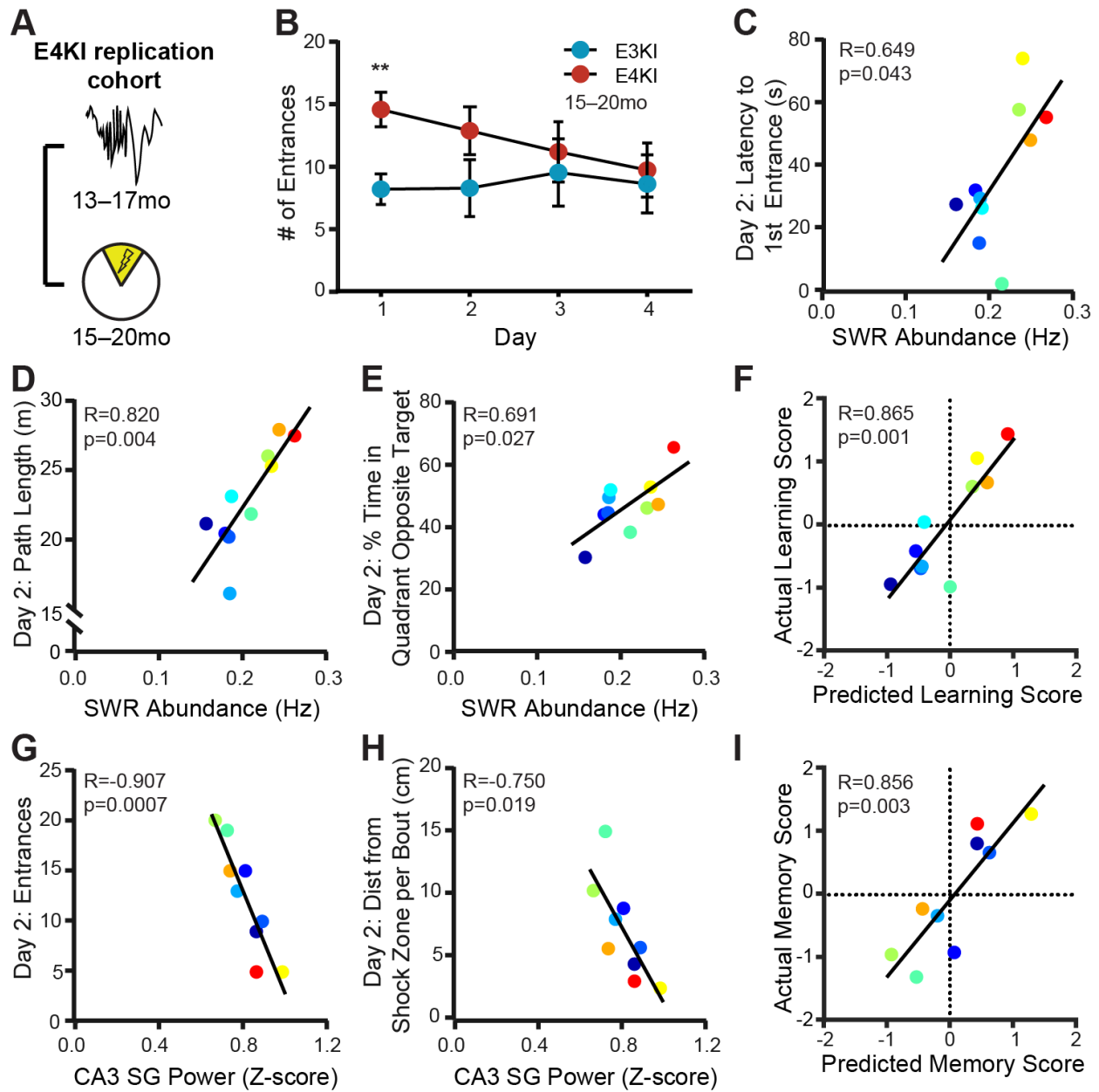


**Figure 2.5. SWR deficits predict spatial avoidance task impairments in aged apoE4-KI mice** (A) Timeline of experiments shown in B–I.

(B) Number of entrances into the shock zone is significantly different on day 1 (unpaired t test with Sidak’s multiple comparison adjustment,  $t(23) = 3.43$ ,  $p = 0.009$ ).  $n = 12$  apoE3-KI mice and  $n = 13$  apoE4-KI mice, aged 15–20 months.  $**p < 0.01$ . Error bars indicate mean  $\pm$  SEM.

(C–E) SWR abundance predicts (C) latency to first shock zone entrance ( $F(1,8) = 5.81$ , adjusted  $p = 0.12$ ), (D) total path length ( $F(1,8) = 16.42$ , adjusted  $p = 0.018$ ), and (E) percent of total time spent in quadrant opposite the shock zone ( $F(1,8) = 7.33$ , adjusted  $p = 0.1$ ) on day 2,  $n = 10$  apoE4-KI mice.

(F) Learning performance score as predicted by the linear model in 2E predicts actual learning performance ( $F(1,8) = 23.7$ ),  $n = 10$  apoE4-KI mice.

(G,H) CA3 SG power during SWRs predicts (G) entrances to the shock zone on day 2 ( $F(1,7) =$

32.53, adjusted  $p = 0.003$ ) and (H) distance travelled per movement bout relative to shock zone boundaries on day 2 ( $F(1,7) = 9.04$ , adjusted  $p = 0.077$ ),  $n = 9$  apoE4-KI mice.

(I) Memory precision performance score as predicted by the linear model in 2I predicts actual memory precision performance score ( $F(1,7) = 19.2$ ),  $n = 9$  apoE4-KI mice.

Mice aged 15–20 months at APA and 13–17 months at electrophysiological recording. Points colored in order of SWR abundance from blue (lowest) to red (highest). All correlations are Pearson correlations of apoE4-KI mice. Multiplicity adjusted  $p$  values with the Holm-Sidak method.

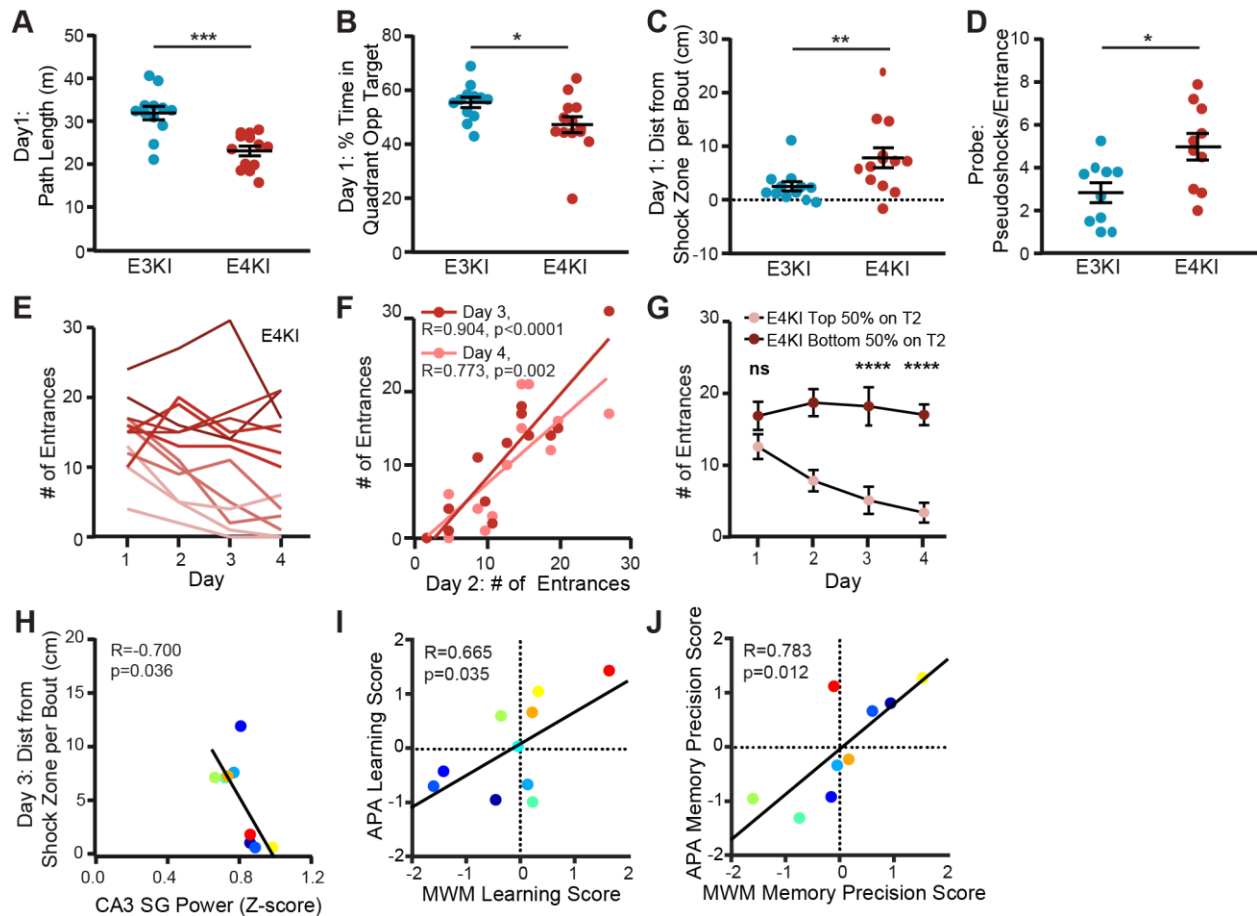


**Figure 2.6. Aged apoE4-KI mice show impaired acquisition of a spatial avoidance task.**

(A) Total path length on day 1 (unpaired t test,  $t(23) = 4.64$ ,  $p = 0.0004$ ).

(B) Percent time spent in quadrant opposite the shock zone on day 1 (unpaired t test,  $t(23) = 2.27$ ,  $p = 0.033$ ).

(C) Distance travelled during each movement bout relative to the shock zone boundary on day 1 (Mann Whitney U = 30,  $p = 0.008$ ).

(D) Shocks that would have been received per shock zone entrance during probe were the field electrified; mice which did not enter the shock zone during probe are excluded (unpaired t test,  $t(18) = 2.76$ ,  $p = 0.013$ ).

In A–D,  $n = 12$  apoE3-KI mice and  $n = 13$  apoE4-KI mice, aged 15–20 months.

(E) ApoE4-KI mice show wide variation in performance. Entrances into the shock zone curves colored from best (light) to worst (dark) average performance over all days.

(F) Number of entrances on day 2 predicts number of entrances on days 3 ( $F(1,11) = 49.27$ ) and 4 ( $F(1,11) = 16.32$ ).

(G) Number of entrances into the shock zone for apoE4-KI mice divided into 2 groups based on number of entrances on day 2. Only differences on days 1, 3, and 4 were examined, yielding no difference in day 1 ( $t(44) = 1.66$ ,  $p = 0.36$ ) and significant differences on days 3 ( $t(44) = 6.06$ ,  $p < 0.0001$ ) and 4 ( $t(44) = 5.28$ ,  $p < 0.0001$ );  $n = 7$  top 50%,  $n = 6$  bottom 50%. Unpaired t tests with Sidak’s multiple comparison adjustment.

(H) CA3 SG power during SWRs predicts distance travelled per movement bout relative to shock zone boundaries on day 3 ( $F(1,7) = 6.74$ );  $n = 9$  mice.

**(I)** MWM learning performance score predicts APA learning performance score ( $F(1,8) = 6.34$ );  $n = 10$  mice.

**(J)** MWM memory precision performance score predicts APA memory precision performance score ( $F(1,7) = 11.1$ );  $n = 9$  mice.

In E–J, apoE4-KI mice, aged 15–20 months. All correlations are Pearson correlations.

\* $p < 0.05$ , \*\* $p < 0.01$ , \*\*\* $p < 0.001$ , \*\*\*\* $p < 0.0001$ . Error bars indicate mean  $\pm$  SEM.

**Table 2.3. All APA metric correlations tested in replication cohort.**

Metric	Trial	SWR Abundance				CA3 SG Power			
		R	F	DFn, DFd	P value	R	F	DFn, DFd	P value
# of Entrances	1	-0.27	0.64	1, 8	0.45	-0.24	0.43	1, 7	0.53
	2	-0.09	0.07	1, 8	0.80	<b>-0.91</b>	<b>32.5</b>	<b>1, 7</b>	<b>0.0007</b>
	3	-0.14	0.16	1, 8	0.70	<b>-0.76</b>	<b>9.49</b>	<b>1, 7</b>	<b>0.02</b>
	4	0.19	0.29	1, 8	0.61	<b>-0.72</b>	<b>7.48</b>	<b>1, 7</b>	<b>0.03</b>
Latency to 1st Entrance	1	-0.43	1.78	1, 8	0.22	0.01	0	1, 7	0.98
	2	<b>0.65</b>	<b>5.81</b>	<b>1, 8</b>	<b>0.043</b>	0.27	0.53	1, 7	0.49
	3	0.16	0.22	1, 8	0.65	0.10	0.08	1, 7	0.79
	4	0.36	1.19	1, 8	0.31	0.37	1.12	1, 7	0.33
Path Length	1	0.14	0.15	1, 8	0.71	0.00	0	1, 7	1
	2	<b>0.82</b>	<b>16.42</b>	<b>1, 8</b>	<b>0.004</b>	-0.03	0.01	1, 7	0.93
	3	0.23	0.44	1, 8	0.52	-0.28	0.61	1, 7	0.46
	4	0.53	3.08	1, 8	0.12	-0.25	0.45	1, 7	0.53
% Time in Opposite Quadrant	1	0.22	0.39	1, 8	0.55	0.45	1.77	1, 7	0.22
	2	<b>0.69</b>	<b>7.33</b>	<b>1, 8</b>	<b>0.027</b>	0.22	0.37	1, 7	0.56
	3	-0.10	0.07	1, 8	0.79	0.13	0.12	1, 7	0.74
	4	-0.03	0.01	1, 8	0.93	0.07	0.04	1, 7	0.85
Dist from Shock Zone per Bout	1	-0.30	0.77	1, 8	0.41	-0.17	0.21	1, 7	0.66
	2	-0.08	0.05	1, 8	0.83	<b>-0.75</b>	<b>9.04</b>	<b>1, 7</b>	<b>0.02</b>
	3	0.05	0.02	1, 8	0.90	<b>-0.7</b>	<b>6.74</b>	<b>1, 7</b>	<b>0.04</b>
	4	0.38	1.31	1, 8	0.29	-0.15	0.15	1, 7	0.71

Bold values indicate significant correlations.

## **SWR deficits at younger ages predict spatial approach and spatial avoidance task impairments at older ages**

Finally, a meaningful predictor should be consistent within a single subject over aging and have predictive power before the onset of memory impairment. We conducted a longitudinal study of the replication cohort, measuring behavior and electrophysiology from the same mice at 5–8 months (young), 9–11 months (middle-aged), and 13–17 months (old) (**Fig. 2.1A, 2.7A, and Table S1**). Young apoE4-KI mice already had reduced SWR abundance and associated SG power in CA3 when compared to young apoE3-KI mice (**Fig. 2.8A and 2.8B**). Interestingly, SWR abundance increased in apoE3-KI mice over aging, although there was also a decrease in SWR baseline power (**Fig. 2.8C**) that, along with a preserved standard deviation of SWR power (**Fig. 2.8D**), could have contributed to this increase. Increases in CA3 SG power during SWRs were seen in both groups over aging (**Fig. 2.8B**) without concomitant changes in baseline or standard deviation (**Fig. 2.8E and 2.8F**), suggesting SWR-specific physiological changes and indicating stability in the quality of the recordings.

The early reduction in SWR abundance and associated SG power in CA3 did not translate into an early behavior deficit however: young apoE4-KI mice showed no detectable learning deficits (**Fig. 2.8G**)<sup>10</sup>, and SWR abundance and associated CA3 SG power measured at 5–8 months did not predict behavior tested one month later (**Table 2.4**). The lack of early memory deficits in the presence of altered network activity related to spatial navigation parallels observations in young adult human  $\epsilon 4$  carriers<sup>43</sup> and suggests the possibility of compensation in the younger brain. Overall, these findings suggest that these SWR properties, rather than degrading with age, may already show deficits at young ages that will manifest as behavioral deficits later, facilitating their potential use as an early predictor for later memory decline.

We then asked whether SWR properties were consistent within individual mice across time. More stability over time would allow these SWR properties to potentially predict memory impairments before their onset. We found that while SWR abundance was not significantly correlated across ages in either apoE3-KI or apoE4-KI mice (**Fig. 2.7B** and **2.7C**), CA3 SG power during SWRs was significantly correlated across ages in both genotypes (**Fig. 2.7D** and **2.7E**). CA3 SG power at 5–8 months did not significantly predict CA3 SG power at 13–17 months, however (e.g. for apoE3-KI mice,  $R = 0.2$ ,  $F(1,12) = 0.5$ ,  $p = 0.49$ ), indicating slow, individual-specific changes over time. We noted that baseline power in the SWR frequency band, but not in the SG frequency band, declined over aging, which could explain this lack of correlation for SWR abundance. Overall, these findings indicate that CA3 SG power during SWRs is a relatively stable measure over the timescale of four months, making it a more promising candidate for a predictive measure over aging.

Indeed, when we examined the relationship between CA3 SG power during SWRs and behavior 10–11 months later (**Fig. 2.7F**), we found strong predictive relationships (**Table 2.4**). CA3 SG power during SWRs measured at 5–8 months predicted escape latency on the third hidden day and the slope of the escape latency curve for the first 2 or first 3 days on the MWM task at 14–18 months (**Fig. 2.7G, 2.7H, 2.8H**, and **Table 2.4**). It also predicted the number of entries into the shock zone and path length on day 2 during the APA task at 15–20 months (**Fig. 2.7J, 2.7K** and **Table 2.4**). As before, points are colored by SWR abundance measured at 13–17 months from lowest (blue) to highest (red). Therefore, deficits in CA3 SG power during SWRs in young apoE4-KI mice – before spatial learning impairment is detectable – predicted future learning impairment on both a spatial approach and a spatial avoidance task at older ages. We confirmed that these effects were not expected given the multiple comparisons made: in total, we compared 15



behavioral metrics against 2 SWR properties for a total of 30 comparisons, 5 of which were significant with  $\alpha = 0.05$ ; far more than would be predicted by chance ( $p < 0.016$ , binomial test assuming all initial tests are independent; see **Table 2.4**). Even following multiple comparisons adjustment, 3 of the 5 comparisons remained significant, again far more than would be predicted by chance ( $p = 0.031$ , binomial test assuming all initial tests are independent).

Of all behavioral measures related to learning as established in Figures 2.2 and 2.5, 3 of 4 MWM metrics and 2 of 3 APA metrics were significantly predicted by CA3 SG power during SWRs measured at 5–8 months. To assess our ability to make predictions of overall behavioral performance based on the relationships in the screen cohort, we once again combined all 4 MWM metrics into a learning performance score (**Fig. 2.7I**) and all 3 APA metrics into an APA learning performance score (**Fig. 2.7L**). This allowed us to validate relationships derived from a training set (old age screen cohort SWR abundance and MWM) and apply it to a test set (young age replication cohort CA3 SG power and old age replication cohort APA and MWM). Here again, the relationship derived from the screen cohort effectively predicted behavioral deficits, allowing us to account for 50% and 71% of the variance in the actual learning performance score with CA3 SG power during SWRs measured 10–11 months previously.

We were surprised to note that the behavioral measures that could be predicted by SWR abundance measured at older ages were predicted by SWR-associated CA3 SG power measured at young ages. This suggests a relationship between CA3 SG power at 5–8 months and SWR abundance measured at 13–17 months, and indeed CA3 SG power during SWRs in young apoE4-KI mice strongly predicted SWR abundance 8 months later (**Fig. 2.8I**). This was not true for young apoE3-KI mice (**Fig. 2.8I**), again perhaps due to a ceiling effect. Therefore, in apoE4-KI mice, the amount of SG power generated in CA3 during SWRs in a young mouse predicted the extent to

which that mouse generated SWRs at rest 8 months later.

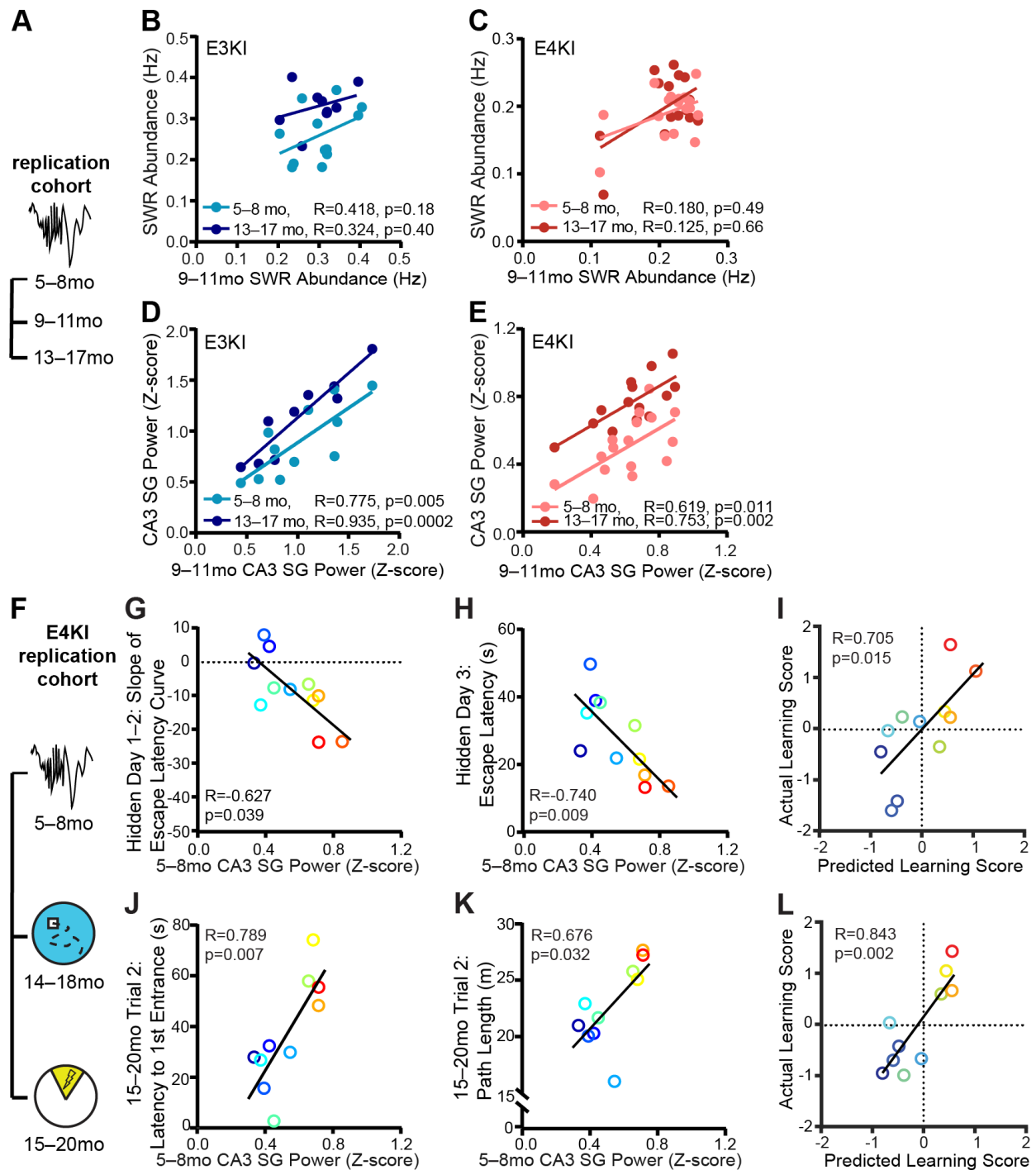


**Figure 2.7. SWR deficits at younger ages predict spatial approach and spatial avoidance task impairments at older ages**

(A) Timeline of experiments shown in B–E.

(B,C) SWR abundance at 9–11 months does not correlate with SWR abundance at 5–8 months and 13–17 months in (B) apoE3-KI mice ( $F(1,10) = 2.12$ ,  $n = 12$  for 5–8 months,  $F(1,7) = 0.82$ ,  $n = 9$  for 13–17 months) and (C) apoE4-KI mice ( $n = 17$  for 5–8 months,  $n = 15$  for 13–17 months, Spearman correlation).

**(D,E)** CA3 SG power during SWRs at 9–11 months correlates with CA3 SG power during SWRs at 5–8 months and 13–17 months in **(D)** apoE3-KI mice ( $F(1,9) = 13.54$ ,  $n = 11$  for 5–8 months,  $F(1,7) = 48.52$ ,  $n = 9$  for 13–17 months) and **(E)** apoE4-KI mice ( $F(1,14) = 8.71$ ,  $n = 16$  for 5–8 months,  $F(1,12) = 15.71$ ,  $n = 14$  for 13–17 months).

**(F)** Timeline of experiments shown in G–L.

**(G,H)** CA3 SG power during SWRs measured at 5–8 months predicts **(G)** slope of escape latency over hidden days 1–2 ( $F(1,9) = 5.82$ , adjusted  $p = 0.077$ ) and **(H)** average escape latency on hidden day 3 ( $F(1,9) = 11.08$ , adjusted  $p = 0.035$ ) on MWM task at 14–18 months,  $n = 11$  apoE4-KI mice.

**(I)** MWM learning performance score as predicted by the linear model in 2E predicts actual learning performance score ( $F(1,8) = 8.9$ ),  $n = 11$  apoE4-KI mice aged 5–8 months at electrophysiological recording and 14–18 months at MWM.

**(J,K)** CA3 SG power during SWRs also predicts **(J)** latency to first shock zone entrance ( $F(1,8) = 13.21$ , adjusted  $p = 0.033$ ) and **(K)** total path length ( $F(1,8) = 6.74$ , adjusted  $p = 0.12$ ) on APA task at 15–20 months,  $n = 10$  apoE4-KI mice.

**(L)** APA learning performance score as predicted by the linear model in 2E predicts actual learning performance score ( $F(1,8) = 19.7$ ),  $n = 10$  apoE4-KI mice aged 5–8 months at electrophysiological recording and 15–20 months at APA.

In G–L, points colored in order of 13–17 month SWR abundance from blue (lowest) to red (highest). Pearson correlations unless otherwise specified. Multiplicity adjusted  $p$  values with the Holm-Sidak method.

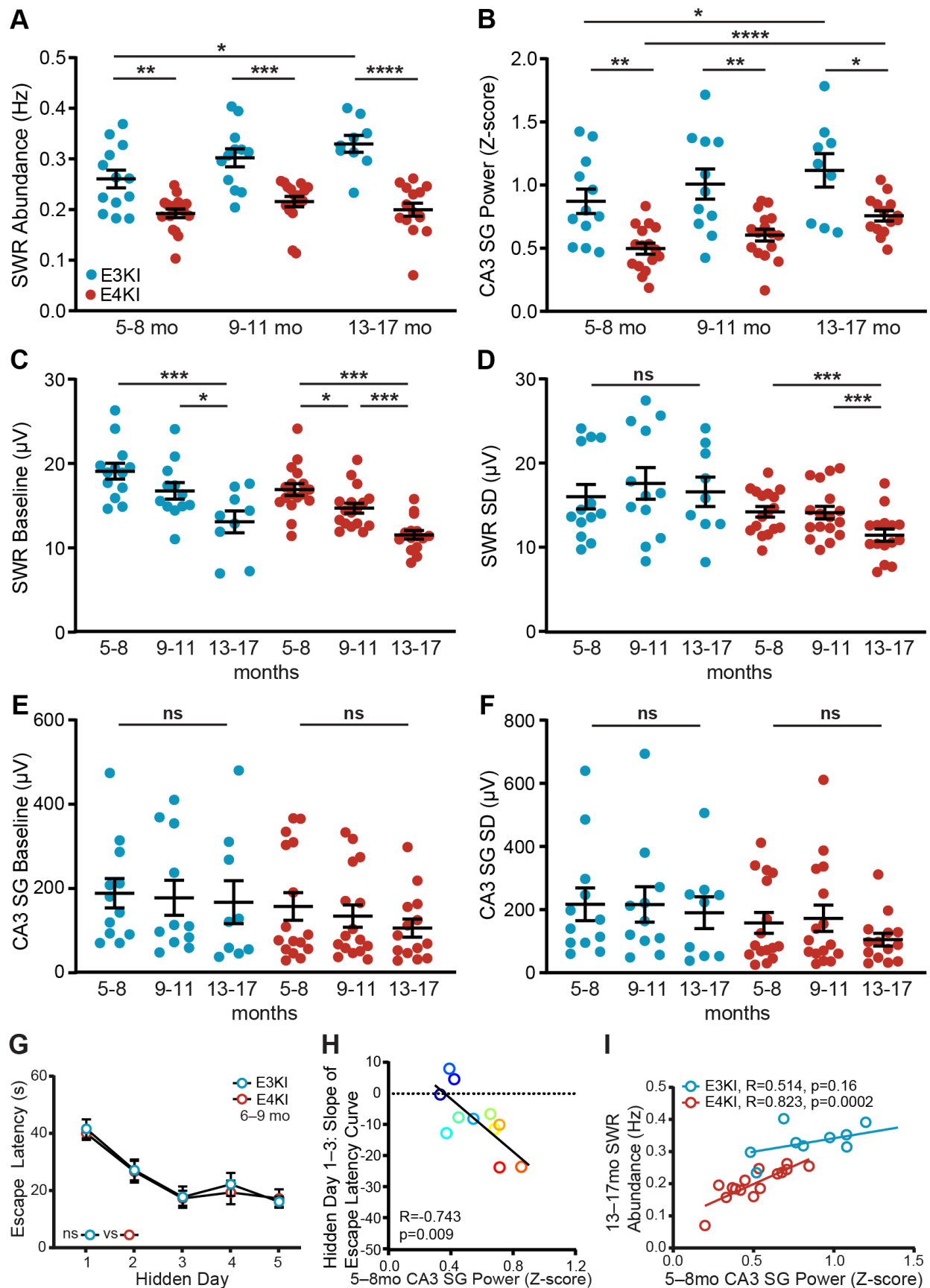


**Figure 2.8. Properties of SWRs and associated SG power in CA3 over aging in apoE3-KI and apoE4-KI mice.**

**(A)** SWR abundance of apoE3-KI mice is higher than in apoE4-KI mice across all ages. Two-way mixed-effects analysis of aligned rank transformed data shows significant effect of genotype ( $F(1,28) = 43.99$ ,  $p < 0.0001$ ) and post-hoc Mann-Whitney U test with Sidak adjustment shows significant difference at 5–8 months ( $U = 43$ ,  $p = 0.012$ ,  $n = 13$  apoE3-KI and  $n = 17$  apoE4-KI mice), 9–11 months ( $U = 26$ ,  $p = 0.0012$ ,  $n = 12$  apoE3-KI and  $n = 17$  apoE4-KI mice) and 13–17 months ( $U = 5$ ,  $p < 0.0001$ ,  $n = 9$  apoE3-KI and  $n = 15$  apoE4-KI mice). SWR abundance increases over aging in apoE3-KI mice ( $t(19) = 2.926$ ,  $p = 0.028$ ,  $n = 13$  for 5–8 months,  $n = 9$  for 13–17 months).

**(B)** CA3 SG power during SWRs in apoE3-KI mice is higher than in apoE4-KI mice across all ages. Two-way mixed-effects analysis of aligned rank transformed data shows significant effect of genotype ( $F(1,26) = 12.86$ ,  $p = 0.0014$ ) and post-hoc Mann-Whitney U test with Sidak adjustment shows significant difference at 5–8 months ( $U = 31$ ,  $p = 0.0054$ ,  $n = 12$  apoE3-KI and  $n = 16$  apoE4-KI mice), 9–11 months ( $U = 35$ ,  $p = 0.024$ ,  $n = 11$  apoE3-KI and  $n = 16$  apoE4-KI mice) and 13–17 months ( $U = 31$ ,  $p = 0.0456$ ,  $n = 9$  apoE3-KI and  $n = 14$  apoE4-KI mice). CA3 SG power during SWRs increases over aging in apoE3-KI mice ( $t(18) = 3.14$ ,  $p = 0.017$ ,  $n = 12$  for 5–8 months,  $n = 9$  for 13–17 months) and apoE4-KI mice ( $t(28) = 5.66$ ,  $p < 0.0001$ ,  $n = 16$  for 5–8 months,  $n = 14$  for 13–17 months).

**(C)** Baseline across the SWR frequency band decreases over aging in apoE3-KI mice ( $t(19) = 4.60$ ,  $p = 0.0006$ ,  $n = 13$  for 5–8 months,  $n = 9$  for 13–17 months;  $t(19) = 2.81$ ,  $p = 0.033$ ,  $n = 12$  for 9–11 months,  $n = 9$  for 13–17 months) and apoE4-KI mice ( $t(30) = 7.25$ ,  $p < 0.0001$ ,  $n = 17$  for 5–8 months,  $n = 15$  for 13–17 months;  $t(30) = 3.10$ ,  $p = 0.012$ ,  $n = 17$  for 5–8 months,  $n = 7$  for 9–11 months;  $t(30) = 4.26$ ,  $p = 0.0006$ ,  $n = 17$  for 9–11 months,  $n = 15$  for 13–17 months).

**(D)** SD across the SWR frequency band decreases over aging in apoE4-KI mice ( $t(30) = 4.34$ ,  $p = 0.0004$ ,  $n = 17$  for 5–8 months,  $n = 15$  for 13–17 months;  $t(30) = 4.18$ ,  $p = 0.0007$ ,  $n = 17$  for 9–11 months,  $n = 15$  for 13–17 months), but not apoE3-KI mice ( $t(19) = 0.25$ ,  $p = 0.99$ ,  $n = 13$  for 5–8 months,  $n = 9$  for 13–17 months).

**(E)** Baseline across SG frequency band in CA3 does not change over aging in apoE3-KI mice ( $t(18) = 0.18$ ,  $p = 1.0$ ,  $n = 12$  for 5–8 months,  $n = 9$  for 13–17 months) or apoE4-KI mice (Mann Whitney test with Sidak adjustment,  $U = 88$ ,  $p = 0.70$ ,  $n = 16$  for 5–8 months,  $n = 14$  for 13–17 months).

**(F)** SD across SG frequency band in CA3 does not change over aging in apoE3-KI mice ( $t(18) = 0.50$ ,  $p = 0.95$ ,  $n = 12$  for 5–8 months,  $n = 9$  for 13–17 months) or apoE4-KI mice (Mann Whitney U test with Sidak adjustment,  $U = 98$ ,  $p = 0.93$ ,  $n = 16$  for 5–8 months,  $n = 14$  for 13–17 months). In A–F, all comparisons unpaired t tests with Sidak adjustment unless otherwise specified.

**(G)** ApoE4-KI mice show no impairment on MWM at ages 6–9 months,  $n = 13$  apoE3-KI and  $n = 13$  apoE4-KI mice.

**(H)** CA3 SG power during SWRs measured at 5–8 months predicts slope of escape latency over hidden days 1–3 ( $F(1,9) = 10.89$  on MWM task at 14–18 months,  $n = 11$  apoE4-KI mice, Pearson correlation, Holm-Sidak multiplicity adjusted  $p = 0.027$ ).

**(I)** CA3 SG power during SWRs measured at 5–8 months predicts SWR abundance in the same mouse at 13–17 months for apoE4-KI ( $F(1,13) = 27.19$ ,  $n = 15$ ) but not apoE3-KI mice ( $F(1,7) = 2.52$ ,  $n = 9$ ), Pearson correlations.

\* $p < 0.05$ ; \*\* $p < 0.01$ ; \*\*\* $p < 0.001$ ; \*\*\*\* $p < 0.0001$ . Error bars indicate mean  $\pm$  SEM.

**Table 2.4. All behavioral correlations tested with 5–8 month apoE4-KI mouse electrophysiological data.**

Age and Behavior	Metric	SWR Abundance				CA3 SG Power			
		R	F	DFn, DFd	P value	R	F	DFn, DFd	P value
6-9 mo MWM	Slope of Escape Latency Days 1-2	0.05	0.02	1,11	0.88	0.06	0.02	1,10	0.85
	Slope of Escape Latency Days 1-3	0.17	0.33	1, 11	0.57	-0.04	0.02	1, 10	0.90
	Escape Latency Day 3	-0.03	0.01	1, 11	0.93	0.04	0.02	1, 10	0.90
	Night 1 Learning	0.22	0.55	1, 11	0.47	-0.01	0.001	1, 10	0.97
	Probe 1 % in Target Quadrant	-0.23	0.61	1, 11	0.45	-0.05	0.02	1, 10	0.88
	Probe 2 % in Target Quadrant	-0.06	0.04	1, 11	0.84	0.09	0.08	1, 10	0.79
	Probe 1 Target Crossings	-0.48	3.36	1, 11	0.09	-0.23	0.56	1, 10	0.47
	Probe 1 Dist to Platform Curve	0.27	0.88	1, 11	0.37	0.14	0.19	1, 10	0.68
	Probe 2 Dist to Platform Curve	-0.31	1.18	1, 11	0.30	-0.21	0.44	1, 10	0.52
14-18 mo MWM	Slope of Escape Latency Days 1-2	0.20	0.42	1,10	0.51	<b>-0.63</b>	<b>5.82</b>	<b>1,9</b>	<b>0.039</b>
	Slope of Escape Latency Days 1-3	-0.11	0.12	1, 10	0.74	<b>-0.74</b>	<b>10.89</b>	<b>1, 9</b>	<b>0.009</b>
	Escape Latency Day 3	0.19	0.37	1, 10	0.56	<b>-0.74</b>	<b>11.08</b>	<b>1, 9</b>	<b>0.009</b>
	Night 1 Learning	-0.16	0.27	1, 10	0.62	-0.45	2.30	1, 9	0.16
	Probe 1 % in Target Quadrant	-0.49	3.20	1, 10	0.10	-0.35	1.28	1, 9	0.29
	Probe 2 % in Target Quadrant	-0.31	1.08	1, 10	0.32	-0.07	0.05	1, 9	0.83
	Probe 1 Target Crossings	-0.43	2.21	1, 10	0.17	-0.28	0.77	1, 9	0.40
	Probe 1 Dist to Platform Curve	0.45	2.53	1, 10	0.14	0.22	0.45	1, 9	0.52
	Probe 2 Dist to Platform Curve	0.17	0.29	1, 10	0.60	0.37	1.40	1, 9	0.27
15-20 mo APA Trial 2	# of Entrances	0.60	5.09	1, 9	0.05	-0.09	0.07	1, 8	0.80
	Latency to 1 <sup>st</sup> Entrance	-0.29	0.81	1, 9	0.39	<b>0.79</b>	<b>13.21</b>	<b>1, 8</b>	<b>0.007</b>
	Path Length	0.01	0.0003	1, 9	0.99	<b>0.68</b>	<b>6.74</b>	<b>1, 8</b>	<b>0.03</b>
	% Time in Opposite Quadrant	-0.18	0.31	1, 9	0.59	0.59	4.25	1, 8	0.07
	Dist from Shock Zone per Bout	0.46	2.48	1,9	0.15	0.11	0.09	1,8	0.77
Trial 3	Dist from Shock Zone per Bout	0.43	2.02	1,9	0.19	0.20	0.33	1,8	0.58

Bold values indicate significant correlations.

## Discussion

We have demonstrated that SWR abundance and associated CA3 SG power can be used as functional biomarkers to predict cognitive decline in an apoE4 mouse model of AD. We capitalized on the behavioral population variability and the SWR-related network alterations found in apoE4-KI mice, which allowed us to assess correlations between the two. We then observed that these SWR properties, measured 1–2 months prior to behavior in aged apoE4-KI mice, predict multiple behavioral metrics, capturing different but related aspects of spatial learning and memory. These findings were not restricted to a single cohort, as demonstrated through replication, or to a single task, as demonstrated through correlations observed with two distinct spatial tasks. Finally and most critically, CA3 SG power during SWRs in young apoE4-KI mice, measured prior to the onset of detectable cognitive deficits, predicted spatial learning and memory impairments across both tasks 10 months later. This metric was also correlated within individual animals over several months, making it a potential functional biomarker for cognitive decline in AD (**Fig. 2.9**).



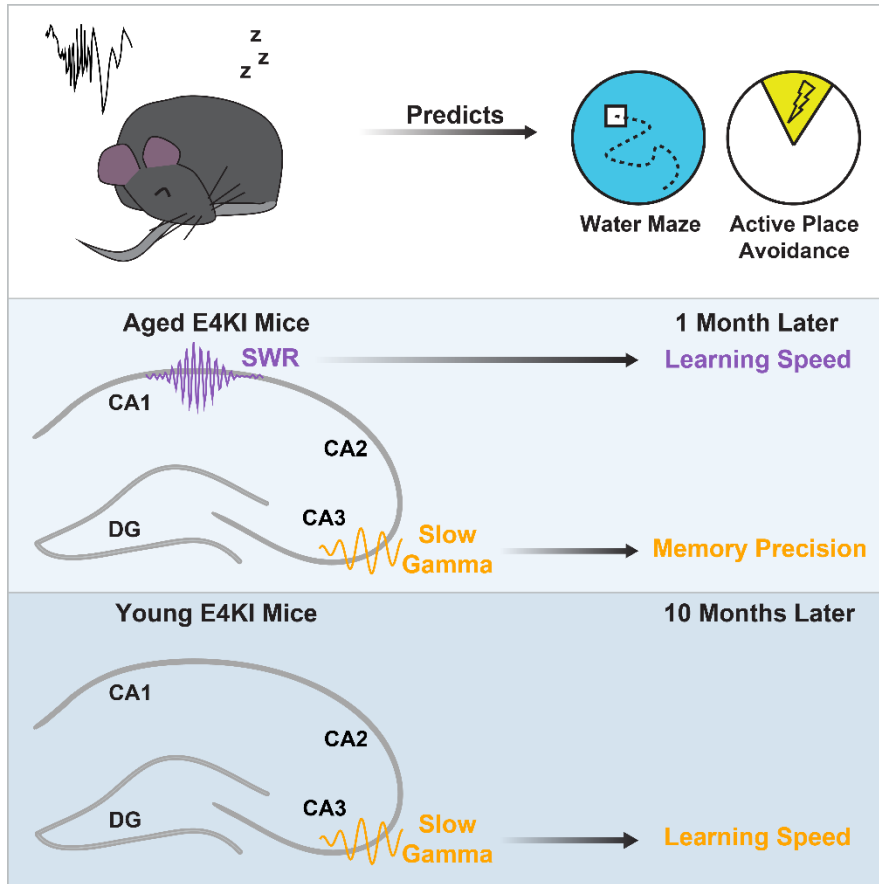


**Figure 2.9. SWRs and associated SG power in SG as a proposed biomarker.**

We observed full replication of all predictive measures despite differences in SWR abundance between the screen and replication cohorts. While experimental conditions were identical to the greatest practical extent, it is possible that genetic drift occurred across multiple generations or that colony conditions changed, which could affect this result. Despite this, when we z-score normalized the data, we found that predictive relationships derived from the initial screen cohort were very strongly predictive in the replication cohort for both the MWM and the APA tasks. This consistency suggests that a simple normalization to the values seen in a given population allows for accurate predictions of behavioral impairments from physiological measurements across many months in our mouse models.

Through chronic measurement of hippocampal network activity in individual mice, we were able to assess whether SWR features are stable over several months. SWR abundance is affected by environmental variables such as novelty and reward<sup>31,32</sup>, but such a relationship has yet to be defined for SWR-associated slow gamma. Our results suggest that over timescales of 4 months, CA3 SG power during SWRs in each animal is significantly correlated with the same measure in the same animal assessed at a later time point, while SWR abundance is not, perhaps due to changes in baseline activity in the SWR frequency band over aging. Previous cross-sectional work in wild type rats reported that SWR abundance measured during or immediately after a task was reduced in aged rats<sup>44,45</sup>. Our longitudinal measurements in human apoE3-KI mice during rest, independent from task performance, did not show this reduction. Rather, we observed that both SWR abundance and associated CA3 SG power slightly increased with aging, although average measures for apoE4-KI mice remained lower than for apoE3-KI mice across all ages. Since behavioral differences do not emerge until later ages, this suggests an additional network change – perhaps a loss of compensation – that occurs over aging in apoE4-KI mice, which interacts with

existing physiological deficits to cause behavioral impairment.

Substantial previous work has shown that physiological characteristics of CA3 can distinguish between aged rats with impaired or unimpaired memory. Aged impaired rats have elevated CA3 activation, which leads to inability to remap CA3 place cells in novel contexts<sup>46,47</sup>. They furthermore have reduced expression of genes related to synaptic plasticity in CA3<sup>48-51</sup>. Our findings establish another way in which measurements from CA3 can distinguish impaired from unimpaired spatial memory. Moreover, SG activity throughout the hippocampus is hypothesized to originate from CA3. During SWRs, CA1 SG is most coherent with CA3 SG activity, and SG power is highest in the stratum radiatum, the input layer from CA3<sup>28,36,52</sup>. Thus, it is reasonable that SG power measured at its hypothesized generator is the strongest predictor of spatial learning and memory.

The extent of coherence between CA1 and CA3 of oscillations in the SG frequency band correlates with replay fidelity, the temporal order of place cell firing in a spatial sequence<sup>36</sup>. Notably, one previous study found that measures of replay fidelity following a linear track run correlated with MWM learning in aged wild type rats<sup>53</sup>. Together with our finding of correlations between CA3 SG power during SWRs and MWM performance, this suggests that measures related to replay fidelity measured outside of task performance can predict MWM learning deficits in the context of both normal aging and AD aging.

We additionally found that CA3 slow gamma power during SWRs at young ages predicts SWR abundance 8 months later. While the cause of this correlation is unclear, it suggests a relationship in apoE4-KI mice between organization of replay events in early adulthood and the number of events later in life. There may be a positive feedback loop in which replays with greater fidelity to the original encoded sequences lead to greater probability of future replays over aging.

Alternatively, CA3 SG power during SWRs may be a more sensitive reflection of the health of the underlying circuitry, which may affect SWR generation in later life.

The most common proposed biomarkers for AD are amyloid or tau, measured in CSF or by PET imaging<sup>54</sup>. However, at least 40% of cognitively normal elderly patients show amyloid or tau pathology, indicating that these molecular biomarkers are not sufficient to distinguish healthy aging from AD-induced cognitive decline<sup>55,56</sup>. Hippocampal network activity shows a clear link between pathology and behavioral outcomes and represents a potential new class of functional biomarkers. Moreover, human longitudinal studies of potential biomarkers have only been able to follow sporadic AD subjects for 3–8 years prior to diagnosis. Since cognitive decline accelerates 15-fold during the 5–6 years prior to AD diagnosis, these biomarkers may only be sufficient to predict ongoing cognitive decline<sup>57</sup>. In contrast, this study in mice was able to predict cognitive decline long before memory impairment was detectable.

A physiological biomarker also has the distinct advantage of being compatible with repeated measures. In contrast, behavioral readouts often cannot be repeated without affecting performance, and post-mortem pathology only captures the final endpoint. Using a network signature, disease progression could be measured over aging, and cellular pathological differences that differentiate future impaired from unimpaired animals could be assessed at an early age. During preclinical drug studies, a single animal could be measured over a time course of treatment or with variable doses, both reducing the number of animals required and increasing study power through use of paired statistics. Most critically, preventative therapies could be tested in animals by measuring the effect on the hippocampal network before spatial learning and memory impairments arise.

Currently, SWRs are only detectable in humans by depth electrodes<sup>58</sup>, thus new technology

will need to be developed to translate this functional biomarker into humans. However, SWRs are signatures of a brain-wide activity patterns<sup>27</sup>, and could in principle be detected via EEG or other non-invasive approaches. In particular, MEG has recently been demonstrated to be capable of detecting ripple frequency oscillations in deep brain structures<sup>59</sup> and the hippocampus<sup>60</sup>, and high density scalp EEG has been shown to detect signals highly correlated to those measured by intracranial electrodes in deep brain structures<sup>61</sup>. Moreover, recent work in humans shows that SWRs detected in the medial temporal lobe are highly correlated with SWRs detected in the temporal association cortices, suggesting that detecting SWRs from cortex could serve as a proxy<sup>62</sup>. Overall, SWR features are compelling functional biomarker candidates that can predict future cognitive decline in an apoE4 model of AD and could potentially be used to predict AD risk and assess treatment efficacy before the onset of symptoms.

## References

1. Hebert, L. E., Weuve, J., Scherr, P. A. & Evans, D. A. Alzheimer disease in the United States (2010-2050) estimated using the 2010 census. *Neurology* **80**, 1778–1783 (2013).
2. Sperling, R. A., Aisen, P. S., Beckett, L. A., Bennett, D. A., Craft, S., Fagan, A. M., Iwatsubo, T., Jack, C. R., Kaye, J., Montine, T. J., Park, D. C., Reiman, E. M., Rowe, C. C., Siemers, E., Stern, Y., Yaffe, K., Carrillo, M. C., Thies, B., Morrison-Bogorad, M., Wagster, M. V & Phelps, C. H. Toward defining the preclinical stages of Alzheimer's disease: recommendations from the National Institute on Aging-Alzheimer's Association workgroups on diagnostic guidelines for Alzheimer's disease. *Alzheimers. Dement.* **7**, 280–92 (2011).
3. Ballard, C., Gauthier, S., Corbett, A., Brayne, C., Aarsland, D. & Jones, E. Alzheimer's disease. *Lancet* **377**, 1019–1031 (2011).
4. Huang, Y. & Mucke, L. Alzheimer mechanisms and therapeutic strategies. *Cell* **148**, 1204–1222 (2012).
5. Liu, C.-C., Liu, C.-C., Kanekiyo, T., Xu, H. & Bu, G. Apolipoprotein E and Alzheimer disease: risk, mechanisms and therapy. *Nat. Rev. Neurol.* **9**, 106–18 (2013).
6. Farrer, L. A., Cupples, L. A., Haines, J. L., Hyman, B. T., Kukull, W. A., Mayeux, R., Myers, R. H., Pericak-Vance, M. A., Risch, N. & van Duijn, C. M. Effects of age, sex, and ethnicity on the association between apolipoprotein E genotype and Alzheimer disease. A meta-analysis. APOE and Alzheimer Disease Meta Analysis Consortium. *JAMA* **278**, 1349–1356 (1997).
7. Corder, E. H., Saunders, A. M., Strittmatter, W. J., Schmechel, D. E., Gaskell, P. C., Small, G. W., Roses, A. D., Haines, J. L. & Pericak-Vance, M. A. Gene dose of

- apolipoprotein E type 4 allele and the risk of Alzheimer's disease in late onset families. *Science* **261**, 921–923 (1993).
8. Bien-Ly, N., Gillespie, A. K., Walker, D., Yoon, S. Y. & Huang, Y. Reducing human apolipoprotein E levels attenuates age-dependent A $\beta$  accumulation in mutant human amyloid precursor protein transgenic mice. *J. Neurosci.* **32**, 4803–11 (2012).
  9. Ramaswamy, G., Xu, Q., Huang, Y. & Weisgraber, K. H. Effect of Domain Interaction on Apolipoprotein E Levels in Mouse Brain. *J. Neurosci.* **25**, 10658–10663 (2005).
  10. Leung, L., Andrews-Zwilling, Y., Yoon, S. Y., Jain, S., Ring, K., Dai, J., Wang, M. M., Tong, L., Walker, D. & Huang, Y. Apolipoprotein E4 causes age- and sex-dependent impairments of hilar GABAergic interneurons and learning and memory deficits in mice. *PLoS One* **7**, e53569 (2012).
  11. Andrews-Zwilling, Y., Bien-Ly, N., Xu, Q., Li, G., Bernardo, A., Yoon, S. Y., Zwilling, D., Yan, T. X., Chen, L. & Huang, Y. Apolipoprotein E4 causes age- and Tau-dependent impairment of GABAergic interneurons, leading to learning and memory deficits in mice. *J Neurosci* **30**, 13707–13717 (2010).
  12. Beydoun, M. A., Boueiz, A., Abougergi, M. S., Kitner-Triolo, M. H., Beydoun, H. A., Resnick, S. M., O'Brien, R. & Zonderman, A. B. Sex differences in the association of the apolipoprotein E epsilon 4 allele with incidence of dementia, cognitive impairment, and decline. *Neurobiol. Aging* **33**, 720–731 (2012).
  13. Caselli, R. J., Dueck, A. C., Osborne, D., Sabbagh, M. N., Connor, D. J., Ahern, G. L., Baxter, L. C., Rapcsak, S. Z., Shi, J., Woodruff, B. K., Locke, D. E. C., Snyder, C. H., Alexander, G. E., Rademakers, R. & Reiman, E. M. Longitudinal Modeling of Age-Related Memory Decline and the APOE  $\epsilon$ 4 Effect. *N. Engl. J. Med.* **361**, 255–263 (2009).

14. deIpolyi, A. R., Rankin, K. P., Mucke, L., Miller, B. L. & Gorno-Tempini, M. L. Spatial cognition and the human navigation network in AD and MCI. *Neurology* **69**, 986–97 (2007).
15. Mattson, M. P. Pathways towards and away from Alzheimer’s disease. *Nature* **430**, 631–639 (2004).
16. Morris, R. G. & Baddeley, A. D. Primary and working memory functioning in Alzheimer-type dementia. *J. Clin. Exp. Neuropsychol.* **10**, 279–96 (1988).
17. Squire, L. R. & Zola-Morgan, J. T. The cognitive neuroscience of human memory since H.M. *Annu Rev Neurosci* **34**, 259–288 (2011).
18. Buzsáki, G. Hippocampal sharp wave-ripple: A cognitive biomarker for episodic memory and planning. *Hippocampus* **1188**, 1073–1188 (2015).
19. Palop, J. J., Chin, J. & Mucke, L. A network dysfunction perspective on neurodegenerative diseases. *Nature* **443**, 768–773 (2006).
20. Goutagny, R. & Krantic, S. Hippocampal oscillatory activity in Alzheimer’s disease: toward the identification of early biomarkers? *Aging Dis.* **4**, 134–40 (2013).
21. Buzsáki, G. Hippocampal sharp waves: their origin and significance. *Brain Res.* **398**, 242–52 (1986).
22. Joo, H. R. & Frank, L. M. The hippocampal sharp wave–ripple in memory retrieval for immediate use and consolidation. *Nat. Rev. Neurosci.* **19**, 744–757 (2018).
23. Girardeau, G., Benchenane, K., Wiener, S. I., Buzsáki, G. & Zugaro, M. B. Selective suppression of hippocampal ripples impairs spatial memory. *Nat. Neurosci.* **12**, 1222–1223 (2009).
24. Ego-Stengel, V. & Wilson, M. A. Disruption of ripple-associated hippocampal activity



- during rest impairs spatial learning in the rat. *Hippocampus* **20**, 1–10 (2010).
25. Jadhav, S. P., Kemere, C., German, P. W. & Frank, L. M. Awake Hippocampal Sharp-Wave Ripples Support Spatial Memory. *Science* **336**, 1454–1458 (2012).
  26. Nokia, M. S., Mikkonen, J. E., Penttonen, M. & Wikgren, J. Disrupting neural activity related to awake-state sharp wave-ripple complexes prevents hippocampal learning. *Front. Behav. Neurosci.* **6**, eCollection 2012 (2012).
  27. Logothetis, N. K., Eschenko, O., Murayama, Y., Augath, M., Steudel, T., Evrard, H. C., Besserve, M. & Oeltermann, A. Hippocampal-cortical interaction during periods of subcortical silence. *Nature* **491**, 547–53 (2012).
  28. Gillespie, A. K., Jones, E. A., Lin, Y.-H., Karlsson, M. P., Kay, K., Yoon, S. Y., Tong, L. M., Nova, P., Carr, J. S., Frank, L. M. & Huang, Y. Apolipoprotein E4 causes age-dependent disruption of slow gamma oscillations during hippocampal sharp-wave ripples. *Neuron* **90**, 740–751 (2016).
  29. Ciupek, S. M., Cheng, J., Ali, Y. O., Lu, H.-C. & Ji, D. Progressive Functional Impairments of Hippocampal Neurons in a Tauopathy Mouse Model. *J. Neurosci.* **35**, 8118–8131 (2015).
  30. Nicole, O., Hadzibegovic, S., Gajda, J., Bontempi, B., Bem, T. & Meyrand, P. Soluble amyloid beta oligomers block the learning-induced increase in hippocampal sharp wave-ripple rate and impair spatial memory formation. *Sci. Rep.* **6**, 22728 (2016).
  31. Cheng, S. & Frank, L. M. New experiences enhance coordinated neural activity in the hippocampus. *Neuron* **57**, 303–13 (2008).
  32. Singer, A. C. & Frank, L. M. Rewarded outcomes enhance reactivation of experience in the hippocampus. *Neuron* **64**, 910–21 (2009).

33. O'Neill, J., Senior, T. J., Allen, K., Huxter, J. R. & Csicsvari, J. Reactivation of experience-dependent cell assembly patterns in the hippocampus. *Nat. Neurosci.* **11**, 209–215 (2008).
34. Iaccarino, H. F., Singer, A. C., Martorell, A. J., Rudenko, A., Gao, F., Gillingham, T. Z., Mathys, H., Seo, J., Kritskiy, O., Abdurrob, F., Adaikkan, C., Canter, R. G., Rueda, R., Brown, E. N., Boyden, E. S. & Tsai, L.-H. Gamma frequency entrainment attenuates amyloid load and modifies microglia. *Nature* **540**, 230–235 (2016).
35. Oliva, A., Fernández-Ruiz, A., Fermino de Oliveira, E. & Buzsáki, G. Origin of Gamma Frequency Power during Hippocampal Sharp-Wave Ripples. *Cell Rep.* **25**, 1693–1700 (2018).
36. Carr, M. F., Karlsson, M. P. & Frank, L. M. Transient Slow Gamma Synchrony Underlies Hippocampal Memory Replay. *Neuron* **75**, 700–713 (2012).
37. Ramirez-Villegas, J. F., Logothetis, N. K. & Besserve, M. Diversity of sharp-wave-ripple LFP signatures reveals differentiated brain-wide dynamical events. *Proc. Natl. Acad. Sci.* **112**, E6379–E6387 (2015).
38. Pfeiffer, B. E. & Foster, D. J. Autoassociative dynamics in the generation of sequences of hippocampal place cells. *Science* **349**, 180–183 (2015).
39. Morris, R. G. Developments of a water-maze procedure for studying spatial learning in the rat. *J. Neurosci. Methods* **11**, 47–60 (1984).
40. Cimadevilla, J. M., Kaminsky, Y., Fenton, A. A. & Bures, J. Passive and active place avoidance as a tool of spatial memory research in rats. *J. Neurosci. Methods* **102**, 155–164 (2000).
41. Sullivan, P. M., Mace, B. E., Maeda, N. & Schmechel, D. E. Marked regional differences

- of brain human apolipoprotein E expression in targeted replacement mice. *Neuroscience* **124**, 725–733 (2004).
42. Wobbrock, J. O., Findlater, L., Gergle, D. & Higgins, J. J. The aligned rank transform for nonparametric factorial analyses using only anova procedures. in *Proc. 2011 Annu. Conf. Hum. factors Comput. Syst. - CHI '11* 143–6 (2011). doi:10.1145/1978942.1978963
43. Kunz, L., Schröder, T. N., Lee, H., Montag, C., Lachmann, B., Sariyska, R., Reuter, M., Stirnberg, R., Stöcker, T., Messing-Floeter, P. C., Fell, J., Doeller, C. F., Axmacher, N., Schroder, T. N., Lee, H., Montag, C., Lachmann, B., Sariyska, R., Reuter, M., Stirnberg, R., Stocker, T., Messing-Floeter, P. C., Fell, J., Doeller, C. F. & Axmacher, N. Reduced grid-cell-like representations in adults at genetic risk for Alzheimer's disease. *Science* **350**, 430–433 (2015).
44. Cowen, S. L., Gray, D. T., Wiegand, J.-P. P. L., Schimanski, L. A. & Barnes, C. A. Age-associated changes in waking hippocampal sharp-wave ripples. *Hippocampus* Epub ahead of print (2018). doi:10.1002/hipo.23005
45. Wiegand, J.-P. L., Gray, D. T., Schimanski, L. A., Lipa, P., Barnes, C. A. & Cowen, S. L. Age Is Associated with Reduced Sharp-Wave Ripple Frequency and Altered Patterns of Neuronal Variability. *J. Neurosci.* **36**, 5650–60 (2016).
46. Wilson, I. A., Ikonen, S., Gallagher, M., Eichenbaum, H. & Tanila, H. Age-Associated Alterations of Hippocampal Place Cells Are Subregion Specific. *J. Neurosci.* **25**, 6877–6886 (2005).
47. Haberman, R. P., Koh, M. T. & Gallagher, M. Heightened cortical excitability in aged rodents with memory impairment. *Neurobiol. Aging* **54**, 144–151 (2017).
48. Adams, M. M., Smith, T. D., Moga, D., Gallagher, M., Wang, Y., Wolfe, B. B., Rapp, P.

- R. & Morrison, J. H. Hippocampal dependent learning ability correlates with N-methyl-D-aspartate (NMDA) receptor levels in CA3 neurons of young and aged rats. *J. Comp. Neurol.* **432**, 230–243 (2001).
49. Smith, T. D., Adams, M. M., Gallagher, M., Morrison, J. H. & Rapp, P. R. Circuit-specific alterations in hippocampal synaptophysin immunoreactivity predict spatial learning impairment in aged rats. *J. Neurosci.* **20**, 6587–93 (2000).
50. Haberman, R. P., Colantuoni, C., Koh, M. T. & Gallagher, M. Behaviorally Activated mRNA Expression Profiles Produce Signatures of Learning and Enhanced Inhibition in Aged Rats with Preserved Memory. *PLoS One* **8**, e83674 (2013).
51. Haberman, R. P., Colantuoni, C., Stocker, A. M., Schmidt, A. C., Pedersen, J. T. & Gallagher, M. Prominent hippocampal CA3 gene expression profile in neurocognitive aging. *Neurobiol. Aging* **32**, 1678–1692 (2011).
52. Ramirez-Villegas, J. F., Willeke, K. F., Logothetis, N. K. & Besserve, M. Dissecting the Synapse- and Frequency-Dependent Network Mechanisms of In Vivo Hippocampal Sharp Wave-Ripples. *Neuron* **100**, 1224-1240.e13 (2018).
53. Gerrard, J. L., Burke, S. N., McNaughton, B. L. & Barnes, C. A. Sequence reactivation in the hippocampus is impaired in aged rats. *J. Neurosci.* **28**, 7883–90 (2008).
54. Riedel, W. J. Preventing cognitive decline in preclinical Alzheimer's disease. *Curr. Opin. Pharmacol.* **14**, 18–22 (2014).
55. Caselli, R. J. & Reiman, E. M. Characterizing the preclinical stages of Alzheimer's disease and the prospect of presymptomatic intervention. *J. Alzheimers. Dis.* **33 Suppl 1**, S405-16 (2013).
56. Boyle, P. A., Yu, L., Wilson, R. S., Schneider, J. A. & Bennett, D. A. Relation of

- neuropathology with cognitive decline among older persons without dementia. *Front. Aging Neurosci.* **5**, 50 (2013).
57. Wilson, R. S., Leurgans, S. E., Boyle, P. A. & Bennett, D. A. Cognitive Decline in Prodromal Alzheimer Disease and Mild Cognitive Impairment. *Arch. Neurol.* **68**, 351–356 (2011).
  58. Axmacher, N., Elger, C. E. & Fell, J. Ripples in the medial temporal lobe are relevant for human memory consolidation. *Brain* **131**, 1806–17 (2008).
  59. Yin, C., Zhang, X., Chen, Z., Li, X., Wu, S., Lv, P. & Wang, Y. Detection and localization of interictal ripples with magnetoencephalography in the presurgical evaluation of drug-resistant insular epilepsy. *Brain Res.* **1706**, 147–156 (2019).
  60. Liu, Y., Dolan, R. J., Kurth-Nelson, Z. & Behrens, T. E. J. Human Replay Spontaneously Reorganizes Experience. *Cell* **178**, 1–13 (2019).
  61. Seeber, M., Cantonas, L.-M., Hoevels, M., Sesia, T., Visser-Vandewalle, V. & Michel, C. M. Subcortical electrophysiological activity is detectable with high-density EEG source imaging. *Nat. Commun.* **10**, 753 (2019).
  62. Vaz, A. P., Inati, S. K., Brunel, N. & Zaghoul, K. A. Coupled ripple oscillations between the medial temporal lobe and neocortex retrieve human memory. *Science* **363**, 975–978 (2019).

## **CHAPTER III**

### **Hippocampal GABAergic Interneurons Bidirectionally Modulate Sharp-Wave Ripples**

## **Abstract**

The hippocampus transitions smoothly between encoding of new memories, driven by external inputs from entorhinal cortex and manifest as fast gamma oscillatory activity, and consolidation of old memories, driven by internal inputs from CA3 and manifest as slow gamma (SG) and sharp-wave ripple (SWR) oscillatory activity. However, the mechanism for this transition between inputs is unclear. We hypothesized that GABAergic interneurons in CA3 and DG might modulate this transition. The majority of hippocampal interneurons can be classified as parvalbumin-expressing ( $PV^+$ ), soma-targeting or somatostatin-expressing ( $SST^+$ ), dendritic-targeting subtypes that differentially regulate endogenous firing patterns and which contribute to SWRs in CA1. SWRs are driven by inputs from upstream area CA3 and also engage the dentate gyrus (DG), but little is known about whether and how these interneuron subtypes in either CA3 or DG regulate activity in CA1. We therefore carried out chemogenetic inhibition of either or both of these interneuron subtypes in CA3 and DG to understand their role in regulating SWRs as a measure of CA3 coupling to CA1. We found that that  $PV^+$  and  $SST^+$  interneurons bidirectionally modulate sleep SWRs in CA1 and coincident activity throughout the hippocampus. Suppressing  $PV^+$  interneurons leads to increased coupling of CA3 to CA1, while suppressing  $SST^+$  interneurons has the opposite effect. Suppressing both interneuron types simultaneously follows the same trends as inhibiting  $PV^+$  interneurons alone, suggesting somatic inhibition dominates these effects. Thus, CA3 and DG  $PV^+$  and  $SST^+$  interneurons may modulate the transition between internal and external inputs to the hippocampus.

## Introduction

Many regions of the brain play multiple roles in information processing and facilitate this by switching between different input and output transformations. The hippocampus, for instance, contributes to encoding, retrieval, and consolidation of memories, and must alternate between three distinct network states in order to do so<sup>1-3</sup>. Encoding of new information is driven by external inputs from the entorhinal cortex (EC). Consolidation of previous information is driven by internal inputs from the CA3. Retrieval may be a combination of these two input sources<sup>4</sup>.

One major driver of this transition is locomotion. CA3 input to CA1 is highest during immobility, while EC input to CA1 is highest during movement<sup>5-7</sup>. During immobility, high CA3 drive to CA1 manifests as sharp-wave ripples (SWRs)<sup>8-10</sup> which are critical for memory consolidation following learning<sup>11-13</sup>. Underlying SWRs are neuronal sequences which replay trajectories associated with past experiences<sup>14-16</sup> for consolidation in cortical areas<sup>17-20</sup>. During movement, high EC drive to CA1 manifests as fast gamma oscillations nested within theta oscillations<sup>21,22</sup> during which new locations are encoded<sup>23</sup>. However, this behavioral transition is insufficient to explain the network transition, as encoding of current locations can occur during immobility<sup>24</sup> and retrieval of task-relevant trajectories via SWRs can occur during movement<sup>25-27</sup>.

What facilitates this switch between internal and external inputs? GABAergic interneurons regulate principal cell input and output and might therefore contribute to this transition. In the hippocampus, the majority of GABAergic interneurons are somatostatin-expressing (SST<sup>+</sup>), or parvalbumin-expressing (PV<sup>+</sup>)<sup>28,29</sup>. PV<sup>+</sup> and SST<sup>+</sup> interneurons are distinguished by their subcellular spatial domains, firing properties, pyramidal cell spike modulation mechanisms, and temporal coordination<sup>30</sup>. PV is expressed mainly by basket and axo-axonic cells while SST is expressed mainly by oriens-lacunosum moleculare (O-LM), hilar perforant path (HIPP), and



bistratified cells<sup>30</sup>. In CA1, multiple studies have demonstrated SST<sup>+</sup> O-LM and bistratified and PV<sup>+</sup> basket and axo-axonic cells entrain their firing to ripple frequency oscillations<sup>31–35</sup>. However, SWRs are driven by CA3 and further engage DG<sup>9,36</sup>. While a few studies have examined PV<sup>+</sup> and SST<sup>+</sup> interneurons in CA3 and the dentate gyrus (DG) during SWRs and found them to also increase their firing<sup>37,38</sup>, their role in modulating SWRs is unknown.

PV<sup>+</sup> and SST<sup>+</sup> interneurons are uniquely positioned to bidirectionally regulate information flow. PV<sup>+</sup> interneurons mainly target somatic and perisomatic compartments and thus regulate principal cell excitability and precise spike timing<sup>30,34,39,40</sup>. These cells are preferentially recruited by EC layer II inputs and are thus the main drivers of feedforward inhibition<sup>41–43</sup>. In contrast, SST<sup>+</sup> interneurons mainly target distal apical dendrites – the layer of extrahippocampal excitatory inputs from EC and MS – and thus gate synaptic weights and the extent of principal cell spiking<sup>30,40,44,45</sup>. These cells receive primarily local inputs and thus provide feedback inhibition<sup>41,42</sup>. Overall, potentiation of CA1 SST<sup>+</sup> interneurons attenuates EC inputs to CA1 while potentiation of PV<sup>+</sup> interneurons attenuates CA3 inputs to CA1<sup>46,47</sup>.

We therefore predicted that reducing CA3 and DG PV<sup>+</sup> inhibition would increase CA3 excitability and reduce feedforward inhibition from EC, while reducing SST<sup>+</sup> inhibition would ungate EC inputs. To test this, we measured the effect of suppressing CA3 and DG PV<sup>+</sup> and SST<sup>+</sup> interneurons on SWRs during sleep and awake rest. We observed that suppressing PV<sup>+</sup> interneurons increased CA3 coupling to CA1, possibly at the expense of EC input, while suppressing SST<sup>+</sup> interneurons decreased CA3 coupling to CA1, possibly through increasing EC input. Our findings support PV<sup>+</sup> and SST<sup>+</sup> interneurons in

## Materials and Methods

### EXPERIMENTAL MODEL AND SUBJECT DETAILS

C57BL6/J mice with the SST-IRES-Cre allele (*Sst<sup>tm2.1(cre)Zjh</sup>/J*, MGI:4838416) or the PV-IRES-Cre allele (*Pvalb<sup>tm1(cre)Arbr</sup>/J*, MGI:3590684) knocked-in<sup>48,49</sup> were originally obtained from Jackson Laboratory. Equal numbers of PVCre, SSTCre and PVCre/SSTCre mice were selected from littermates of a PVCre x SSTCre cross. All animals were bred in-house using trio breeding producing 10 pups per litter on average, which were weaned at 28 days. Equal proportions of males and females aged 3–8 months were selected for each genotype, viral vector, and group. Within each genotype group and sex, mice were randomly assigned to receive either hM4Di-mCherry vector or mCherry empty vector injection. Experimenters were blinded to genotype during surgery and blinded to genotype and viral vector expression during all post-operative behavior, recordings, and histology. Animals were housed in a pathogen-free barrier facility on a 12h light cycle (lights on at 7am and off at 7pm) at 19–23°C and 30–70% humidity. Animals were identified by ear punch under brief isoflurane anesthesia and genotyped by PCR of a tail clipping at both weaning and perfusion. All animals otherwise received no procedures except those reported in this study. Throughout the study, mice were singly housed. All animal experiments were conducted in accordance with the guidelines and regulations of the National Institutes of Health, the University of California, and the Gladstone Institutes under IACUC protocol AN117112.

### METHOD DETAILS

#### Surgery

Mice were anesthetized by intraperitoneal injection of ketamine (60 mg/kg) and xylazine (30 mg/kg); anesthesia was maintained with 0.6–1.5% isoflurane given through a vaporizer and nose

cone. The head was secured with earbars and a tooth bar in a stereotaxic alignment system (Kopf Instruments). Fur was removed from the scalp, which was then sterilized with alternating swabs of chlorhexidine and 70% ethanol. The scalp was opened, sterilized with 3% hydrogen peroxide, and thoroughly cleaned to reduce risk of tissue regrowth. 0.5 mm craniotomies were made at 1.95 mm AP and  $\pm$  1.5 mm ML from bregma for viral injection. 1  $\mu$ L of AAV5-hSyn-DIO-hM4D(Gi)-mCherry (UNC Viral Vector Core;<sup>50</sup>) or AAV5-hSyn-DIO-mCherry (Addgene, RRID: Addgene\_50459) was injected at 2.1 mm below the surface of the brain<sup>51,52</sup>. Skull screws (FST) were inserted into craniotomies over the right frontal cortex and left parietal cortex to anchor and support the implant, and were secured with dental adhesive (C&B Metabond, Parkell). An additional 0.5 mm craniotomy was made over the right cerebellum for insertion of the indifferent ground and reference wires. The craniotomy centered at -1.95 mm AP and 1.5 mm ML from bregma and extended bidirectionally along the ML axis to 2 mm width to receive the recording probe. The probes had four 5 mm shanks spaced 400  $\mu$ m apart with 8 electrode sites per shank and 200  $\mu$ m spacing between sites (Neuronexus; configuration A4x8-400-200-704-CM32). The probe was quickly lowered until the tip reached 2.2 mm below the surface of the brain, and the reference and ground wire was inserted into the subdural space above the cerebellum. The probe was cemented in place with dental acrylic and the scalp was closed with nylon sutures. Mice were treated with 0.0375 mg/kg buprenorphine intraperitoneally and 5 mg/kg ketofen subcutaneously 30–45 min after surgery, monitored until ambulatory, then monitored daily for 3 days. A minimum of 3 weeks was allowed for recovery and viral expression before recording.

## **Electrophysiology**

Data from all mice was collected, amplified, multiplexed, processed, and digitized with 32-channel Upright Headstage, commutator, and Main Control Unit (SpikeGadgets). Simultaneous data acquisition at 30 kHz and video tracking at 30 frames/s was performed using Trodes software (SpikeGadgets). Each animal was randomly assigned a time during the light cycle, and behavior and recordings were always conducted with that animal at that same time each day  $\pm$  1 hour. CNO (NIMH, C-929) was prepared in 1% DMSO in 0.9% sterile saline and administered via intraperitoneal injection daily at a dose of 2 mg/kg 1 hour prior to data collection. Body weight was measured weekly during treatment and injection volume was adjusted accordingly. Control mice were injected with a matched volume of 1% DMSO in 0.9% sterile saline. Injections were well tolerated and had no adverse effects on health. Data were collected during 60 min home cage sessions for 7 days, alternating vehicle and CNO administration. During recordings, home cages were changed to Alpha-dri bedding (Shepherd Specialty Papers) to enable video tracking.

For recordings during the active place avoidance task<sup>53</sup>, data was collected for 20 min immediately prior to and 20 min immediately following each trial. In all trials, mice were placed in a 40 cm diameter arena that rotates at 1 rpm (BioSignal Group). On the first day, mice habituated to the environment by exploring it for 10 minutes. On the following 4 days, when mice entered a 60° region which is fixed relative to the room, as measured by video tracking, they received a 0.2 mA foot shock for 500 ms at 60 Hz every 1.5 s until they left the shock zone. Mice could only use spatial cues on the walls around the arena to actively avoid this shock zone given the constant rotation of the arena. SWR rate was analyzed only on the first day of training.

## **Histology**

Mice were deeply anesthetized with avertin, and a 30  $\mu$ A current was passed through each recording site for 2 s to generate small electrolytic lesions (Ugo Basile). Mice were then perfused with 0.9% NaCl. The brains were removed and stored at 4°C, then fixed in 4% PFA for 2 days, rinsed in PBS for 1 day, and cryoprotected in 30% sucrose for at least 2 days. Brains were cut into 30  $\mu$ m coronal sections with a microtome (Leica) and stored in cryoprotectant at -20°C. Every third section was stained with cresyl violet, then electrolytic lesion locations were observed under a light microscope (Leica). Every tenth section was used for immunohistochemistry. Sections were blocked and permeabilized in 10% normal donkey serum and 0.5% Triton X for 1 hour at room temperature, and then incubated overnight at 4°C in 1:100 rat anti-SST (Millipore cat# MAB354, RRID:AB\_2255365), 1:1000 mouse anti-PV (Millipore cat# MAB1572, RRID:AB\_2174013), and 1:500 biotinylated rabbit anti-RFP (Abcam cat# ab34771, RRID:AB\_777699). Sections were then incubated for 1 hour at room temperature in 1:1500 donkey anti-rat AlexaFluor488 (Thermo Fisher Scientific cat# A-21208, RRID:AB\_2535794) or 1:1500 goat anti-rat AlexaFluor647 (Thermo Fisher Scientific cat# A-21247, RRID:AB\_141778), 1:1500 donkey anti-mouse AlexaFluor647 (Thermo Fisher Scientific cat# A-31571, RRID:AB\_162542), and 1:1000 Streptavidin AlexaFluor594 (Sigma Aldrich cat# S6402) and mounted to slides using DAPI. Images were collected on a fluorescent microscope (Keyence) and counted manually in ImageJ. Representative images were adjusted for contrast only.

## ***Ex vivo* electrophysiology**

3–6 month old mice were stereotaxically injected with hM4D as described above, then the scalp was sutured closed. 3 weeks following surgery to allow for viral expression, mice were deeply

anesthetized with isoflurane. The brain was rapidly removed and placed in 4°C slicing solution comprised of 110 mM Choline Chloride, 2.5 mM KCl, 1.25 mM NaH<sub>2</sub>PO<sub>4</sub>, 26 mM NaHCO<sub>3</sub>, 2 mM CaCl<sub>2</sub>, 1.3 mM Na Pyruvate, 1 mM L-Ascorbic Acid, and 10 mM dextrose. 300µm sagittal sections were cut using a vibratome (VT 1200s, Leica), transferred to a vapor interface chamber aerated with 95% O<sub>2</sub>/ 5% CO<sub>2</sub> gas mixture, and allowed to recover at 34°C for one hour prior to recording. Sections were then transferred to a submerged recording chamber at 34°C perfused at 10 mL/min with oxygenated aCSF solution comprised of 124 mM NaCl, 26 mM NaHCO<sub>3</sub>, 10 mM Glucose, 1.25 mM NaH<sub>2</sub>PO<sub>4</sub>, 2.5 mM KCl, 1.25 mM MgCl<sub>2</sub>, and 1.5 mM CaCl<sub>2</sub>. SST<sup>+</sup> and PV<sup>+</sup> cells were visually identified in the DG by mCherry expression and morphology using a modified Olympus BXW-51 microscope (Scientifica, Inc). Interneurons were recorded using patch-clamp electrodes filled with an intracellular solution comprised of 125 mM K-gluconate, 10 mM KCl, 10 mM HEPES, 2 mM MgCl<sub>2</sub>, 10 mM EGTA, 4 mM MgATP, 10 mM Na-phosphocreatine, and 3 mM Na<sub>2</sub>GTP. CNO was dissolved to 1µM in aCSF and delivered through the perfusion system. Whole cell recordings were performed using a Multiclamp 700B amplifier (Molecular Devices). The signals were sampled at 10 kHz and digitized using Digidata 1550B with Clampex 10 software (Molecular Devices). Data was analyzed using custom scripts in IGOR Pro software (WaveMetrics).

### **Analysis of neural data**

Neural data was analyzed with custom software written in MATLAB (Mathworks) with the Chronux toolbox (<http://www.chronux.org>) and Trodes to MATLAB software (SpikeGadgets). The anatomical location of each electrode site was determined by examining Nissl-stained histological sections, raw LFP traces, the SWR-triggered spectrogram signature, and dentate

spikes. Data were band-pass Butterworth filtered at 0.1–300 Hz, then downsampled to 1000 Hz and analyzed as LFP. Raw LFP data were band-pass equiripple filtered at 125–200 Hz for SWRs, 0–30 Hz for sharp waves, and at 30–50 Hz for SG. SWRs were detected on the CA1 site closest to the center of the pyramidal layer and defined by the Hilbert envelope of the ripple-filtered trace, smoothed with a 4 ms Gaussian, exceeding 3 SD above baseline for at least 15 ms<sup>25</sup>. Analysis of SWRs was restricted to periods of extended immobility, after the mouse Gaussian smoothed velocity had been < 1 cm/s for 30 seconds or more. SWRs were considered part of chains if a second SWR event occurred within 200 ms of the end of an event. Instantaneous frequency was defined by intrapeak times. Sharp wave amplitude was defined as the maximum absolute value of the Hilbert envelope of the sharp wave-filtered trace during SWRs. SWRs in CA3 were detected on the site with the highest MUA and examined only when they coincided with an SWR detected in CA1.

SWR-triggered spectrograms for each electrode site and SWR-triggered coherence between regions were calculated with the multitaper method, as previously described<sup>54</sup>, with a 100 ms sliding window. For illustration in figures, a 10 ms sliding window was used. SWR-associated SG power was calculated as the averaged z-scored power over the 30–50 Hz frequency band 0–100 ms after ripple detection. This was then averaged over all SWR events and over all electrode sites within that cell layer or subregion. SG power was analyzed for three regions: CA1 stratum radiatum, CA3 including stratum pyramidale and stratum radiatum, and dentate gyrus including hilus and granule cell layers. Only dentate gyrus sites with visually confirmed dentate spikes were included in analysis. For CNO epochs, the mean and SD of the slow gamma filtered signal from the vehicle epoch recorded the day before were used for z-scoring.

For multi-unit analysis, data were referenced to a corpus callosum electrode, band-pass

Butterworth filtered at 600–6000 Hz, and then events greater than 75  $\mu$ V were analyzed as spikes. Sites used for SWR detection were further verified to be in the CA1 pyramidal layer by measuring large increases in multi-unit activity during SWRs. The site closest to the center of the cell layer, as determined by highest MUA, was used for MUA analysis. For fast ripple analysis, data were downsampled to 5 kHz and band-pass equiripple filtered at 125–600 Hz, then events were detected in CA1 when the Hilbert envelope of the ripple-filtered trace, smoothed with a 4 ms Gaussian, exceeded 3 SD above baseline for at least 3 oscillations of the filtered trace. Events were classified as fast ripples if the mean frequency was above 250 Hz. All measurements were analyzed per session, then averaged across all sessions. Thus, each mouse contributed a single number to all comparisons.

## **QUANTIFICATION AND STATISTICAL ANALYSIS**

Statistics were computed using custom software written in MATLAB (Mathworks). Statistical test used, exact n, test statistic values, degrees of freedom, and exact p value are in figure legends. When a central value is plotted, it is always mean  $\pm$  SEM, as indicated in figure legends. In all cases, n represents number of animals. Significance was established as  $p < 0.05$ . No data were excluded based on statistical tests. 3 mice were excluded from analysis due to poor viral expression. Sample sizes were based on previous studies<sup>52,55–57</sup>. Most data were normally distributed as shown by Shapiro-Wilk test, and variances between groups were similar as shown by F test. In these instances, we used paired and unpaired t tests. When these assumptions were violated, we used Wilcoxon matched pairs signed rank tests and rank sum tests.



## Results

### Recording *in vivo* hippocampal LFP during chemogenetic suppression of PV<sup>+</sup> and SST<sup>+</sup> interneurons in CA3 and DG

We used a Cre-dependent chemogenetic approach to silence specific interneuron subtypes in CA3 and DG. We bilaterally injected PVCre, SSTCre, and PVCre/SSTCre mice with AAV5-hSyn-DIO-hM4D(Gi)-mCherry or with AAV5-hSyn-DIO-mCherry into the DG hilus, then implanted with a 32-site silicon electrode array into the right dorsal hippocampus (**Fig. 3.1A**). Hm4D expression was highly co-localized with PV and SST expression (**Fig. 3.2A** and **3.2B**) and extended throughout CA3 and DG (**Fig. 3.1B** and **3.2C**) from dorsal to ventral hippocampus (**Fig. 3.1C**). We confirmed hM4D function by observing that CNO application to ex vivo hippocampal slices reduced firing rates (**Fig. 3.2D**), hyperpolarized by  $-8.61 \pm 1.3\text{mV}$  (**Fig. 3.2E**), and increased input resistance (**Fig. 3.2F**) in PV<sup>+</sup> and SST<sup>+</sup> interneurons expressing hM4D. After viral expression, we recorded LFP activity from all hippocampal subregions during sleep and awake rest over 7 daily 1 hour sessions, alternating CNO and vehicle treatment (**Fig. 3.1B**).

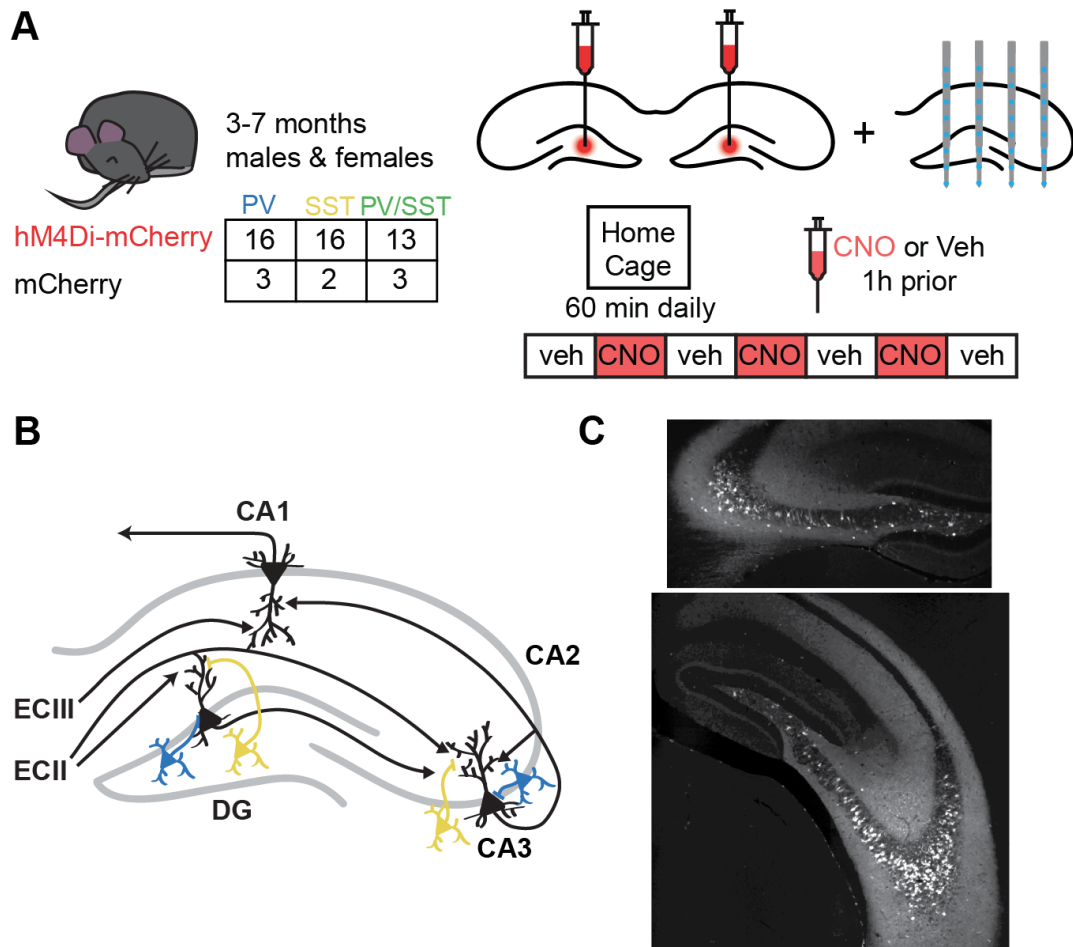


**Figure 3.1. Recording *in vivo* hippocampal LFP during chemogenetic suppression of PV<sup>+</sup> and SST<sup>+</sup> interneurons in CA3 and DG.**

(A) Simplified circuit diagram of the hippocampus. CA3 and DG receive excitatory inputs from layer II of entorhinal cortex onto distal dendrites and inhibitory inputs from local PV<sup>+</sup> interneurons (blue) onto the soma and local SST<sup>+</sup> interneurons (yellow) onto distal dendrites. Adapted with permission from (Gillespie et al., 2016).

(B) Experimental strategy. Mice were bilaterally injected with AAV5-hSyn-DIO-hM4D(Gi)-mCherry or with AAV5-hSyn-DIO-mCherry into the DG hilus, then implanted with a 32-site silicon electrode array into the right dorsal hippocampus. LFP activity was recorded from all hippocampal subregions during sleep and awake rest over 7 daily 1 hour sessions, alternating CNO and vehicle treatment.

(C) Example of mCherry expression in dorsal (top) and ventral (bottom) hippocampus.

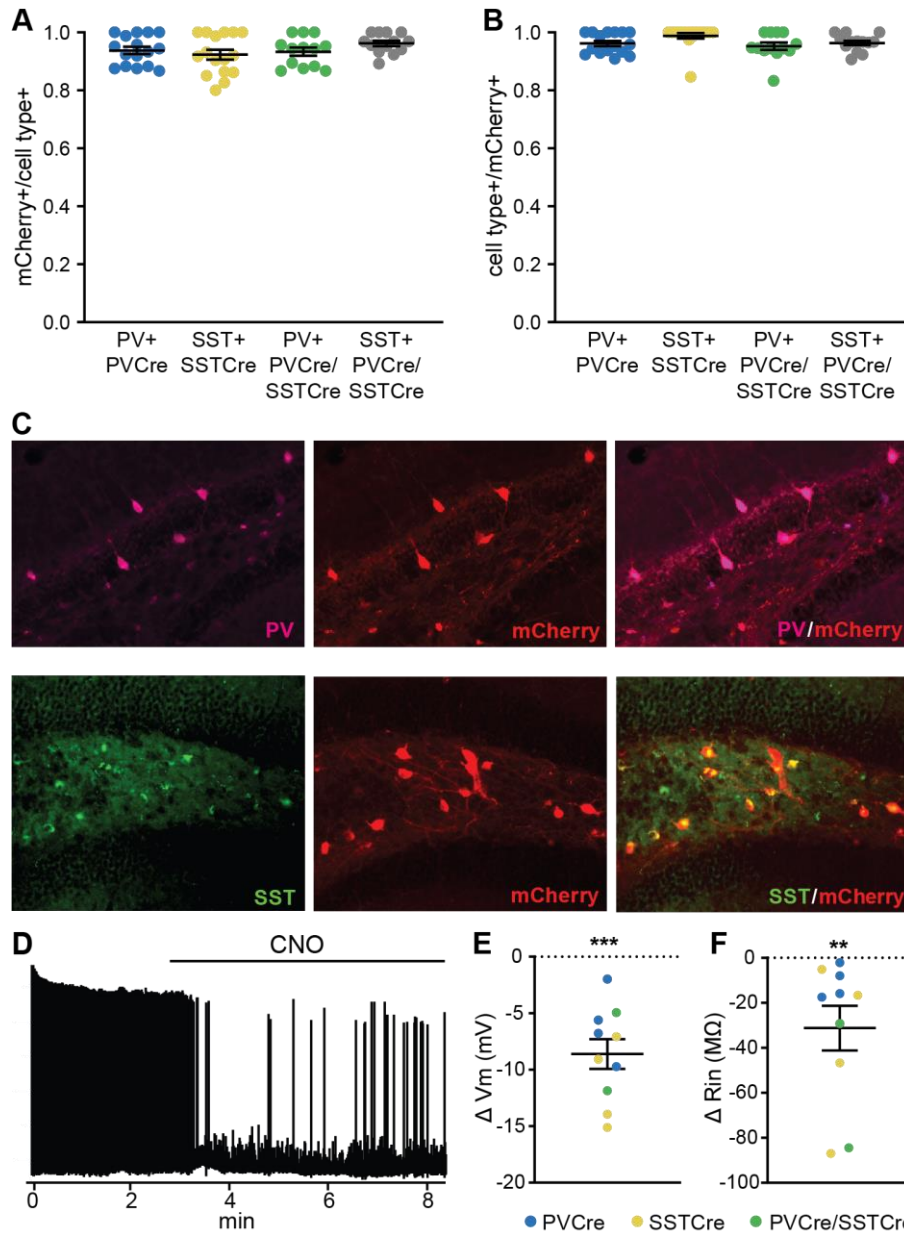


**Figure 3.2. DREADDs function and expression in PV<sup>+</sup> and SST<sup>+</sup> interneurons in CA3 and DG.**

(A, B) Proportion of (A) mCherry<sup>+</sup> cells in PV<sup>+</sup> and SST<sup>+</sup> cells and (B) PV<sup>+</sup> and SST<sup>+</sup> cells in mCherry<sup>+</sup> cells. N = 16 PVCre mice, n = 16 SSTCre mice, and n = 13 PVCre/SSTCre mice.

(C) Example of mCherry coexpression with PV (top) and SST (bottom) in DG.

(D) CNO application to *ex vivo* hippocampal sections reduces firing rates in a PV<sup>+</sup> interneuron in a PVCre animal expressing hM4D.

(E,F) CNO application on PV<sup>+</sup> and SST<sup>+</sup> interneurons expressing hM4D in the DG in *ex vivo* hippocampal sections (D) hyperpolarizes cells (1-sample t test,  $t(9)=6.57$ ,  $p = 0.0001$ ) and (E) increases input resistance (1-sample Wilcoxon test,  $W = -55$ ,  $p = 0.002$ ). N = 4 PVCre slices, n = 4 SSTCre slices, and n = 2 PVCre/SSTCre slices.

Error bars are mean  $\pm$  SEM. \*\*\* $p < 0.001$ .

### Suppressing PV<sup>+</sup> interneurons increases CA3 coupling onto CA1 during SWRs

We first examined the effect of PV<sup>+</sup> interneurons. Suppressing PV<sup>+</sup> interneurons in CA3 and DG increased SWR rate (**Fig. 3.3A**). This effect was not due to differences in SWR detection (**Fig. 3.4A** and **3.4B**). Interestingly, learning-induced increases in SWR rate were abolished (**Fig. 3.3B**). This increase in rate was not due to an increase SWR bursts (**Fig. 3.3C**). Since hippocampal interneuron ablation leads to seizures<sup>58</sup>, we looked for epileptic signatures. While we observed no seizures, we did detect an increase in fast ripple rate when PV<sup>+</sup> interneurons were suppressed (**Fig. 3.3D**). Recruitment of multi-unit activity (MUA) during SWRs was elevated in CA1, CA3, and DG (**Fig. 3.3E**). However, SWR size was smaller (**Fig. 3.3F**), as evident by reduced ripple frequency power during SWRs (**Fig. 3.3G**). Thus there was no relationship between increased MUA recruitment and greater peak amplitude of the ripple-filtered trace. Because SWR size decreased, SWR rate at very high detection thresholds also decreased (**Fig. 3.4C**). SWR frequency in CA1 increased (**Fig. 3.3H**), but decreased in CA3 (**Fig. 3.4D**), suggesting that the local effect of these interneurons and the downstream effects are quite different. There was no change in the cycle length of SWRs (**Fig. 3.3I**), but SWR temporal length decreased (**Fig. 3.3J**), likely due to the increased frequency. Overall, suppressing PV<sup>+</sup> interneurons in CA3 and DG increased CA3 coupling onto CA1, leading to faster and more SWRs with greater CA1 MUA recruitment.

We then measured two frequency components coincident with ripples, both of which are driven by CA3: sharp waves (SW)<sup>10</sup> and slow gamma (SG) power<sup>54,59,60</sup> (**Fig. 3.3K**). During PV<sup>+</sup> suppression, SW amplitude in CA1 was increased (**Fig. 3.3L**). SG power was higher on average in CA1, and variance of SG power was elevated in all 3 subregions (**Fig. 3.4E** and **3.4F**). We therefore used mean and SD SG power calculated from vehicle-treated epochs to z-score SG power during all epochs. Suppressing PV<sup>+</sup> interneurons lead to greater SWR-coincident SG power in

CA1, CA3, and DG (**Fig. 3.3M**). Therefore, CA3 coupling likely increased not only to CA1, but also back to DG and to CA3. Interestingly, the extent of CA1 SWR-coincident SG power increase correlated across animals with the extent of sharp wave amplitude increase and the extent of SWR frequency increase (**Fig. 3.4G** and **3.4H**), suggesting these features may be similarly controlled, in line with previous findings<sup>61,62</sup>. Instantaneous frequency of this SG did not change (**Fig. 3.4I**). While coherence between CA3 and CA1 and between DG and CA1 in the SG frequency band did increase during SWRs (**Fig. 3.4J**), the extent of this increase did not change when PV<sup>+</sup> interneurons were suppressed (**Fig. 3.3N**). Thus, suppressing PV<sup>+</sup> interneurons increased SG power – likely driven by CA3 – during and outside of SWRs, but this did not increase coherence between subregions, in line with previous findings that these two aspects of gamma oscillations may be modulated through separate mechanisms<sup>5</sup>.

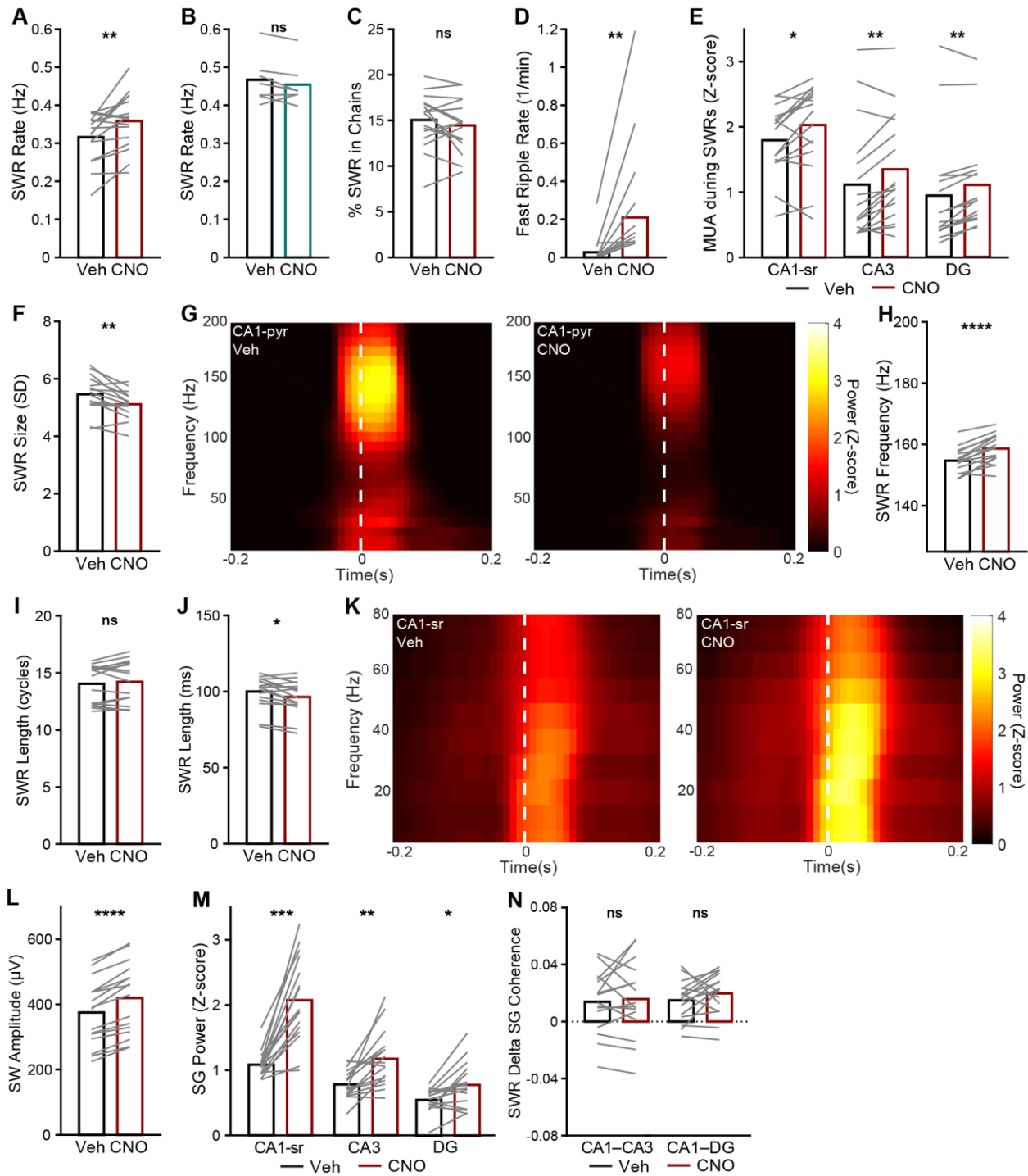


**Figure 3.2. Suppressing PV<sup>+</sup> interneurons increases CA3 coupling onto CA1 during SWRs.**

(A) SWR rate ( $Z = 2.74$ ,  $p = 0.006$ ).

(B) SWR rate before and after each trial of active place avoidance learning ( $Z = 1.18$ ,  $p = 0.24$ ,  $n = 7$  PVCre mice).

(C) Percent of SWRs following another SWR within 200 ms ( $t(15) = 1.19$ ,  $p = 0.3$ ).

(D) Fast ripple rate ( $Z = 2.93$ ,  $p = 0.003$ ).

(E) Normalized recruitment to SWRs of multi-unit activity in CA1 ( $Z = 2.33$ ,  $p = 0.02$ ), CA3 ( $Z = 2.59$ ,  $p = 0.097$ ), and DG ( $Z = 3$ ,  $p = 0.003$ ).

(F) SWR size ( $t(15) = 3.64$ ,  $p = 0.002$ ).

(G) Representative SWR-triggered spectrograms from a CA1 pyramidal cell layer site during vehicle-treated epochs (left) and CNO-treated epochs (right) in a PVCre mouse. White dash lines represent threshold crossing for SWR detection.

(H) SWR instantaneous frequency ( $t(15) = 5.44$ ,  $p = 0.0001$ ).

(I) SWR cycle length ( $t(12) = 0.85$ ,  $p = 0.4$ ).

(J) SWR temporal length ( $Z = 2.48$ ,  $p = 0.01$ ).

(K) Representative SWR-triggered spectrograms from a CA1 stratum radiatum layer site during vehicle-treated epochs (left) and CNO-treated epochs (right) in a PVCre mouse. White dash lines represent threshold crossing for SWR detection.

(L) Sharp wave amplitude ( $t(15) = -9.40$ ,  $p < 0.0001$ ).

(M) Normalized SG power during SWRs in CA1 ( $Z = 3.52$ ,  $p = 0.0004$ ), CA3 ( $t(15) = 3.96$ ,  $p = 0.001$ ), and DG ( $Z = 2.53$ ,  $p = 0.01$ ).

(N) Increase during SWRs of SG frequency band coherence between CA3 and CA1 ( $t(15) = 0.47$ ,  $p = 0.6$ ) and between DG and CA1 ( $t(15) = 1.29$ ,  $p = 0.2$ ).

N = 16 PVCre mice except where specified. Paired t tests when the test statistic given is t and Wilcoxon matched pairs signed rank test when the test statistic given is Z. \* $p < 0.05$ ; \*\* $p < 0.01$ ; \*\*\* $p < 0.001$ ; \*\*\*\* $p < 0.0001$ .

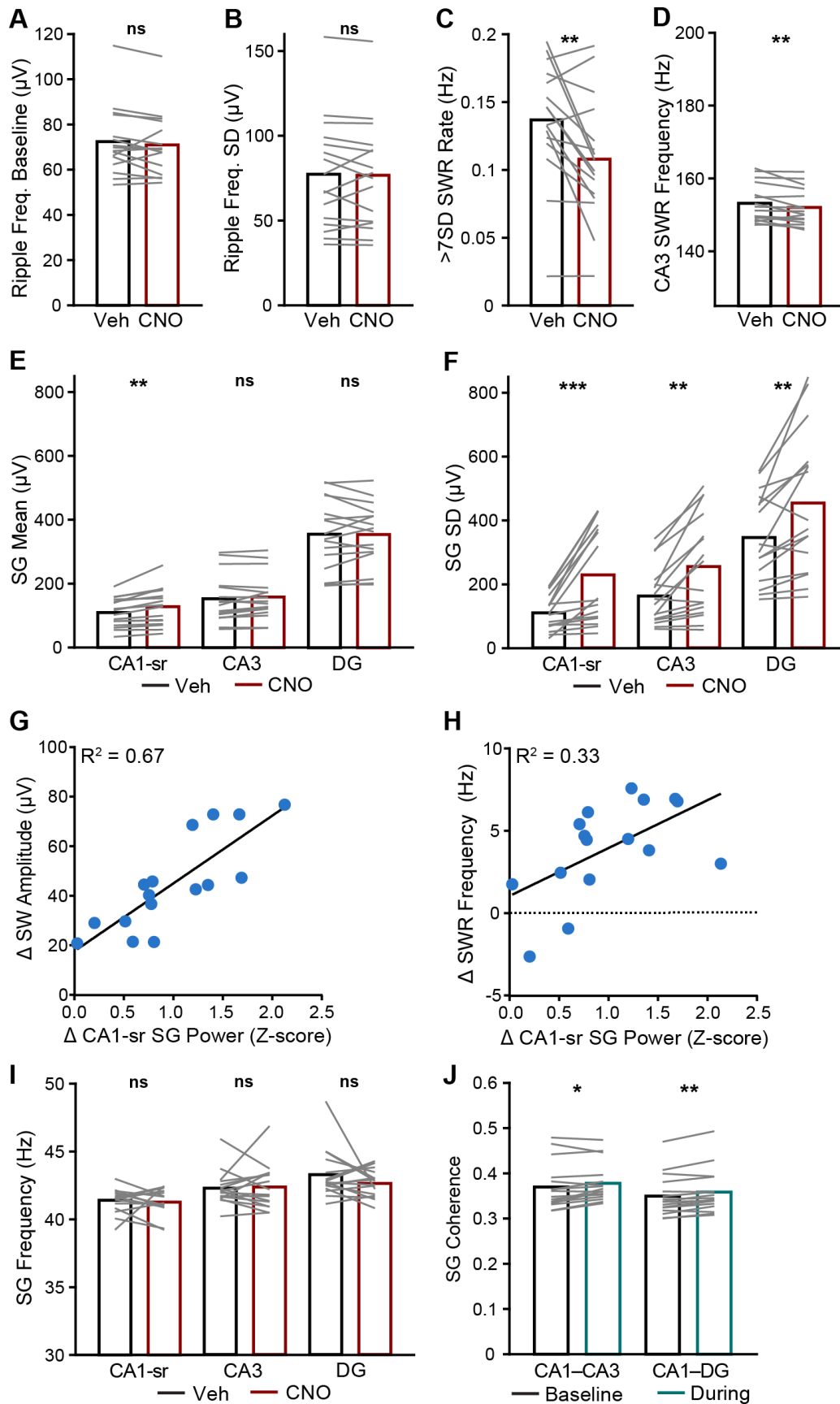




**Figure 3.4. Properties of SWRs during PV<sup>+</sup> interneuron suppression.**

(A,B) SWR frequency activity (A) mean ( $Z = 1.6$ ,  $p = 0.1$ ) and (B) SD ( $t(15) = 0.32$ ,  $p = 0.8$ ).

(C) Rate of SWRs  $> 7$  SD above baseline ( $t(15) = 3.38$ ,  $p = 0.004$ ).

(D) SWR instantaneous frequency in CA3 ( $Z = 2.59$ ,  $p = 0.0097$ ).

(E,F) SG frequency activity (E) mean in CA1 ( $t(15) = 4.03$ ,  $p = 0.001$ ), CA3 ( $t(15) = 1.49$ ,  $p = 0.2$ ), and DG ( $t(15) = 0.15$ ,  $p = 0.9$ ) and (F) SD in CA1 ( $Z = 3.52$ ,  $p = 0.0004$ ), CA3 ( $t(15) = 3.94$ ,  $p = 0.001$ ), and DG ( $t(15) = 3.47$ ,  $p = 0.003$ ) during prolonged immobility.

(G,H) SWR-coincidence SG power in CA1 predicts (G) sharp wave amplitude ( $F(1,14) = 27.9$ ,  $p = 0.0001$ ) and (H) SWR frequency ( $F(1,14) = 6.8$ ,  $p = 0.02$ ). Pearson correlation.

(I) Instantaneous frequency during SWRs of SG in CA1 ( $t(15) = 0.45$ ,  $p = 0.7$ ), CA3 ( $Z = 0.21$ ,  $p = 0.8$ ), and DG ( $Z = 1$ ,  $p = 0.3$ ).

(J) SG frequency band coherence between CA3 and CA1 ( $Z = 2.28$ ,  $p = 0.02$ ) and between CA3 and DG ( $Z = 3$ ,  $p = 0.003$ ) increases during SWRs as compared to baseline during prolonged immobility.

$N = 16$  PVCre mice. Paired t tests when the test statistic given is t and Wilcoxon matched pairs signed rank test when the test statistic given is Z. \* $p < 0.05$ ; \*\* $p < 0.01$ ; \*\*\* $p < 0.001$ ; \*\*\*\* $p < 0.0001$ .

### **Suppressing SST<sup>+</sup> interneurons decreases CA3 coupling onto CA1 during SWRs**

We next examined the effect of SST<sup>+</sup> interneurons. Suppressing SST<sup>+</sup> interneurons in CA3 and DG decreased SWR rate (**Fig. 3.5A**), which again was not due to differences in SWR detection (**Fig. 3.6A** and **3.6B**). However, learning-induced increases in SWR rate were intact (**Fig. 3.5B**). There was a dramatic decrease in the proportion of SWRs that participated in chains (**Fig. 3.5C**), suggesting increased coupling from ECII may disrupt SWR chains. This loss of SWR chains could not fully explain the reduction in SWR rate (**Fig. 3.6C**). There was no increase in fast ripple rate (**Fig. 3.5D**), thus PV<sup>+</sup> interneurons may be the gating interneuron type for this pathological activity. Recruitment of multi-unit activity (MUA) during SWRs was elevated in CA3 and DG, but not CA1 (**Fig. 3.5E**). Thus, while suppressing interneurons broadly increased local principal cell recruitment to SWRs, downstream principal cell recruitment only increased when CA3 coupling was elevated by suppressing PV<sup>+</sup> interneurons. SWR size did not change (**Fig. 3.5F**). SWR frequency in CA1 decreased modestly (**Fig. 3.5G**), but did not change in CA3 (**Fig. 3.6D**), therefore these interneurons have a downstream effect but no local effect on this measure. The number of cycles per SWR increased (**Fig. 3.5H**), as did the temporal length (**Fig. 3.5I**). Since EC activity increases prior to SWRs longer than 100 ms<sup>62</sup>, we looked specifically at the proportion of SWRs longer than 100 ms and found an increase (**Fig. 3.5J**). Overall, suppressing SST<sup>+</sup> interneurons in CA3 and DG decreased CA3 coupling onto CA1, leading to longer and fewer SWRs which were less likely to appear in chains.

We then measured SWs and SG power coincident with SWRs. During SST<sup>+</sup> interneuron suppression, SW amplitude did not change (**Fig. 3.5K**), and SG power did not change at baseline (**Fig. 3.6E** and **3.6F**) nor during SWRs (**Fig. 3.5L**), except for a modest increase in SG power in DG during SWRs. Instantaneous frequency of this SG also did not change (**Fig. 3.6G**).

Interestingly, the extent of SG frequency band coherence increase during SWRs between CA3 and CA1 and between DG and CA1 was suppressed to below zero. Thus, SST<sup>+</sup> interneurons may orchestrate the coordination of SG oscillations between hippocampal subregions.

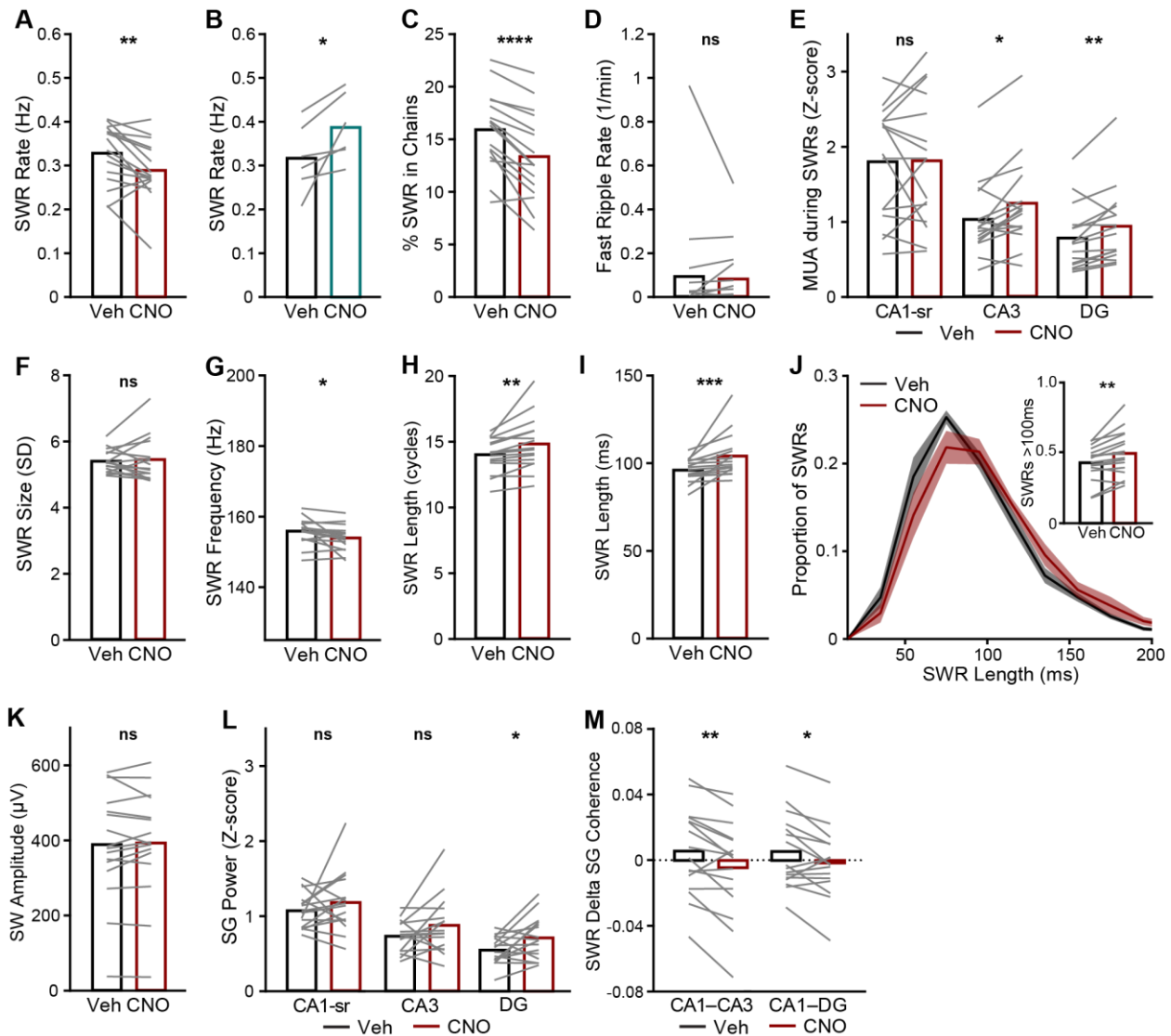


**Figure 3.5. Suppressing SST<sup>+</sup> interneurons decreases CA3 coupling onto CA1 during SWRs.**

(A) SWR rate ( $t(15) = 3.13$ ,  $p = 0.007$ ).

(B) SWR rate before and after one trial of active place avoidance learning ( $t(5) = 2.7$ ,  $p = 0.04$ ,  $n = 6$  SSTCre mice).

(C) Percent of SWRs following another SWR within 200 ms ( $t(15) = 6.09$ ,  $p < 0.0001$ ).

(D) Fast ripple rate ( $Z = 1.17$ ,  $p = 0.2$ ).

(E) Normalized recruitment to SWRs of multi-unit activity in CA1 ( $t(15) = 0.1$ ,  $p = 0.9$ ), CA3 ( $Z = 2.53$ ,  $p = 0.01$ ), and DG ( $Z = 2.59$ ,  $p = 0.0097$ ).

(F) SWR size ( $Z = 0.1$ ,  $p = 0.9$ ).

(G) SWR instantaneous frequency ( $t(15) = 2.29$ ,  $p = 0.04$ ).

(H) SWR cycle length ( $t(15) = 3.05$ ,  $p = 0.008$ ).

(I) SWR temporal length ( $Z = 3.52$ ,  $p = 0.0004$ ).

(J) Distribution of SWR lengths; inset: proportion of SWRs > 100 ms ( $t(15) = 3.67$ ,  $p = 0.002$ ).

(K) Sharp wave amplitude ( $t(15) = 0.55$ ,  $p = 0.6$ ).

**(L)** Normalized SG power during SWRs in CA1 ( $t(15) = 1.07$ ,  $p = 0.3$ ), CA3 ( $t(15) = 1.69$ ,  $p = 0.1$ ), and DG ( $t(15) = 2.42$ ,  $p = 0.03$ ).

**(M)** Increase during SWRs of SG frequency band coherence between CA3 and CA1 ( $t(15) = 3.69$ ,  $p = 0.002$ ) and between DG and CA1 ( $t(15) = 2.59$ ,  $p = 0.02$ ).

N = 16 SSTCre mice except where specified. Paired t tests when the test statistic given is t and Wilcoxon matched pairs signed rank test when the test statistic given is Z. \* $p < 0.05$ ; \*\* $p < 0.01$ ; \*\*\* $p < 0.001$ ; \*\*\*\* $p < 0.0001$ . Error bars are mean  $\pm$  SEM.

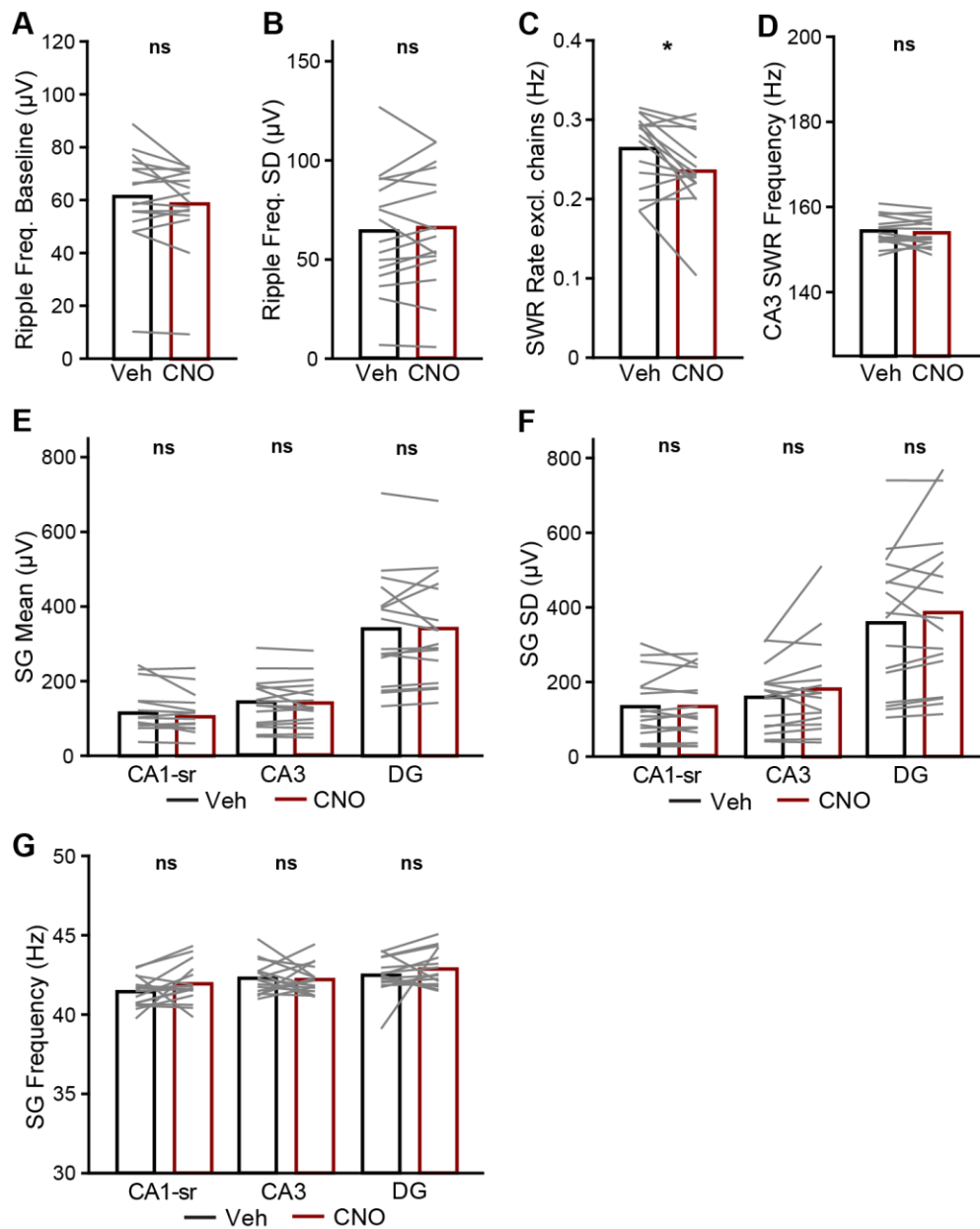


**Figure 3.6. Properties of SWRs during SST<sup>+</sup> interneuron suppression. Related to Figure 3.**

(A,B) SWR frequency activity (A) mean ( $Z = 1.24$ ,  $p = 0.2$ ) and (B) SD ( $t(15) = 0.66$ ,  $p = 0.5$ ).

(C) SWR rate with chains of SWRs excluded ( $Z = 2.38$ ,  $p = 0.02$ ).

(D) SWR instantaneous frequency in CA3 ( $t(15) = 0.88$ ,  $p = 0.4$ ).

(E,F) SG frequency activity (E) mean in CA1 ( $t(15) = 1.8$ ,  $p = 0.09$ ), CA3 ( $t(15) = 0.6$ ,  $p = 0.6$ ), and DG ( $t(15) = 0.1$ ,  $p = 0.94$ ) and (F) SD in CA1 ( $t(15) = 0.1$ ,  $p = 0.96$ ), CA3 ( $Z = 1.4$ ,  $p = 0.16$ ), and DG ( $t(15) = 1.4$ ,  $p = 0.19$ ) during prolonged immobility.

(G) Instantaneous frequency during SWRs of SG in CA1 ( $t(15) = 1.6$ ,  $p = 0.14$ ), CA3 ( $t(15) = 0.3$ ,  $p = 0.8$ ), and DG ( $Z = 0.9$ ,  $p = 0.4$ ).

$N = 16$  SSTCre mice. Paired  $t$  tests when the test statistic given is  $t$  and Wilcoxon matched pairs signed rank test when the test statistic given is  $Z$ . \* $p < 0.05$ ; \*\* $p < 0.01$ ; \*\*\* $p < 0.001$ ; \*\*\*\* $p < 0.0001$ .

Lastly, we assessed the effect of suppressing both interneuron populations simultaneously in PVCre/SSTCre mice. All SWR features changed in the same magnitude and direction as suppressing PV<sup>+</sup> interneurons alone, with the exception of SG coherence during SWRs (**Fig. 3.7**). This suggests that many of these SWR features may either be dominated by somatic inhibition or that SST<sup>+</sup> interneurons may affect these features through inhibiting PV<sup>+</sup> interneurons. SG coherence in contrast may be driven primarily by dendritic inhibition.

To assess the robustness of these effects, we assessed both males and females, since females have more DG interneurons than males at this age<sup>63</sup>. Males had higher SWR rates and slower SG frequency in CA1 and CA3 than females during vehicle treatment epochs (**Table 3.1**), but there were otherwise no sex differences on SWR features. The effect of suppressing interneurons was in the same direction and magnitude in both sexes on most SWR features (**Table 3.2**). Interestingly, suppressing SST<sup>+</sup> interneurons decreased CA1 SG power and MUA during SWRs in females, but modestly increased it in males, leading to no effect on average. In sum, SST<sup>+</sup> interneuron modulation of CA1 engagement during SWRs is bidirectional in a sex-dependent manner. Finally, to control for possible off-target effects of CNO, we treated mice injected with an empty vector as a control and observed no differences between vehicle and CNO treated epochs (**Fig. 3.7**).

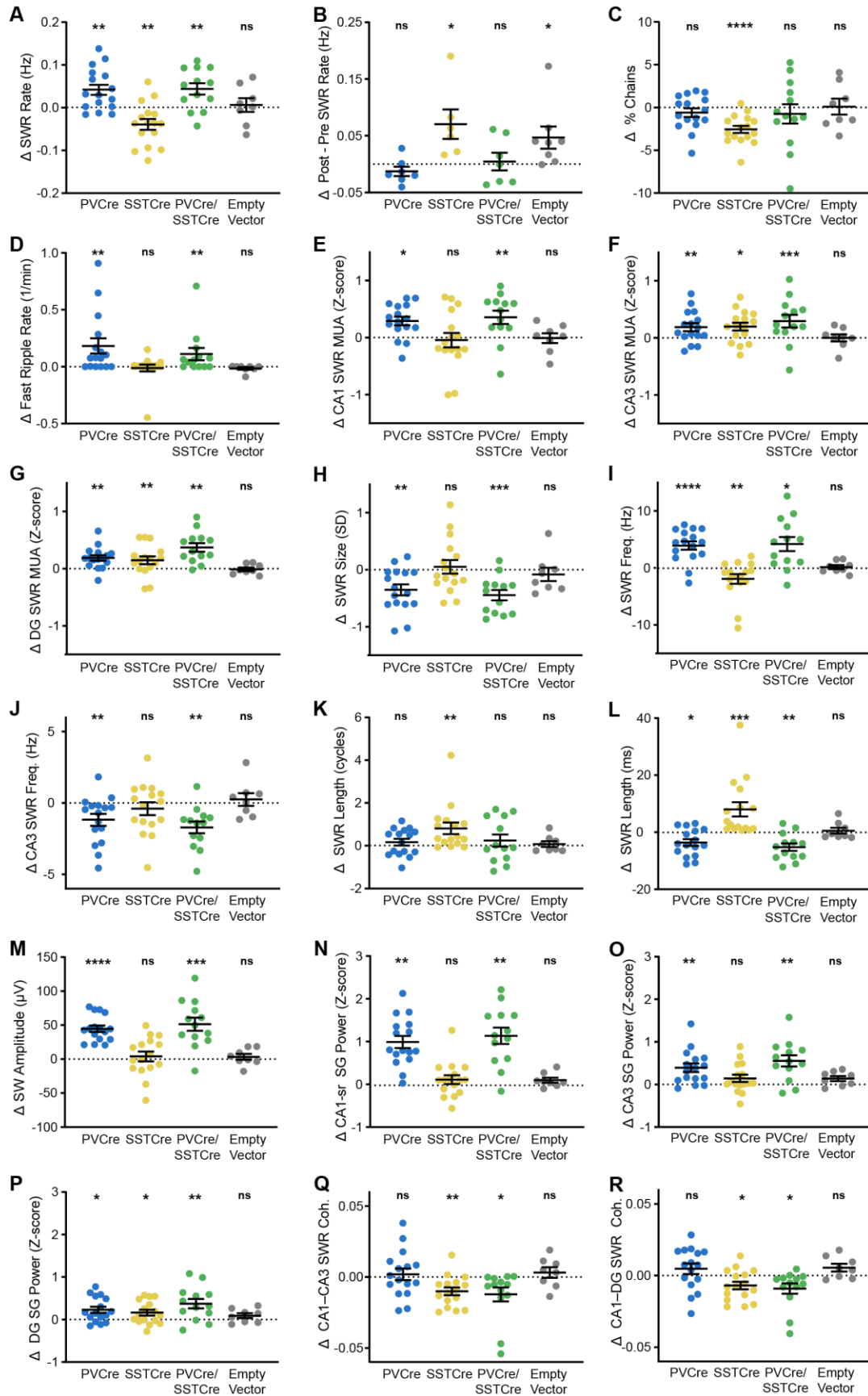




**Figure 4.7. Suppressing both PV<sup>+</sup> and SST<sup>+</sup> interneurons increases CA3 coupling onto CA1 during SWRs.**

**(A)** SWR rate (PVCre/SSTCre (P/S):  $t(12) = 3.3$ ,  $p = 0.006$ ; Empty Vector (EV):  $t(7) = 0.39$ ,  $p = 0.7$ ).

**(B)** SWR rate before and after each trial of active place avoidance learning (P/S:  $Z = 1.18$ ,  $p = 0.2$ ,  $n = 7$  mice; EV:  $t(7) = 2.41$ ,  $p = 0.047$ ,  $n = 8$  mice).

**(C)** Percent of SWRs following another SWR within 200 ms (P/S:  $t(12) = 0.6$ ,  $p = 0.5$ ; EV:  $t(7) = 0.1$ ,  $p = 0.9$ ).

**(D)** Fast ripple rate (P/S:  $Z = 2.67$ ,  $p = 0.008$ ; EV:  $Z = 1.46$ ,  $p = 0.1$ ).

**(E–G)** Normalized recruitment to SWRs of multi-unit activity in **(E)** CA1 (P/S:  $t(12) = 3.22$ ,  $p = 0.007$ ; EV:  $t(7) = 0.1$ ,  $p = 0.9$ ), **(F)** CA3 (P/S:  $t(12) = 4.42$ ,  $p = 0.0008$ ; EV:  $t(7) = 0.3$ ,  $p = 0.8$ ), and **(G)** DG (P/S:  $Z = 3.11$ ,  $p = 0.002$ ; EV:  $t(7) = 0.5$ ,  $p = 0.7$ ).

**(H)** SWR size (P/S:  $t(12) = 4.88$ ,  $p = 0.0004$ ; EV:  $t(7) = 0.7$ ,  $p = 0.5$ ).

**(I–J)** SWR instantaneous frequency in **(I)** CA1 (P/S:  $t(12) = 3.4$ ,  $p = 0.005$ ; EV:  $t(7) = 0.4$ ,  $p = 0.7$ ) and **(J)** CA3 (P/S:  $t(12) = 4.17$ ,  $p = 0.001$ ; EV:  $Z = 0.3$ ,  $p = 0.8$ ).

**(K)** SWR cycle length (P/S:  $t(12) = 0.9$ ,  $p = 0.4$ ; EV:  $t(7) = 0.6$ ,  $p = 0.6$ ).

**(L)** SWR temporal length (P/S:  $t(12) = 4.01$ ,  $p = 0.002$ ;  $t(7) = 0.5$ ,  $p = 0.6$ ).

**(M)** Sharp wave amplitude (P/S:  $t(12) = 5.32$ ,  $p = 0.0002$ ; EV:  $t(7) = 0.8$ ,  $p = 0.5$ ).

**(N–P)** Normalized SG power during SWRs in **(N)** CA1 (P/S:  $Z = 3.11$ ,  $p = 0.002$ ; EV:  $t(7) = 1.7$ ,  $p = 0.1$ ), **(O)** CA3 (P/S:  $Z = 2.83$ ,  $p = 0.005$ ; EV:  $t(7) = 2.35$ ,  $p = 0.051$ ), and **(P)** DG (P/S:  $t(12) = 3.4$ ,  $p = 0.005$ ; EV:  $t(7) = 1.6$ ,  $p = 0.2$ ).

**(Q,R)** Increase during SWRs of SG frequency band coherence **(Q)** between CA3 and CA1 (P/S:  $t(12) = 2.48$ ,  $p = 0.03$ ; EV:  $t(7) = 0.9$ ,  $p = 0.4$ ) and **(R)** between DG and CA1 (P/S:  $t(12) = 2.46$ ,  $p = 0.03$ ; EV:  $t(7) = 2.1$ ,  $p = 0.08$ ).

N = 16 PVCre, 16 SSTCre, and 13 PVCre/SSTCre (P/S) mice injected with hM4D vector, except where specified. N = 8 PVCre, SSTCre, and PVCre/SSTCre mice injected with empty vector (EV), except where specified. Paired t tests when the test statistic given is t and Wilcoxon matched pairs signed rank test when the test statistic given is Z. Details for PVCre and SSTCre statistical tests in legends for Figures 2 and 3, respectively. \* $p < 0.05$ ; \*\* $p < 0.01$ ; \*\*\* $p < 0.001$ ; \*\*\*\* $p < 0.0001$ . Error bars are mean  $\pm$  SEM.

**Table 3.1. Sex differences across all mice in vehicle-treated epochs.**

Feature	F mean (n = 26)	M mean (n = 27)	statistic	df	test value	p
<b>SWR Rate (Hz)</b>	<b>0.3</b>	<b>0.34</b>	<b>t</b>	<b>51</b>	<b>2.23</b>	<b>0.03</b>
SWR Proportion in Chains (Hz)	15.42	16.24	t	51	0.73	0.47
SWR Post-Pre (Hz)	0.41	0.37	t	26	1.05	0.3
Fast Ripple Rate (Hz)	0.02	0.11	Z	NA	1.84	0.07
CA1 MUA during SWRs (Z-score)	1.86	1.85	t	51	0.04	0.96
CA3 MUA during SWRs (Z-score)	1.24	1.19	Z	NA	0.28	0.78
DG MUA during SWRs (Z-score)	0.85	0.82	Z	NA	0.09	0.99
SWR Size (SD)	5.66	5.47	t	51	1.33	0.19
SWR Freq. (Hz)	155.08	154.64	t	51	0.4	0.69
CA3 SWR Freq. (Hz)	154.52	153.7	t	51	0.7	0.48
SWR Len. (cycles)	13.65	14.17	t	51	1.43	0.16
SWR Len. (ms)	97.22	97.99	t	51	0.32	0.75
Sharp Wave Amplitude ( $\mu$ V)	355.68	416.26	Welch's t	40	1.77	0.08
CA1 SG Mean ( $\mu$ V)	110.7	131.09	t	51	1.23	0.22
CA3 SG Mean ( $\mu$ V)	112	133.79	t	51	1.19	0.24
DG SG Mean ( $\mu$ V)	132.15	138.07	Z	NA	0.77	0.44
CA1 SG SD ( $\mu$ V)	137.01	149.85	Z	NA	1.02	0.31
CA3 SG SD ( $\mu$ V)	304.05	349.39	Z	NA	1.52	0.13
DG SG SD ( $\mu$ V)	292.65	351.8	Z	NA	1.68	0.09
CA1 SG Power (Z-score)	1.07	1.06	t	51	0.15	0.88
CA3 SG Power (Z-score)	0.77	0.8	t	51	0.49	0.62
DG SG Power (Z-score)	0.52	0.58	t	51	1.13	0.26
<b>CA1 SG Freq. (Hz)</b>	<b>41.67</b>	<b>41.17</b>	<b>Z</b>	<b>NA</b>	<b>2.2</b>	<b>0.03</b>
<b>CA3 SG Freq. (Hz)</b>	<b>42.62</b>	<b>42.01</b>	<b>Z</b>	<b>NA</b>	<b>2.23</b>	<b>0.03</b>
DG SG Freq. (Hz)	43.02	42.75	Z	NA	0.85	0.4
CA1-CA3 Delta Coherence	0.01	0.01	Z	NA	0.4	0.69
CA1-DG Delta Coherence	0.01	0.01	t	51	0.59	0.55

Paired t tests when the test statistic given is t and Wilcoxon matched pairs signed rank test when the test statistic given is Z. Significant comparisons are bolded. N = 15 females and n = 13 males for SWR Post-Pre.

**Table 3.2. Effects of PV<sup>+</sup> and/or SST<sup>+</sup> suppression stratified by sex.**

PVCre	F mean (n = 9)	M mean (n = 7)	statistic	df	test value	p
SWR Rate (Hz)	0.04	0.05	t	14	0.54	0.6
SWR Proportion in Chains (Hz)	-0.26	-1.05	t	14	0.76	0.46
SWR Post-Pre (Hz)	-0.008	-0.02	t	5	0.64	0.55
Fast Ripple Rate (Hz)	0.18	0.19	Z	NA	0	1
CA1 MUA during SWRs (Z-score)	0.12	0.38	t	14	1.68	0.11
CA3 MUA during SWRs (Z-score)	0.2	0.28	t	14	0.59	0.57
DG MUA during SWRs (Z-score)	0.21	0.11	t	14	1.4	0.18
SWR Size (SD)	-0.37	-0.33	t	14	0.19	0.85
SWR Freq. (Hz)	3.36	4.67	t	14	0.89	0.39
CA3 SWR Freq. (Hz)	-1.54	-0.7	t	14	1.01	0.33
SWR Len. (cycles)	-0.02	0.42	t	14	1.43	0.18
SWR Len. (ms)	-3.6	-3.64	t	14	0.02	0.99
Sharp Wave Amplitude (μV)	43.11	46.73	t	14	0.37	0.72
CA1 SG Mean (μV)	21.15	14.15	t	14	0.76	0.46
CA3 SG Mean (μV)	104.3	135.43	Z	NA	0.95	0.34
DG SG Mean (μV)	4.64	6.27	t	14	0.22	0.83
CA1 SG SD (μV)	85.63	99.79	t	14	0.29	0.77
CA3 SG SD (μV)	1.4	4.58	t	14	0.35	0.73
DG SG SD (μV)	110.01	103.88	t	14	0.09	0.93
CA1 SG Power (Z-score)	0.99	0.99	t	14	0.01	0.99
CA3 SG Power (Z-score)	0.35	0.46	Z	NA	1.16	0.24
DG SG Power (Z-score)	0.2	0.27	t	14	0.47	0.65
CA1 SG Freq. (Hz)	-0.16	-0.1	t	14	0.09	0.93
CA3 SG Freq. (Hz)	-0.14	0.39	Z	NA	0.32	0.75
DG SG Freq. (Hz)	-0.35	-1.03	Z	NA	0.11	0.92
CA1-CA3 Delta Coherence	0	0	t	14	0.38	0.71
CA1-DG Delta Coherence	0.01	0	t	14	1.34	0.2
SSTCre	F mean (n = 5)	M mean (n = 11)	statistic	df	test value	p
SWR Rate (Hz)	-0.05	-0.03	t	14	0.6	0.56
SWR Proportion in Chains (Hz)	-3.21	-2.26	t	14	1.05	0.31
SWR Post-Pre (Hz)	0.04	0.09	t	4	-0.8	0.47
Fast Ripple Rate (Hz)	0	-0.14	Z	NA	0.93	0.35
CA1 MUA during SWRs (Z-score)	<b>-0.34</b>	<b>0.17</b>	<b>Z</b>	<b>NA</b>	<b>2.15</b>	<b>0.03</b>
CA3 MUA during SWRs (Z-score)	0.23	0.21	t	14	0.19	0.85
DG MUA during SWRs (Z-score)	0.26	0.11	t	14	1.39	0.18
SWR Size (SD)	-0.2	0.17	t	14	1.47	0.16
SWR Freq. (Hz)	-4.25	-0.86	Welch's t	4.25	1.41	0.23
CA3 SWR Freq. (Hz)	-1.34	0.03	t	14	1.46	0.17

SSTCre (contd)	F mean (n = 5)	M mean (n = 11)	statistic	df	test value	p
SWR Len. (cycles)	1.37	0.56	Welch's t	4.32	1.01	0.37
SWR Len. (ms)	15.88	4.49	Z	NA	1.7	0.09
Sharp Wave Amplitude ( $\mu$ V)	0.51	5.53	t	14	0.31	0.76
CA1 SG Mean ( $\mu$ V)	8.7	10.47	Z	NA	1.02	0.31
CA3 SG Mean ( $\mu$ V)	6.17	2.34	Z	NA	0.68	0.5
DG SG Mean ( $\mu$ V)	6.86	0.94	Z	NA	1.36	0.17
CA1 SG SD ( $\mu$ V)	33.05	16.87	Z	NA	1.02	0.31
CA3 SG SD ( $\mu$ V)	6.35	4.17	t	14	0.41	0.69
DG SG SD ( $\mu$ V)	31.79	24.74	Z	NA	0	1
CA1 SG Power (Z-score)	<b>-0.21</b>	<b>0.26</b>	<b>Z</b>	<b>NA</b>	<b>2.61</b>	<b>0.01</b>
CA3 SG Power (Z-score)	-0.06	0.24	t	14	1.72	0.11
DG SG Power (Z-score)	0.03	0.22	t	14	1.38	0.19
CA1 SG Freq. (Hz)	-0.16	-0.1	t	14	0.09	0.93
CA3 SG Freq. (Hz)	-0.14	0.39	Z	NA	0.32	0.75
DG SG Freq. (Hz)	-0.35	-1.03	Z	NA	0.11	0.92
CA1-CA3 Delta Coherence	-0.02	-0.01	t	14	1.33	0.2
CA1-DG Delta Coherence	-0.01	-0.01	t	14	0.68	0.51
PVCre/SSTCre	F mean (n = 8)	M mean (n = 5)	statistic	df	test value	p
SWR Rate (Hz)	0.03	0.06	t	11	1.28	0.23
SWR Proportion in Chains (Hz)	-0.93	-0.45	Z	NA	0.22	0.83
SWR Post-Pre (Hz)	-0.005	0.06	t	5	1.7	0.15
Fast Ripple Rate (Hz)	0.16	0.04	Z	NA	0.59	0.55
CA1 MUA during SWRs (Z-score)	0.42	0.3	Z	NA	0.81	0.42
CA3 MUA during SWRs (Z-score)	0.43	0.33	t	11	0.54	0.6
DG MUA during SWRs (Z-score)	0.41	0.28	t	11	0.83	0.43
SWR Size (SD)	-0.35	-0.59	t	11	1.28	0.23
SWR Freq. (Hz)	5.16	2.67	Z	NA	0.95	0.34
CA3 SWR Freq. (Hz)	-1.49	-2.07	t	11	0.67	0.52
SWR Len. (cycles)	0.55	-0.24	t	11	1.41	0.19
SWR Len. (ms)	-6.02	-3.99	t	11	0.74	0.47
Sharp Wave Amplitude ( $\mu$ V)	55.92	44.15	t	11	0.58	0.58
CA1 SG Mean ( $\mu$ V)	22.43	34.71	t	11	0.83	0.43
CA3 SG Mean ( $\mu$ V)	110.54	90.46	Z	NA	0.22	0.83
DG SG Mean ( $\mu$ V)	24.05	16.3	t	11	0.63	0.54
CA1 SG SD ( $\mu$ V)	95.62	83.47	Z	NA	0.07	0.94
CA3 SG SD ( $\mu$ V)	38.03	40.25	t	11	0.07	0.94
DG SG SD ( $\mu$ V)	132.96	149.32	Z	NA	0.22	0.83
CA1 SG Power (Z-score)	1.21	1.02	t	11	0.46	0.65
CA3 SG Power (Z-score)	0.67	0.38	t	11	1.07	0.31

PVCre/SSTCre (contd)	F mean (n = 8)	M mean (n = 5)	statistic	df	test value	p
DG SG Power (Z-score)	0.46	0.23	t	11	1.02	0.33
CA1 SG Freq. (Hz)	0.37	0.42	t	11	0.08	0.93
CA3 SG Freq. (Hz)	-0.26	0.21	Z	NA	0.95	0.34
DG SG Freq. (Hz)	-0.56	0.14	t	11	0.66	0.52
CA1-CA3 Delta Coherence	-0.01	-0.02	Z	NA	1.1	0.27
CA1-DG Delta Coherence	-0.01	-0.01	Z	NA	0.37	0.71

Paired t tests when the test statistic given is t and Wilcoxon matched pairs signed rank test when the test statistic given is Z. Significant comparisons are bolded. For SWR Post-Pre, PVCre: n = 4 females, n = 3 males; SSTCre: n = 2 females, n = 4 males; PVCre/SSTCre: n = 5 females, n = 2 males.

## Discussion

Our findings support PV<sup>+</sup> and SST<sup>+</sup> interneurons in CA3 and DG as modulators of internal and external input to the hippocampus, respectively. Suppressing PV<sup>+</sup> interneurons lead to SWR modulation that matched increasing CA3 drive to CA1: SWR had higher incidence, faster frequency, and greater amplitude of coincident sharp waves and slow gamma<sup>54,64–67</sup>. Suppressing SST<sup>+</sup> interneurons had largely opposite effects, though slow gamma coherence was modulated while sharp wave and slow gamma power was not. Overall, interneuron suppression modulated multiple facets of SWRs, and these changes held in both cohorts and both sexes.

These SWR features changes could have the direct functional consequences. For instance, suppressing PV<sup>+</sup> interneurons abolished SWR rate increase following learning, which may impair consolidation of task-relevant memories<sup>68,69</sup> and may be caused by excessive CA3 drive preventing EC inputs from engaging the network to encode task-relevant information. Suppressing SST<sup>+</sup> interneurons increased SWR length, which may increase the underlying length of the underlying replay trajectory and improve working memory<sup>70</sup> and could be due to increased EC input, as EC activity increases prior to long SWRs<sup>62</sup>. Chains of SWRs may be replays of extended trajectories, which require ECIII input to CA1 during awake immobility, but not sleep<sup>65</sup>. Our findings support the role of CA3 input to CA1 for extended replays during sleep. Finally, fast ripples are an epileptic signature that can result from reduced GABAA-mediated inhibition converting SWRs to fast ripples<sup>71,72</sup> which can disrupt normal encoding<sup>73</sup>. Here, we find that disrupting PV<sup>+</sup> interneuron-mediated inhibition in CA3 and DG can induce fast ripples, but disrupting SST<sup>+</sup> interneuron-mediated inhibition cannot.

Previous studies altering PV<sup>+</sup> interneurons in CA1 shed light on how these interneurons play a different role than those in CA3 and DG. Suppressing CA1 PV<sup>+</sup> interneurons has no effect

in SWR incidence *in vivo*<sup>56,57,68</sup>, but does abolish learning-induced SWR rate increases<sup>68</sup>. This manipulation decreases SWR cycle length, but does not change SWR frequency<sup>57</sup>. In contrast, a computational model of somatic-targeting interneurons and pyramidal cells in CA1 found that increasing input strength to these interneurons increased SWR frequency<sup>74</sup>. Reducing excitatory input to CA1 PV<sup>+</sup> interneurons has been shown to reduce or increase SWR amplitude depending on the method<sup>75,76</sup>, but suppressing these interneurons has no effect<sup>56,68</sup>. Genetic or computational reduction of excitation onto CA1 PV<sup>+</sup> interneurons increases ensemble spiking during SWRs<sup>67,75</sup>. Blocking CA1 somatic inhibition *in vivo* and *in silico* leads to fast ripple generation<sup>61,67</sup>. Therefore, CA1 SWR rate, size, and frequency may be driven by CA3 independent of CA1 PV<sup>+</sup> interneurons, while increased CA1 pyramidal cell engagement and conversion to fast ripples may be broader phenomenon which can be modulated by any PV<sup>+</sup> interneuron population.

Somatic inhibition in CA1 is required for SWRs. Somatic IPSCs onto CA1 pyramidal cells<sup>57,67</sup> and CA1 PV<sup>+</sup> interneuron firing<sup>77</sup> are phase locked to SWRs. Rhythmic CA1 somatic inhibition paces ripple frequency activity in CA1<sup>57,67</sup>. Disrupting this inhibition reduces sharp wave amplitude, SWR energy, and multi-unit recruitment during SWRs and decouples pyramidal cell firing from phase-locking to SWRs<sup>61,78,79</sup>. However, since SWRs require transient increase in excitation over inhibition<sup>80</sup> and driving CA1 inhibition during SWRs can disrupt them<sup>61</sup>, decreasing somatic inhibition may provide windows of increased excitability leading to more SWRs.

We observed a strong positive modulation of SWR-coincident SG power throughout the hippocampus by PV<sup>+</sup> interneurons. Several lines of evidence support PV<sup>+</sup> interneurons as the main driver of slow gamma frequency rhythms<sup>81</sup>, but these studies would support the finding of SG power being abolished upon PV<sup>+</sup> interneuron suppression. Importantly, however, most studies of

PV<sup>+</sup> cell contribution to CA3-driven gamma has been during carbachol-induced gamma rhythms in *ex vivo* hippocampal sections generation<sup>82-84</sup>. Given our findings, SWR-coincident SG may be driven by a combination of increased CA3 drive and disinhibition or feedforward drive of local non-PV<sup>+</sup> interneurons, which may contribute to coordination with cortical areas during SWRs<sup>19</sup>.

While PV<sup>+</sup> interneurons appear to regulate SG power during SWRs, SST<sup>+</sup> interneurons orchestrate the coordination of this oscillation between subregions. A computational model demonstrated that O-LM cells firing at theta frequency can generate coherent slow gamma oscillations across distant CA3 cell assemblies<sup>85</sup> due to the extensive arborization of O-LM cells along the longitudinal axis of the hippocampus<sup>86</sup>. The authors hypothesized that since HIPP cells have similar innervation extents<sup>45</sup>, this model could predict how gamma coherence along the longitudinal axis of the dentate gyrus is achieved<sup>21,85</sup>. If slow gamma coherence is regulated in the same way during SWRs as during theta, this fits with our findings that CA3 and DG SST<sup>+</sup> interneurons are indispensable for SG coherence. SST<sup>+</sup> cells furthermore project to contralateral hippocampus in the same subregion<sup>87</sup>, which may help coordinate SG coherence across hemispheres as well. Overall, this may lead to more accurate underlying replay<sup>54</sup>.

CA1 SST<sup>+</sup> O-LM cells facilitate CA3 inputs by inhibiting feedforward inhibition from Schaffer collaterals while simultaneously reducing inputs from EC onto CA1 pyramidal cells by inhibiting pyramidal dendrites in the lacunosum-moleculare<sup>88,89</sup>. This would suggest O-LM cells are recruited to switch the network from retrieving or consolidating more remote associations to encoding current associations. CA1 bistratified cells similarly inhibit EC input to gate irrelevant inputs and enable encoding of relevant sensory cues during learning<sup>55</sup>. In contrast, suppression of O-LM cells during object memory encoding enhances retrieval performance<sup>90</sup>; under this paradigm, suppressing SST<sup>+</sup> interneurons may ungate relevant EC inputs to improve performance.



Since suppressing CA3 and DG SST<sup>+</sup> interneurons leads to decreased CA3 coupling to CA1, this suggests SST<sup>+</sup> interneurons may broadly be recruited to drive the network towards internal inputs and consolidation.

We observed the same effects when suppressing PV<sup>+</sup> and SST<sup>+</sup> interneurons simultaneously as when suppressing PV<sup>+</sup> cells alone. In line with these findings, genetically ablating AMPA currents to all hippocampal interneurons increases SWR rate, frequency, and CA1 pyramidal cell engagement<sup>91</sup>. This may be due to disinhibition. In CA1, SST<sup>+</sup> O-LM cells inhibit PV<sup>+</sup> cells, suppressing feedforward inhibition from CA3<sup>88,89,92</sup>. In DG, this disinhibitory circuit alters the discharge probability and temporal precision of the PV<sup>+</sup> interneuron targets<sup>93</sup>. It is therefore possible that many of the effects observed when suppressing SST<sup>+</sup> interneurons were due to disinhibition of PV<sup>+</sup> interneurons.

There is, of course, much variation within interneuron subtypes<sup>94</sup>, and so this Cre-driven approach dissected two cell types which may each represent several subtypes. Each of these subtypes has different connectivity, oscillatory phase preference, inputs, and membrane properties<sup>30</sup>. However, PV<sup>+</sup> interneuron classes broadly are more similar to each other than to SST<sup>+</sup> interneuron classes. One group of cells cannot be dissected with this approach: PV and SST co-expressing cells<sup>95</sup>, which comprise up to 30% and 5% of all PV<sup>+</sup> or SST<sup>+</sup> cells in CA3 and DG, respectively. Future work using intersectional approaches could determine how this specific class modulates EC and CA3 inputs.

Our findings support PV<sup>+</sup> and SST<sup>+</sup> interneurons bidirectionally modulating SWRs by controlling CA3 drive to CA1. A second possible mechanism is through regulating responses to EC up and down states. SWRs are temporally coordinated with down to up state transitions<sup>96-98</sup>, which may provide a substrate for hippocampal-cortical communication during learning<sup>20,99</sup>. In

cortex, PV<sup>+</sup> and SST<sup>+</sup> interneurons increase their firing rates in down and up states, respectively. PV<sup>+</sup> and SST<sup>+</sup> interneurons may differentially regulate hippocampal responses to these changes in cortical input to DG during sleep<sup>96</sup>, thus regulating SWRs. A third option is through regulating medial septum (MS) inputs. CA1 SST<sup>+</sup> cells form reciprocal connections onto GABAergic cells in the MS<sup>100–106</sup>, and recent work has shown DG SST<sup>+</sup> interneurons project to MS as well<sup>107</sup>. One specific class of MS GABAergic cells inhibit CA3 PV<sup>+</sup> axo-axonic cells during the sharp wave, which may be necessary for sharp wave initiation<sup>108</sup>; this could explain why suppressing CA3 PV<sup>+</sup> interneurons led to larger sharp waves. However, most MS GABAergic cells projecting to CA3 and DG and are suppressed during SWRs<sup>109–111</sup>. Moreover, an inhibitory network model was able to generate SWRs when MS inhibition was removed<sup>112</sup>. Therefore, SST<sup>+</sup> cells may regulate MS activity during SWRs, and their suppression could lead to increased nonspecific input from GABAergic septohippocampal neurons, which might reduce SWRs.

Myriad studies in cortex have shown PV<sup>+</sup> and SST<sup>+</sup> interneurons have distinct and often bidirectional roles. Specifically, this is found in tuning<sup>113,114</sup>, beta and theta frequency activity<sup>115</sup>, stimulus-induced gamma rhythms<sup>116,117</sup>, slow waves and spindles<sup>118–120</sup>, NREM<sup>118</sup>, reward encoding<sup>121</sup>, and working memory<sup>122,123</sup>. Here, we observe that these cells can bidirectionally modulate oscillations in the hippocampus as well.

SST<sup>+</sup> interneurons in the DG are specifically lost in Alzheimer's disease and normal aging models, and the extent of their loss correlates with memory impairments<sup>124,125</sup>. These models show reduced SWR rate, frequency, and coincident SG power<sup>59,69,126–130</sup>, and the extent of these impairments predicts memory deficits<sup>131</sup>. Suppression of CA3 and DG SST<sup>+</sup> interneurons in induces similar effects, thus it is possible that loss of these interneurons is directly responsible for SWR alterations in pathological and normal aging and related memory deficits.

We propose that PV<sup>+</sup> and SST<sup>+</sup> interneurons in CA3 and DG may modulate the switch between internal and external drive to the hippocampus, with PV<sup>+</sup> interneurons suppressing CA3 drive and SST<sup>+</sup> interneurons suppressing EC drive. A recent study found that a subset of CA1 PV<sup>+</sup> and SST<sup>+</sup> interneurons increase their firing at locomotion cessation, and hypothesized that they may facilitate the transition from theta oscillations driven by external inputs during movement to large irregular activity driven by internal inputs during immobility<sup>132</sup>. Our findings support this hypothesis and further suggest that interneurons may facilitate this network transition without a behavioral transition.

## References

1. Kay, K. & Frank, L. M. Three brain states in the hippocampus and cortex. *Hippocampus* (2018). doi:10.1002/hipo.22956
2. Buzsáki, G. Two-stage model of memory trace formation: A role for “noisy” brain states. *Neuroscience* **31**, 551–570 (1989).
3. Sosa, M., Gillespie, A. K. & Frank, L. M. in 1–58 (Springer Berlin Heidelberg, 2016). doi:10.1007/7854\_2016\_462
4. Carr, M. F. & Frank, L. M. A single microcircuit with multiple functions: state dependent information processing in the hippocampus. *Curr. Opin. Neurobiol.* **22**, 704–8 (2012).
5. Kemere, C., Carr, M. F., Karlsson, M. P. & Frank, L. M. Rapid and continuous modulation of hippocampal network state during exploration of new places. *PLoS One* **8**, e73114 (2013).
6. Winson, J. & Abzug, C. Neuronal transmission through hippocampal pathways dependent on behavior. *J. Neurophysiol.* **41**, 716–732 (1978).
7. Segal, M. A correlation between hippocampal responses to interhemispheric stimulation, hippocampal slow rhythmic activity and behaviour. *Electroencephalogr. Clin. Neurophysiol.* (1978). doi:10.1016/0013-4694(78)90192-X
8. Csicsvari, J., Hirase, H., Mamiya, A. & Buzsáki, G. Ensemble patterns of hippocampal CA3-CA1 neurons during sharp wave-associated population events. *Neuron* (2000). doi:10.1016/S0896-6273(00)00135-5
9. Ylinen, A., Bragin, A., Nádasdy, Z., Jandó, G., Szabó, I., Sik, A. & Buzsáki, G. Sharp wave-associated high-frequency oscillation (200 Hz) in the intact hippocampus: network and intracellular mechanisms. *J. Neurosci.* **15**, 30–46 (1995).

10. Buzsáki, G., Horváth, Z., Urioste, R., Hetke, J. & Wise, K. High-frequency network oscillation in the hippocampus. *Science* **256**, 1025–1027 (1992).
11. Girardeau, G., Benchenane, K., Wiener, S. I., Buzsáki, G. & Zugaro, M. B. Selective suppression of hippocampal ripples impairs spatial memory. *Nat. Neurosci.* **12**, 1222–1223 (2009).
12. Ego-Stengel, V. & Wilson, M. A. Disruption of ripple-associated hippocampal activity during rest impairs spatial learning in the rat. *Hippocampus* **20**, 1–10 (2010).
13. Jadhav, S. P., Kemere, C., German, P. W. & Frank, L. M. Awake Hippocampal Sharp-Wave Ripples Support Spatial Memory. *Science* **336**, 1454–1458 (2012).
14. Lee, A. K. & Wilson, M. A. Memory of Sequential Experience in the Hippocampus during Slow Wave Sleep. *Neuron* **36**, 1183–1194 (2002).
15. Diba, K. & Buzsáki, G. Forward and reverse hippocampal place-cell sequences during ripples. *Nat. Neurosci.* **10**, 1241–2 (2007).
16. Wilson, M. A. & McNaughton, B. Reactivation of hippocampal ensemble memories during sleep. *Science* **265**, 676–679 (1994).
17. Jadhav, S. P., Rothschild, G., Roumis, D. K. & Frank, L. M. Coordinated Excitation and Inhibition of Prefrontal Ensembles during Awake Hippocampal Sharp-Wave Ripple Events. *Neuron* **90**, 113–127 (2016).
18. Logothetis, N. K., Eschenko, O., Murayama, Y., Augath, M., Steudel, T., Evrard, H. C., Besserve, M. & Oeltermann, A. Hippocampal-cortical interaction during periods of subcortical silence. *Nature* **491**, 547–53 (2012).
19. Remondes, M. & Wilson, M. A. Slow- $\gamma$  Rhythms Coordinate Cingulate Cortical Responses to Hippocampal Sharp-Wave Ripples during Wakefulness. *Cell Rep.* **13**,

- 1327–35 (2015).
20. Sirota, A., Csicsvari, J., Buhl, D. & Buzsáki, G. Communication between neocortex and hippocampus during sleep in rodents. *Proc. Natl. Acad. Sci. U. S. A.* **100**, 2065–9 (2003).
  21. Bragin, A., Jandó, G., Nádasdy, Z., Hetke, J., Wise, K., Buzsáki, G., Szabó, G., Freund, T. F. & Hájos, N. Gamma (40–100 Hz) oscillation in the hippocampus of the behaving rat. *J. Neurosci.* **15**, 47–60 (1995).
  22. Colgin, L. L., Denninger, T., Fyhn, M., Hafting, T., Bonnevie, T., Jensen, O., Moser, M.-B. & Moser, E. I. Frequency of gamma oscillations routes flow of information in the hippocampus. *Nature* **462**, 353–357 (2009).
  23. Zheng, C., Bieri, K. W., Hsiao, Y.-T. & Colgin, L. L. Spatial Sequence Coding Differs during Slow and Fast Gamma Rhythms in the Hippocampus. *Neuron* 1–11 (2016).  
doi:10.1016/j.neuron.2015.12.005
  24. Kay, K., Sosa, M., Chung, J. E., Karlsson, M. P., Larkin, M. C. & Frank, L. M. A hippocampal network for spatial coding during immobility and sleep. *Nature* **531**, 185–190 (2016).
  25. Cheng, S. & Frank, L. M. New experiences enhance coordinated neural activity in the hippocampus. *Neuron* **57**, 303–13 (2008).
  26. O’Neill, J., Senior, T. & Csicsvari, J. Place-selective firing of CA1 pyramidal cells during sharp wave/ripple network patterns in exploratory behavior. *Neuron* (2006).  
doi:10.1016/j.neuron.2005.10.037
  27. Joo, H. R. & Frank, L. M. The hippocampal sharp wave–ripple in memory retrieval for immediate use and consolidation. *Nat. Rev. Neurosci.* **19**, 744–757 (2018).
  28. Jinno, S. & Kosaka, T. Patterns of expression of calcium binding proteins and neuronal

- nitric oxide synthase in different populations of hippocampal GABAergic neurons in mice. *J. Comp. Neurol.* **449**, 1–25 (2002).
29. Jinno, S. & Kosaka, T. Patterns of expression of neuropeptides in GABAergic nonprincipal neurons in the mouse hippocampus: Quantitative analysis with optical disector. *J. Comp. Neurol.* **461**, 333–49 (2003).
  30. Klausberger, T. & Somogyi, P. Neuronal diversity and temporal dynamics: the unity of hippocampal circuit operations. *Science* **321**, 53–7 (2008).
  31. Pangalos, M., Donoso, J. R., Winterer, J., Zivkovic, A. R., Kempster, R., Maier, N. & Schmitz, D. Recruitment of oriens-lacunosum-moleculare interneurons during hippocampal ripples. *Proc. Natl. Acad. Sci. U. S. A.* **110**, 4398–403 (2013).
  32. Katona, L., Lapray, D., Viney, T. J., Oulhaj, A., Borhegyi, Z., Micklem, B. R., Klausberger, T. & Somogyi, P. Sleep and movement differentiates actions of two types of somatostatin-expressing GABAergic interneuron in rat hippocampus. *Neuron* **82**, 872–86 (2014).
  33. Varga, C., Golshani, P. & Soltesz, I. Frequency-invariant temporal ordering of interneuronal discharges during hippocampal oscillations in awake mice. *Proc. Natl. Acad. Sci. U. S. A.* **109**, E2726–34 (2012).
  34. Royer, S., Zemelman, B. V., Losonczy, A., Kim, J., Chance, F., Magee, J. C. & Buzsáki, G. Control of timing, rate and bursts of hippocampal place cells by dendritic and somatic inhibition. *Nat. Neurosci.* **15**, 769–75 (2012).
  35. Somogyi, P., Katona, L., Klausberger, T., Lasztóczy, B. & Viney, T. J. Temporal redistribution of inhibition over neuronal subcellular domains underlies state-dependent rhythmic change of excitability in the hippocampus. *Philos. Trans. R. Soc. Lond. B. Biol.*

- Sci.* **369**, 20120518 (2014).
36. Sasaki, T., Piatti, V. C., Hwaun, E., Ahmadi, S., Lisman, J. E., Leutgeb, S. & Leutgeb, J. K. Dentate network activity is necessary for spatial working memory by supporting CA3 sharp-wave ripple generation and prospective firing of CA3 neurons. *Nat. Neurosci.* **1** (2018). doi:10.1038/s41593-017-0061-5
  37. Szabo, G. G., Du, X., Oijala, M., Varga, C., Parent, J. M. & Soltesz, I. Extended Interneuronal Network of the Dentate Gyrus. *Cell Rep.* **20**, 1262–1268 (2017).
  38. Hájos, N., Karlócai, M. R., Németh, B., Ulbert, I., Monyer, H., Szabó, G., Erdélyi, F., Freund, T. F. & Gulyás, A. I. Input-Output Features of Anatomically Identified CA3 Neurons during Hippocampal Sharp Wave/Ripple Oscillation In Vitro. *J. Neurosci.* **33**, (2013).
  39. Miles, R., Tóth, K., Gulyás, A. I., Hájos, N. & Freund, T. F. Differences between Somatic and Dendritic Inhibition in the Hippocampus. *Neuron* **16**, 815–823 (1996).
  40. Lovett-Barron, M., Turi, G. F., Kaifosh, P., Lee, P. H., Bolze, F., Sun, X.-H., Nicoud, J.-F., Zemelman, B. V., Sternson, S. M. & Losonczy, A. Regulation of neuronal input transformations by tunable dendritic inhibition. *Nat. Neurosci.* **15**, 423–30, S1-3 (2012).
  41. Freund, T. F. & Buzsáki, G. Interneurons of the hippocampus. *Hippocampus* **6**, 347–470 (1998).
  42. Wheeler, D. W., White, C. M., Rees, C. L., Komendantov, A. O., Hamilton, D. J. & Ascoli, G. A. Hippocampome.org: a knowledge base of neuron types in the rodent hippocampus. *Elife* **4**, (2015).
  43. Lee, C.-T., Kao, M.-H., Hou, W.-H., Wei, Y.-T., Chen, C.-L. & Lien, C.-C. Causal Evidence for the Role of Specific GABAergic Interneuron Types in Entorhinal



- Recruitment of Dentate Granule Cells. *Sci. Rep.* **6**, 36885 (2016).
44. Sik, A., Penttonen, M., Ylinen, A., Buzsáki, G., Wise, K. & Buzsáki, G. Hippocampal CA1 interneurons: an in vivo intracellular labeling study. *J. Neurosci.* **15**, 6651–65 (1995).
  45. Sik, A., Penttonen, M. & Buzsáki, G. Interneurons in the Hippocampal Dentate Gyrus: an In Vivo intracellular Study. *Eur. J. Neurosci.* **9**, 573–588 (1997).
  46. Udakis, M., Pedrosa, V., Chamberlain, S. E. L., Clopath, C. & Mellor, J. R. Interneuron-specific plasticity at parvalbumin and somatostatin inhibitory synapses onto CA1 pyramidal neurons shapes hippocampal output. *bioRxiv* 774562 (2019).  
doi:10.1101/774562
  47. Fernández-Ruiz, A., Oliva, A., Nagy, G. A., Maurer, A. P., Berényi, A. & Buzsáki, G. Entorhinal-CA3 Dual-Input Control of Spike Timing in the Hippocampus by Theta-Gamma Coupling. *Neuron* **93**, 1213-1226.e5 (2017).
  48. Taniguchi, H., He, M., Wu, P., Kim, S., Paik, R., Sugino, K., Kvitsiani, D., Fu, Y., Lu, J., Lin, Y., Miyoshi, G., Shima, Y., Fishell, G., Nelson, S. B. & Huang, Z. J. A resource of Cre driver lines for genetic targeting of GABAergic neurons in cerebral cortex. *Neuron* **71**, 995–1013 (2011).
  49. Hippenmeyer, S., Vrieseling, E., Sigrist, M., Portmann, T., Laengle, C., Ladle, D. R. & Arber, S. A developmental switch in the response of DRG neurons to ETS transcription factor signaling. *PLoS Biol.* **3**, e159 (2005).
  50. Krashes, M. J., Koda, S., Ye, C., Rogan, S. C., Adams, A. C., Cusher, D. S., Maratos-Flier, E., Roth, B. L. & Lowell, B. B. Rapid, reversible activation of AgRP neurons drives feeding behavior in mice. *J. Clin. Invest.* **121**, 1424–8 (2011).

51. Andrews-Zwilling, Y., Gillespie, A. K., Kravitz, A. V., Nelson, A. B., Devidze, N., Lo, I., Yoon, S. Y., Bien-Ly, N., Ring, K., Zwilling, D., Potter, G. B., Rubenstein, J. L. R., Kreitzer, A. C. & Huang, Y. Hilar GABAergic interneuron activity controls spatial learning and memory retrieval. *PLoS One* **7**, e40555 (2012).
52. Stefanelli, T., Bertollini, C., Lüscher, C., Muller, D. & Mendez, P. Hippocampal Somatostatin Interneurons Control the Size of Neuronal Memory Ensembles. *Neuron* **89**, 1074–1085 (2016).
53. Cimadevilla, J. M., Kaminsky, Y., Fenton, A. A. & Bures, J. Passive and active place avoidance as a tool of spatial memory research in rats. *J. Neurosci. Methods* **102**, 155–164 (2000).
54. Carr, M. F., Karlsson, M. P. & Frank, L. M. Transient Slow Gamma Synchrony Underlies Hippocampal Memory Replay. *Neuron* **75**, 700–713 (2012).
55. Lovett-Barron, M., Kaifosh, P., Kheirbek, M. A., Danielson, N., Zaremba, J. D., Reardon, T. R., Turi, G. F., Hen, R., Zemelman, B. V. & Losonczy, A. Dendritic inhibition in the hippocampus supports fear learning. *Science* **343**, 857–63 (2014).
56. Xia, F., Richards, B. A., Tran, M. M., Josselyn, S. A., Takehara-Nishiuchi, K. & Frankland, P. W. Parvalbumin-positive interneurons mediate neocortical-hippocampal interactions that are necessary for memory consolidation. *Elife* **6**, e27868 (2017).
57. Gan, J., Weng, S., Pernía-Andrade, A. J., Csicsvari, J. & Jonas, P. Phase-Locked Inhibition, but Not Excitation, Underlies Hippocampal Ripple Oscillations in Awake Mice In Vivo. *Neuron* **93**, 308–314 (2017).
58. Spanpanato, J. & Dudek, F. E. Targeted Interneuron Ablation in the Mouse Hippocampus Can Cause Spontaneous Recurrent Seizures. *eNeuro* **4**, ENEURO.0130-

- 17.2017 (2017).
59. Gillespie, A. K., Jones, E. A., Lin, Y.-H., Karlsson, M. P., Kay, K., Yoon, S. Y., Tong, L. M., Nova, P., Carr, J. S., Frank, L. M. & Huang, Y. Apolipoprotein E4 causes age-dependent disruption of slow gamma oscillations during hippocampal sharp-wave ripples. *Neuron* **90**, 740–751 (2016).
  60. Ramirez-Villegas, J. F., Logothetis, N. K. & Besserve, M. Diversity of sharp-wave-ripple LFP signatures reveals differentiated brain-wide dynamical events. *Proc. Natl. Acad. Sci.* **112**, E6379–E6387 (2015).
  61. Stark, E., Roux, L., Eichler, R., Senzai, Y., Royer, S. S. & Buzsáki, G. Pyramidal Cell-Interneuron Interactions Underlie Hippocampal Ripple Oscillations. *Neuron* **83**, 467–480 (2014).
  62. Oliva, A., Fernández-Ruiz, A., Fermino de Oliveira, E. & Buzsáki, G. Origin of Gamma Frequency Power during Hippocampal Sharp-Wave Ripples. *Cell Rep.* **25**, 1693–1700 (2018).
  63. Leung, L., Andrews-Zwilling, Y., Yoon, S. Y., Jain, S., Ring, K., Dai, J., Wang, M. M., Tong, L., Walker, D. & Huang, Y. Apolipoprotein E4 causes age- and sex-dependent impairments of hilar GABAergic interneurons and learning and memory deficits in mice. *PLoS One* **7**, e53569 (2012).
  64. Nakashiba, T., Buhl, D. L., McHugh, T. J. & Tonegawa, S. Hippocampal CA3 output is crucial for ripple-associated reactivation and consolidation of memory. *Neuron* **62**, 781–7 (2009).
  65. Yamamoto, J. & Tonegawa, S. Direct Medial Entorhinal Cortex Input to Hippocampal CA1 Is Crucial for Extended Quiet Awake Replay. *Neuron* **96**, 217–227.e4 (2017).

66. Wu, F., Stark, E. & Ku, P. Monolithically Integrated m LEDs on Silicon Neural Probes for High-Resolution Optogenetic Studies in Behaving Animals. 1136–1148 (2015).  
doi:10.1016/j.neuron.2015.10.032
67. Ramirez-Villegas, J. F., Willeke, K. F., Logothetis, N. K. & Besserve, M. Dissecting the Synapse- and Frequency-Dependent Network Mechanisms of In Vivo Hippocampal Sharp Wave-Ripples. *Neuron* **100**, 1224-1240.e13 (2018).
68. Ognjanovski, N., Schaeffer, S., Wu, J., Mofakham, S., Maruyama, D., Zochowski, M. & Aton, S. J. Parvalbumin-expressing interneurons coordinate hippocampal network dynamics required for memory consolidation. *Nat. Commun.* **8**, 15039 (2017).
69. Nicole, O., Hadzibegovic, S., Gajda, J., Bontempi, B., Bem, T. & Meyrand, P. Soluble amyloid beta oligomers block the learning-induced increase in hippocampal sharp wave-ripple rate and impair spatial memory formation. *Sci. Rep.* **6**, 22728 (2016).
70. Fernández-Ruiz, A., Oliva, A., Fermino de Oliveira, E., Rocha-Almeida, F., Tingley, D. & Buzsáki, G. Long-duration hippocampal sharp wave ripples improve memory. *Science* **364**, 1082–1086 (2019).
71. Behrens, C. J., van den Boom, L. P. & Heinemann, U. Effects of the GABA<sub>A</sub> receptor antagonists bicuculline and gabazine on stimulus-induced sharp wave-ripple complexes in adult rat hippocampus *in vitro*. *Eur. J. Neurosci.* **25**, 2170–2181 (2007).
72. Foffani, G., Uzcategui, Y. G., Gal, B., Menendez de la Prida, L., Szabo, I., Sik, A., Buzsáki, G., Wilent, W. B. & Higley, M. J. Reduced Spike-Timing Reliability Correlates with the Emergence of Fast Ripples in the Rat Epileptic Hippocampus. *Neuron* **55**, 930–941 (2007).
73. Ewell, L. A., Fischer, K. B., Leibold, C., Leutgeb, S. & Leutgeb, J. K. The impact of

- pathological high-frequency oscillations on hippocampal network activity in rats with chronic epilepsy. *Elife* **8**, e42148 (2019).
74. Melonakos, E. D., White, J. A. & Fernandez, F. R. A model of cholinergic suppression of hippocampal ripples through disruption of balanced excitation/inhibition. *Hippocampus* hipo.23051 (2018). doi:10.1002/hipo.23051
75. Rácz, A., Ponomarenko, A. A., Fuchs, E. C. & Monyer, H. Augmented hippocampal ripple oscillations in mice with reduced fast excitation onto parvalbumin-positive cells. *J. Neurosci.* **29**, 2563–8 (2009).
76. Polepalli, J. S., Wu, H., Goswami, D., Halpern, C. H., Südhof, T. C. & Malenka, R. C. Modulation of excitation on parvalbumin interneurons by neuroligin-3 regulates the hippocampal network. *Nat. Neurosci.* **20**, 219–229 (2017).
77. Klausberger, T., Magill, P. J., Márton, L. F., Roberts, J. D. B., Cobden, P. M., Buzsáki, G. & Somogyi, P. Brain-state- and cell-type-specific firing of hippocampal interneurons in vivo. *Nature* **421**, 844–8 (2003).
78. Schönberger, J., Draguhn, A. & Both, M. Lamina-specific contribution of glutamatergic and GABAergic potentials to hippocampal sharp wave-ripple complexes. *Front. Neural Circuits* **8**, 103 (2014).
79. Schlingloff, D., Káli, S., Freund, T. F., Hájos, N. & Gulyás, A. I. Mechanisms of sharp wave initiation and ripple generation. *J. Neurosci.* **34**, 11385–98 (2014).
80. Mizunuma, M., Norimoto, H., Tao, K., Egawa, T., Hanaoka, K., Sakaguchi, T., Hioki, H., Kaneko, T., Yamaguchi, S., Nagano, T., Matsuki, N. & Ikegaya, Y. Unbalanced excitability underlies offline reactivation of behaviorally activated neurons. *Nat. Neurosci.* **17**, 503–505 (2014).

81. Bartos, M., Vida, I. & Jonas, P. Synaptic mechanisms of synchronized gamma oscillations in inhibitory interneuron networks. *Nat. Rev. Neurosci.* **8**, 45–56 (2007).
82. Mann, E. O., Suckling, J. M., Hajos, N., Greenfield, S. A. & Paulsen, O. Perisomatic feedback inhibition underlies cholinergically induced fast network oscillations in the rat hippocampus in vitro. *Neuron* **45**, 105–17 (2005).
83. Gulyás, A. I., Szabó, G. G., Ulbert, I., Holderith, N., Monyer, H., Erdélyi, F., Szabó, G., Freund, T. F. & Hájos, N. Parvalbumin-containing fast-spiking basket cells generate the field potential oscillations induced by cholinergic receptor activation in the hippocampus. *J. Neurosci.* **30**, 15134–45 (2010).
84. Oren, I., Mann, E. O., Paulsen, O. & Hajos, N. Synaptic Currents in Anatomically Identified CA3 Neurons during Hippocampal Gamma Oscillations In Vitro. *J. Neurosci.* **26**, 9923–9934 (2006).
85. Tort, A. B. L., Rotstein, H. G., Dugladze, T., Gloveli, T. & Kopell, N. J. On the formation of gamma-coherent cell assemblies by oriens lacunosum-moleculare interneurons in the hippocampus. *Proc. Natl. Acad. Sci. U. S. A.* **104**, 13490–5 (2007).
86. Gloveli, T., Dugladze, T., Rotstein, H. G., Traub, R. D., Monyer, H., Heinemann, U., Whittington, M. A. & Kopell, N. J. Orthogonal arrangement of rhythm-generating microcircuits in the hippocampus. *Proc. Natl. Acad. Sci.* **102**, 13295–13300 (2005).
87. Eyre, M. D. & Bartos, M. Somatostatin-Expressing Interneurons Form Axonal Projections to the Contralateral Hippocampus. *Front. Neural Circuits* **13**, 56 (2019).
88. Leão, R. N., Mikulovic, S., Leão, K. E., Munguba, H., Gezelius, H., Enjin, A., Patra, K., Eriksson, A., Loew, L. M., Tort, A. B. L. & Kullander, K. OLM interneurons differentially modulate CA3 and entorhinal inputs to hippocampal CA1 neurons. *Nat.*

- Neurosci.* **15**, 1524–30 (2012).
89. Fuhrmann, F., Justus, D., Sosulina, L., Kaneko, H., Beutel, T., Friedrichs, D., Schoch, S., Schwarz, M. K., Fuhrmann, M. & Remy, S. Locomotion, Theta Oscillations, and the Speed-Related Firing of Hippocampal Neurons Are Controlled by a Medial Septal Glutamatergic Circuit. *Neuron* **86**, 1253–64 (2015).
  90. Siwani, S., França, A. S. C., Mikulovic, S., Reis, A., Hilscher, M. M., Edwards, S. J., Leão, R. N., Tort, A. B. L. & Kullander, K. OLM $\alpha$ 2 Cells Bidirectionally Modulate Learning. *Neuron* **99**, 404-412.e3 (2018).
  91. Caputi, A., Fuchs, E. C., Allen, K., Le Magueresse, C. & Monyer, H. Selective Reduction of AMPA Currents onto Hippocampal Interneurons Impairs Network Oscillatory Activity. *PLoS One* **7**, e37318 (2012).
  92. Banks, M. I., White, J. A. & Pearce, R. A. Interactions between Distinct GABAA Circuits in Hippocampus. *Neuron* **25**, 449–457 (2000).
  93. Savanthrapadian, S., Meyer, T., Elgueta, C., Booker, S. A., Vida, I. & Bartos, M. Synaptic properties of SOM- and CCK-expressing cells in dentate gyrus interneuron networks. *J. Neurosci.* **34**, 8197–209 (2014).
  94. Harris, K. D., Hochgerner, H., Skene, N. G., Magno, L., Katona, L., Bengtsson Gonzales, C., Somogyi, P., Kessaris, N., Linnarsson, S. & Hjerling-Leffler, J. Classes and continua of hippocampal CA1 inhibitory neurons revealed by single-cell transcriptomics. *PLOS Biol.* **16**, e2006387 (2018).
  95. Jinno, S. & Kosaka, T. Colocalization of parvalbumin and somatostatin-like immunoreactivity in the mouse hippocampus: Quantitative analysis with optical disector. *J. Comp. Neurol.* **428**, 377–388 (2000).

96. Sullivan, D., Csicsvari, J., Mizuseki, K., Montgomery, S. M., Diba, K. & Buzsáki, G. Relationships between hippocampal sharp waves, ripples, and fast gamma oscillation: influence of dentate and entorhinal cortical activity. *J. Neurosci.* **31**, 8605–16 (2011).
97. Battaglia, F. P., Sutherland, G. R. & McNaughton, B. L. Hippocampal sharp wave bursts coincide with neocortical &quot;up-state&quot; transitions. *Learn. Mem.* **11**, 697–704 (2004).
98. Isomura, Y., Sirota, A., Ozen, S., Montgomery, S. M., Mizuseki, K., Henze, D. A. & Buzsáki, G. Integration and segregation of activity in entorhinal-hippocampal subregions by neocortical slow oscillations. *Neuron* **52**, 871–82 (2006).
99. Mölle, M., Eschenko, O., Gais, S., Sara, S. J. & Born, J. The influence of learning on sleep slow oscillations and associated spindles and ripples in humans and rats. *Eur. J. Neurosci.* **29**, 1071–1081 (2009).
100. Gulyás, A. I., Görcs, T. J. & Freund, T. F. Innervation of different peptide-containing neurons in the hippocampus by gabaergic septal afferents. *Neuroscience* **37**, 31–44 (1990).
101. Takács, V. T., Freund, T. F. & Gulyás, A. I. Types and synaptic connections of hippocampal inhibitory neurons reciprocally connected with the medial septum. *Eur. J. Neurosci.* **28**, 148–164 (2008).
102. Jinno, S. & Kosaka, T. Immunocytochemical characterization of hippocamposeptal projecting GABAergic nonprincipal neurons in the mouse brain: a retrograde labeling study. *Brain Res.* **945**, 219–31 (2002).
103. Jinno, S., Klausberger, T., Marton, L. F., Dalezios, Y., Roberts, J. D. B., Fuentealba, P., Bushong, E. A., Henze, D., Buzsáki, G. & Somogyi, P. Neuronal diversity in GABAergic



- long-range projections from the hippocampus. *J. Neurosci.* **27**, 8790–804 (2007).
104. Gulyás, A. I., Hajos, N., Katona, I. & Freund, T. F. Interneurons are the local targets of hippocampal inhibitory cells which project to the medial septum. *Eur. J. Neurosci.* **17**, 1861–1872 (2003).
105. Freund, T. F. & Antal, M. GABA-containing neurons in the septum control inhibitory interneurons in the hippocampus. *Nature* **336**, 170–173 (1988).
106. Tóth, K., Freund, T. F. & Miles, R. Disinhibition of rat hippocampal pyramidal cells by GABAergic afferents from the septum. *J. Physiol.* **500**, 463–474 (1997).
107. Yuan, M., Meyer, T., Benkowitz, C., Savanthrapadian, S., Ansel-Bollepalli, L., Foggetti, A., Wulff, P., Alcami, P., Elgueta, C. & Bartos, M. Somatostatin-positive interneurons in the dentate gyrus of mice provide local- and long-range septal synaptic inhibition. *Elife* **6**, (2017).
108. Viney, T. J., Lasztóczy, B., Katona, L., Crump, M. G., Tukker, J. J., Klausberger, T. & Somogyi, P. Network state-dependent inhibition of identified hippocampal CA3 axo-axonic cells in vivo. *Nat. Neurosci.* **16**, 1802–1811 (2013).
109. Borhegyi, Z., Varga, V., Szilágyi, N., Fabo, D. & Freund, T. F. Phase segregation of medial septal GABAergic neurons during hippocampal theta activity. *J. Neurosci.* **24**, 8470–9 (2004).
110. Unal, G., Crump, M. G., Viney, T. J., Éltés, T., Katona, L., Klausberger, T. & Somogyi, P. Spatio-temporal specialization of GABAergic septo-hippocampal neurons for rhythmic network activity. *Brain Struct. Funct.* **223**, 2409–2432 (2018).
111. Salib, M., Joshi, A., Katona, L., Howarth, M., Micklem, B. R., Somogyi, P. & Viney, T. J. GABAergic Medial Septal Neurons with Low-Rhythmic Firing Innervating the Dentate

- Gyrus and Hippocampal Area CA3. *J. Neurosci.* **39**, 4527–4549 (2019).
112. Nicola, W. & Clopath, C. A diversity of interneurons and Hebbian plasticity facilitate rapid compressible learning in the hippocampus. *Nat. Neurosci.* **22**, 1168–1181 (2019).
  113. Miao, C., Cao, Q., Moser, M.-B. & Moser, E. I. Parvalbumin and Somatostatin Interneurons Control Different Space-Coding Networks in the Medial Entorhinal Cortex. *Cell* **171**, 507-521.e17 (2017).
  114. Wilson, N. R., Runyan, C. A., Wang, F. L. & Sur, M. Division and subtraction by distinct cortical inhibitory networks in vivo. *Nature* **488**, 343–348 (2012).
  115. Chen, G., Zhang, Y., Li, X., Zhao, X., Ye, Q., Lin, Y., Tao, H. W., Rasch, M. J. & Zhang, X. Distinct Inhibitory Circuits Orchestrate Cortical beta and gamma Band Oscillations. *Neuron* **96**, 1403-1418.e6 (2017).
  116. Veit, J., Hakim, R., Jadi, M. P., Sejnowski, T. J. & Adesnik, H. Cortical gamma band synchronization through somatostatin interneurons. *Nat Neurosci advance on*, (2017).
  117. Hakim, R., Shamardani, K. & Adesnik, H. A neural circuit for gamma-band coherence across the retinotopic map in mouse visual cortex. *Elife* **7**, (2018).
  118. Funk, C. M., Peelman, K., Bellesi, M., Marshall, W., Cirelli, C. & Tononi, G. Role of Somatostatin-Positive Cortical Interneurons in the Generation of Sleep Slow Waves. *J. Neurosci.* **37**, 9132–9148 (2017).
  119. Kuki, T., Fujihara, K., Miwa, H., Tamamaki, N., Yanagawa, Y. & Mushiake, H. Contribution of parvalbumin and somatostatin-expressing GABAergic neurons to slow oscillations and the balance in beta-gamma oscillations across cortical layers. *Front Neural Circuits* **9**, 6 (2015).
  120. Niethard, N., Ngo, H.-V. V, Ehrlich, I. & Born, J. Cortical circuit activity underlying

- sleep slow oscillations and spindles. *Proc. Natl. Acad. Sci. U. S. A.* **115**, E9220–E9229 (2018).
121. Kvitsiani, D., Ranade, S., Hangya, B., Taniguchi, H., Huang, J. Z. & Kepecs, A. Distinct behavioural and network correlates of two interneuron types in prefrontal cortex. *Nature* **498**, 363–366 (2013).
122. Abbas, A. I., Sundiang, M. J. M., Henoch, B., Morton, M. P., Bolkan, S. S., Park, A. J., Harris, A. Z., Kellendonk, C. & Gordon, J. A. Somatostatin Interneurons Facilitate Hippocampal-Prefrontal Synchrony and Prefrontal Spatial Encoding. *Neuron* (2018). doi:10.1016/J.NEURON.2018.09.029
123. Kim, D., Jeong, H., Lee, J., Ghim, J.-W., Her, E. S., Lee, S.-H. & Jung, M. W. Distinct Roles of Parvalbumin- and Somatostatin-Expressing Interneurons in Working Memory. *Neuron* (2016). doi:10.1016/j.neuron.2016.09.023
124. Andrews-Zwilling, Y., Bien-Ly, N., Xu, Q., Li, G., Bernardo, A., Yoon, S. Y., Zwilling, D., Yan, T. X., Chen, L. & Huang, Y. Apolipoprotein E4 causes age- and Tau-dependent impairment of GABAergic interneurons, leading to learning and memory deficits in mice. *J Neurosci* **30**, 13707–13717 (2010).
125. Spiegel, A. M., Koh, M. T., Vogt, N. M., Rapp, P. R. & Gallagher, M. Hilar interneuron vulnerability distinguishes aged rats with memory impairment. *J. Comp. Neurol.* **521**, 3508–3523 (2013).
126. Wiegand, J.-P. L., Gray, D. T., Schimanski, L. A., Lipa, P., Barnes, C. A. & Cowen, S. L. Age Is Associated with Reduced Sharp-Wave Ripple Frequency and Altered Patterns of Neuronal Variability. *J. Neurosci.* **36**, 5650–60 (2016).
127. Cowen, S. L., Gray, D. T., Wiegand, J.-P. P. L., Schimanski, L. A. & Barnes, C. A. Age-

- associated changes in waking hippocampal sharp-wave ripples. *Hippocampus* Epub ahead of print (2018). doi:10.1002/hipo.23005
128. Cayzac, S., Mons, N., Ginguay, A., Allinquant, B., Jeantet, Y. & Cho, Y. H. Altered hippocampal information coding and network synchrony in APP-PS1 mice. *Neurobiol. Aging* **36**, 3200–3213 (2015).
  129. Ciupek, S. M., Cheng, J., Ali, Y. O., Lu, H.-C. & Ji, D. Progressive Functional Impairments of Hippocampal Neurons in a Tauopathy Mouse Model. *J. Neurosci.* **35**, 8118–8131 (2015).
  130. Iaccarino, H. F., Singer, A. C., Martorell, A. J., Rudenko, A., Gao, F., Gillingham, T. Z., Mathys, H., Seo, J., Kritskiy, O., Abdurrob, F., Adaikkan, C., Canter, R. G., Rueda, R., Brown, E. N., Boyden, E. S. & Tsai, L.-H. Gamma frequency entrainment attenuates amyloid load and modifies microglia. *Nature* **540**, 230–235 (2016).
  131. Jones, E. A., Gillespie, A. K., Yoon, S. Y., Frank, L. M. & Huang, Y. Early Hippocampal Sharp-Wave Ripple Deficits Predict Later Learning and Memory Impairments in an Alzheimer’s Disease Mouse Model. *bioRxiv* 596569 (2019). doi:10.1101/596569
  132. Arriaga, M. & Han, E. B. Dedicated Hippocampal Inhibitory Networks for Locomotion and Immobility. *J. Neurosci.* **37**, 9222–9238 (2017).

## CONCLUSION AND FUTURE DIRECTIONS

Hippocampal oscillatory activity in the context of Alzheimer's disease (AD) is a unique window into the pathology of the hippocampal circuit. The hippocampi of AD patients and AD models are hyperactive, which may be the result of increased excitability of pyramidal and granule cells or decreased function of inhibitory interneurons. This hyperactivity has direct functional consequences. As gain control on inputs is lost, the network is hyper-responsive to all inputs and thus is unable to accurately discriminate between those which are relevant or irrelevant. In addition, loss of inhibitory function leads to an inability to generate and maintain oscillations. This oscillatory activity spreads information between regions of the brain and organizes encoding, retrieval, and consolidation of memories.

In the hippocampus, this pathology can be measured by assessing oscillatory activity. Incidence of sharp-wave ripples (SWRs) – an oscillation which organizes consolidation of memories – is reduced in AD models. This deficit is not rescued by removing pathological proteins from interneurons, suggesting this phenotype may be the result of increased pyramidal cell excitability which might convert SWRs into their pathological counterpart, fast ripples. The extent of SWR loss has the direct functional consequence of reducing spatial learning speed, as SWR rate deficit in apolipoprotein (apo) E4 knock-in (KI) mice predicts early learning in the Morris water maze. AD models also have a reduction of slow gamma (SG) power during SWRs, which is likely the result of interneuron loss. This deficit in CA3 – the predicted driver of SG during SWRs – can predict memory precision impairments and moreover can predict learning speed impairments over 10 months before cognitive impairment is detected. This would suggest that AD model mice have CA3 pathology which manifests as a reduction of CA3 SG power during SWRs at a young age and progresses to an inability to generate SWRs in aged animals.

However, many questions remain. First, future work should investigate the molecular mechanism by which apoE4 expression induces SWR impairments. In particular, SWRs may be supplanted by fast ripples, their pathological equivalent. Since fast ripples are found in epileptic patients and models and apoE4 increases epilepsy risk regardless of AD status, it is possible that fast ripples may hijack the normal circuitry of SWRs and thus reduce normal consolidation. Second, apoE4 carriers and apoE4-KI mice are highly variable across the population, but the populations studied are often too small to detect the genetic or epigenetic differences which protect some apoE4 carriers from AD. Additional experiments could also use SWR deficits at young ages to identify which apoE4 mice might be susceptible or resistant to developing cognitive decline. These mice could then be bred to enrich susceptibility or resistance and thus enrich for the genetic or epigenetic changes that might prove to be protective against AD. Finally, in order for SWRs to be a viable biomarker for future AD risk, these experiments should be repeated in other models of AD and a SWR deficit should be confirmed in apoE4 carriers using noninvasive techniques.

How this loss of GABAergic interneurons manifests as SWR pathology can further be dissected by examining the normal function of these interneurons. Parvalbumin-expressing (PV<sup>+</sup>) and somatostatin-expressing (SST<sup>+</sup>) interneurons in the CA3 and dentate gyrus (DG) are uniquely positioned to gate input from CA3 and entorhinal cortex (EC). Increasing drive from CA3 manifests as increased SWR and SG activity, while increasing drive from EC manifests as increased fast gamma activity. PV<sup>+</sup> interneurons participate in feedforward inhibition driven by EC and target the soma, thus are positioned to decrease drive from CA3. In contrast, SST<sup>+</sup> interneurons participate in feedback inhibition driven by local principal cell inputs and target distal apical dendrites at the level of EC inputs, thus are positioned to reduce drive from EC. Inhibiting PV<sup>+</sup> interneurons caused the circuit to generate greater CA3 drive, as measured by increased SWR

rate, SWR frequency, sharp wave amplitude, and coincident SG power throughout the circuit. In contrast, inhibiting SST<sup>+</sup> interneurons caused decreased CA3 drive, inverting many of the effects of PV<sup>+</sup> suppression while also decreasing the probability of SWR bursts, increasing SWR length, and decreasing SWR-coincident SG coherence throughout the circuit. Since SST<sup>+</sup> interneurons also target PV<sup>+</sup> interneurons, it is unsurprising that suppressing both cell types simultaneously caused similar effects as suppressing PV<sup>+</sup> interneurons alone. Therefore, these two interneuron subtypes in CA3 and DG may play opposing roles in regulating the transition between internal drive – consolidation of previous experiences – and external drive - encoding of new experiences – to the hippocampus.

Future experiments should test these findings by examining how these interneurons modulate input strength from temporammonic and Schaffer collateral inputs by measuring excitatory field potentials (fEPSPs). Future work might also test whether this bidirectional modulation occurs when driving rather than suppressing these interneurons, and the effect of manipulating these cells specifically during key network or behavioral states – for instance, only at decision points in a task, only during SWRs, or only when fast gamma power is high. Finally, the role of disinhibition should further be explored. Our results support SST<sup>+</sup> interneuron inhibition of PV<sup>+</sup> interneurons as a potential driver of network transitions, but another population of interneurons – vasoactive intestinal polypeptide-expressing (VIP) interneurons – inhibit both. Disinhibition plays a major role in cortical responses to input and may also do so in the hippocampus.

SWR pathologies observed in normal and AD pathological aging model mice - decreased SWR incidence, SWR frequency, and SWR-coincident SG - were observed when suppressing SST<sup>+</sup> interneurons, which are specifically lost in these mice. This suggests that loss of these

interneurons may directly affect SWRs in these models by aberrantly increasing drive from EC at the expense of CA3, leading to a lack of consolidation. These findings overall suggest that driving the activity of remaining SST<sup>+</sup> interneurons or supplanting SST<sup>+</sup> interneuronal innervation in CA3 and DG may be beneficial for improving hippocampal oscillatory activity related to memory consolidation in AD models and perhaps patients. This might translate into a reduction in cognitive decline.

In conclusions, SWRs provide a way to assess hippocampal network pathology and a way to measure gating of CA3 and EC inputs by GABAergic interneurons. This pathology – as assessed by SWR incidence and coincident SG power in CA3 – predicts memory impairments in an AD model, suggesting a potential mechanism for these impairments and a potential measurement to assess the functional efficacy of therapeutics, including those targeted at prodromal AD. Since the same hippocampal interneuron subtype lost in AD modulates SWR activity, SST<sup>+</sup> interneurons may provide a potential target for these therapeutics.

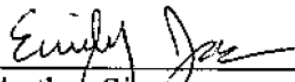


**Publishing Agreement**

*It is the policy of the University to encourage the distribution of all theses, dissertations, and manuscripts. Copies of all UCSF theses, dissertations, and manuscripts will be routed to the library via the Graduate Division. The library will make all theses, dissertations, and manuscripts accessible to the public and will preserve these to the best of their abilities, in perpetuity.*

***Please sign the following statement:***

*I hereby grant permission to the Graduate Division of the University of California, San Francisco to release copies of my thesis, dissertation, or manuscript to the Campus Library to provide access and preservation, in whole or in part, in perpetuity.*

  
\_\_\_\_\_  
Author Signature

23 Sept 2019  
Date